



VAAL UNIVERSITY OF TECHNOLOGY

**EFFECT OF PREPARATION PARAMETERS OF IRON OXIDE NANOPARTICLES
ON THE FENTON CATALYTIC ACTIVITY FOR THE DEGRADATION OF DYE**

MALATJI MATLHATSE

Student number: 213104369

Dissertation submitted in fulfilment of the requirement for the degree of

MAGISTER TECHNOLOGIAE: CHEMISTRY

**FACULTY OF APPLIED AND COMPUTER SCIENCES DEPARTMENT OF
CHEMISTRY**

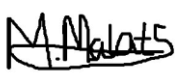
SUPERVISOR: Dr E.L. VILJOEN

CO-SUPERVISOR: Dr M.G. PELEYEJU

March 2021

DECLARATION

I declare that this dissertation was composed by myself, that the work contained herein is my own except where explicitly stated otherwise in the text and that this work has not been previously submitted for any other degree or professional qualification at another university.


..... (Candidate's signature)

04 day of March 2021

DEDICATION

This master work is dedicated to my late mother Christinah Maite Malatji and father Rueben Mashale. You may not be here to witness this work; however, I know I made you proud. Not forgetting my family for their unconditional love, support, encouragement talks and prayer.

ACKNOWLEDGEMENTS

All praise is due to Almighty GOD for the strength and good health throughout the course of this research work.

Sincere appreciation goes to my awesome Supervisor, Dr E.L. Viljoen, and Co-supervisor, Dr M.G. Peleyeju, for their patience and support. May God continue bless them for their kindness.

I would also like to express my gratitude to all other senior lecturers in the Chemistry Department, Vaal University of Technology (VUT) for their positive criticism and guidance shown to me during the course of this work. A special thanks to the laboratory technicians of the department, Mike, Sebokoza and Puleng for their assistance in understanding technical-related issues and for the lessons on operating instruments. A special thank you to my fellow masters student colleagues from the Chemistry Department for their immense support towards this work.

I want to express my deep gratitude to my family and friends, Khomotso, Ouyandi, Phindile, Nonkululeko and Busisiwe for their enormous support and encouragements. I am also grateful to all my VOFIM family, more especially my father and mother in the Lord Paul and Elsa Hagiazo for their constant prayers and support.

I would like to thank all the B.Tech postgraduate students that I worked with; all your projects contributed to this work.

My final thanks go to the NCAP group for their constant support and encouragement.

ABSTRACT

Water polluted by recalcitrant organics, such as methylene blue (MB), can be treated with the Fenton reaction. The Fenton reaction degrades the pollutants through catalytic oxidation. Unsupported iron oxide nanoparticles (IONPs) were used as catalysts in this study. Iron oxide nanoparticles were synthesised using a precipitation-oxidation method and effects of various preparation parameters on the shape, size and catalytic activity of the iron oxide nanoparticles were studied. Parameters investigated include preparation temperature, type and amount of precipitating agent. The precipitating agents used are sodium hydroxide, tetramethyl ammonium hydroxide (TMAOH), tetraethyl ammonium hydroxide (TEAOH) and ethylamine.

The iron oxide nanoparticles were found to be spherical for most of the preparation conditions as determined by TEM. However, irregular flower-like shapes (hexagonal with rod extensions) were obtained when the amounts of the TMAOH and TEAOH bases were more than the stoichiometric amounts. The nature and amount of precipitating agent also influenced the degree of particle agglomeration and growth, with an increase in alkyl chains in the base giving lesser agglomeration. The preparation temperature did not influence the nanoparticles' size when NaOH was used as a precipitating agent. In contrast, when an amine was used as a precipitation agent, caused a slight increase in the size of the nanoparticles. Different crystal phases like hematite, magnetite, maghemite and goethite-hematite mixture were identified in the X-ray diffractograms. UV-Vis spectroscopy showed that all the catalysts were red-shifted except for B3 sample, which was blue-shifted from the bulk materials.

The highest catalytic activities were obtained when NaOH was used as a precipitation agent instead of amine since catalyst has shown to contain the traces amounts of the base used on the surface. The lower catalytic activities for the catalysts prepared using amines may be due to amines adsorbed on the surface and blocking the catalytic active sites. FTIR spectra showed the presence of trace amounts of ammine functional groups on the nanoparticles. No correlation was found between the crystallite size and the Fenton catalytic activity of the catalyst. In the same vein, operational parameters such as the amount of H_2O_2 and temperatures did not show a direct effect on the Fenton catalytic efficiency. Kinetic studies show that the degradation of methylene blue followed the first-order models for all the catalysts prepared with NaOH. Overall, the study shows that different preparation parameters had an effect on the size, shape, phase and the catalytic performance of the synthesised IONPs.

TABLE OF CONTENTS

CHAPTER 1	1
INTRODUCTION	1
1.1 Problem statement.....	3
1.2 Aims and objectives	3
1.3 OUTLINE OF DISSERTATION.....	4
CHAPTER 2	5
LITERATURE REVIEW	5
2.1 FENTON REACTION.....	5
2.2 Enhanced Fenton processes	6
2.2.1 Electro-Fenton.....	7
2.2.2 Photo-Fenton process.....	7
2.3 IRON OXIDE NANOPARTICLES.....	8
2.4 Methods of synthesising iron oxide NPs.....	8
2.4.1 Thermal decomposition	8
2.4.2 Hydrothermal synthesis.....	9
2.4.3 Coprecipitation.....	10
2.4.4 Precipitation and oxidation method	10
2.5 SYNTHESIS AND EFFECTS OF PREPARATION PARAMETERS ON THE SIZE AND SHAPE OF IRON OXIDE NANOPARTICLES	11
2.5.1 Effect of the base type.....	12
2.5.2 Effect of the amount of base	13
2.5.3 Effect of temperature	13
2.6 METHYLENE BLUE POLLUTANT AND DEGRADATION PATHWAYS	14
2.7 FACTORS THAT AFFECT FENTON CATALYTIC ACTIVITY	17
2.7.1 Effect of catalyst particle size	17
2.7.2 Effect of phase on activity of iron oxide.....	17
2.7.3 Effect of oxidation state on size and activity of iron oxide.....	17
2.7.4 Effect of shape on activity of iron oxide.....	18
2.7.5 Effect of type of capping agent and iron precursor on catalytic activity	18
2.7.6 Effect of induction period on activity	19
CHAPTER 3	21
3. MATERIALS	21
3.1 Nanoparticles synthesis methods	21
3.1.1 Preparation of the iron oxide nanoparticles catalyst	21

3.2 CHARACTERISATION OF NANOPARTICLES.....	24
3.2.1 X-ray powder diffraction (XRD)	24
3.2.2 Fourier-transform infrared spectroscopy (FTIR)	25
3.2.3 Transmission electron microscopy (TEM).....	25
3.2.4 UV-Vis and PL analysis.....	26
3.3 FENTON DEGRADATION OF Methylene blue.....	26
3.3.1 Fenton catalytic decolourisation testing.....	26
CHAPTER 4	27
RESULTS AND DISCUSSIONS (PART 1).....	27
4.1 EFFECT OF TEMPERATURE OF REACTION on synthesis of iron oxide nanoparticles.	27
4.1.1 XRD ANALYSIS	27
4.1.2 STRUCTURAL ANALYSIS (TEM).....	29
4.1.3 FTIR ANALYSIS	31
4.1.4 UV-VIS AND PL RESULTS	32
4.2 EFFECT OF AMOUNT AND TYPE OF PRECIPITATING AGENT.....	36
4.2.1 XRD ANALYSIS	36
.....	37
4.2.3 FTIR ANALYSIS	41
4.2.4 UV-VIS AND PL RESULTS	43
4.3 EFFECT OF THE TYPE OF PRECIPITATING AGENT.....	46
4.3.1 XRD ANALYSIS	46
4.3.2 TEM ANALYSIS	48
4.3.3 FTIR ANALYSIS	50
4.3.4 UV/ VIS AND PL RESULTS.....	51
4.4. EFFECT OF TEMPERATURE using oxidation-precipitation-oxidation method.	54
4.4.1 TEM ANALYSIS	54
4.4.2 XRD ANALYSIS	56
4.4.3 FTIR ANALYSIS	57
4.4.5 OPTICAL PROPERTIES	59
4.5 RESULTS AND DISCUSSION (PART 2): FENTON DEGRADATION OF MB AND KINETIC STUDIES	62
-	Error! Bookmark not defined.
4.5.1.1 Performance reproducibility analysis of catalyst (M1).....	62
4.5.1.2 Re-usability of the catalyst for MB degradation	63
4.5.1.3 Effect of reaction temperature of catalyst synthesis on catalytic activity	67
4.5.1.4 Effect of calculated TEM sizes on catalytic activity.....	69
4.5.1.4 Effect of type precipitating agent (base) during synthesis of catalyst on catalytic activity	73

4.5.2 Optimazation of Fenton MB DEGRADATION REACTION PARAMETERS	76
4.5.2.1 Effect of temperature on the degradation of MB	76
4.5.2.2 Effect of H ₂ O ₂ dosage on the degradation of MB	77
CHAPTER 5	79
CONCLUSIONS AND RECOMMENDATIONS	79
5.1 CONCLUSIONS.....	79
5.2 RECOMMENDATIONS	80
REFERENCES	81
Appendix A.....	90

LIST OF FIGURES

Figure 2.1: XRD patterns of the Fe ₃ O ₄ at different temperatures; (a) 85 °C, (b) 65 °C, (c) 45°C and (d) 25 °C (pH: 11).....	13
Figure 2.2: Structure of methylene blue dye.....	14
Figure 2.3: Degradation pathways of methylene blue dye.....	15
Figure 2.4: Effect of operating parameters on CMP degradation in the NZVI/H ₂ O ₂ heterogeneous system: (a) pH.....	19
Figure 4.1: XRD patterns of iron oxide nanoparticles prepared at (a) 25, 45 and 85, (b) 65 and 100 °C	28
Figure 4.2: TEM images and histogram of iron oxide nanoparticles prepared at different temperature with M1 (a):25 °C, M2 (b):45 °C, M3 (c, d) 65 °C, M4 (e): 85 °C, M5: (f, g) 100 °C and zoomed out M3 (h) and M5 (i)	31
Figure 4.3: FTIR Spectrum of iron oxide nanoparticles prepared at different temperature with M1:25 °C, M2:45 °C, M3:65 °C, M4: 85 °C and M5:100 °C.....	32
Figure 4.4: (a) Absorption of iron oxide nanoparticles synthesised at different temperature with M1:25 °C, M2:45 °C, M3:65 °C, M4: 85 °C and M5:100 °C.....	34
Figure 4.4: (b) Tauc plot for direct bandgap of goethite and hematite nanoparticles. The intercept of a black lines with the horizontal axis defines the value of the bandgap at different temperature with M1:25 °C, M2:45 °C, M3:65 °C, M4: 85 °C and M5:100 °C.....	34
Figure 4.5: Emission spectrum of iron oxide nanoparticles synthesised at different temperature with M1:25 °C, M2:45 °C, M3:65 °C, M4: 85 °C and M5:100 °C.....	35

Figure 4.6: XRD patterns of iron oxide nanoparticles prepared at amine amounts of TMAOH (a): T1 0.06 mol, T2 0.09 mol, T3 0.12 mol, TEAOH (b): B1 0.06 mol, B2 0.09 mol and B3 0.12 mol.....	38
Figure 4.7: TEM images and histogram of iron oxide nanoparticles prepared ammine amounts of TMAOH: T1 (a, b) 0.06 mol, T2 (c, d) 0.09 mol and T3 (e, f) 0.12 mol.....	42
Figure 4.8: TEM images and histogram of iron oxide nanoparticles prepared at ammine amounts of TEAOH: B1 (a, b) 0.06 mol, B2 (c, d) 0.09 mol and B3 (e, f) 0.12 mol.....	42
Figure 4.9: (a) FTIR spectrum of iron oxide nanoparticles prepared with TMAOH amine at T1 0.06 mol, T2 0.09 mol and T3 0.12 mol.....	43
Figure 4.9: (b) FTIR spectrum of iron oxide nanoparticles prepared with TEAOH amine at B1 0.06 mol, B2 0.09 mol and B3 0.12 mol.....	43
Figure 4.10: Absorption of iron oxide nanoparticles synthesised with amine TMAOH (a) at amounts of T1: 0.06, T2: 0.09, T3: 0.12 mol, B1: 0.06, B2: 0.09 and B3: 0.12 mol for TEAOH (b).....	45
Figure 4.11.1: (a-f) Tauc plot for direct bandgap of iron oxide nanoparticles. The intercept with the horizontal axis shows the value of the bandgap at different temperature with T1: 0.06 mol TMAOH, T2: 0.09 mol TMAOH, T3:0.12 TMAOH, B1: 0.06 mol TEAOH, B2: 0.09 mol TEAOH and B3:0.12 mol TEAOH.....	94
Figure 4.11.2: (a-f) Tauc plot for indirect bandgap of magnetite nanoparticles. The intercept with the horizontal axis defines the value of the bandgap at different temperature with T1: 0.06 mol TMAOH, T2: 0.09 mol TMAOH, T3:0.12 TMAOH, B1: 0.06 mol TEAOH, B2: 0.09 mol TEAOH and B3:0.12 mol TEAOH.....	95
Figure 4.12: Emission spectrum of iron oxide nanoparticles synthesised with amine TMAOH (a) at amounts of T1: 0.06, T2.....	47
Figure 4.13: XRD diffractograms of iron oxide nanoparticles synthesised using different precipitating agents with MA1: $(\text{CH}_3)_4\text{N-OH}$, MA2: $(\text{CH}_3\text{CH}_2)_4\text{N-OH}$, MA3: NaOH and MA4: $\text{C}_2\text{H}_7\text{N}$	48
Figure 4.14: TEM images and histogram of iron oxide nanoparticles prepared by MA1 (a, b): $(\text{CH}_3)_4\text{N-OH}$, MA2 (c, d): $(\text{CH}_3\text{CH}_2)_4\text{N-OH}$, MA3 (e, f): NaOH and MA4 (g, h): $\text{C}_2\text{H}_7\text{N}$ precipitating agents.....	51

Figure 4.15: FTIR spectrum of iron oxide nanoparticles prepared with different precipitating agents MA1: $(\text{CH}_3)_4\text{N-OH}$, MA2: $(\text{CH}_3\text{CH}_2)_4\text{N-OH}$, MA3: NaOH and MA4:

$\text{C}_2\text{H}_7\text{N}$52

Figure 4.16: (a) absorption of iron oxide nanoparticles synthesised using different precipitating agents with MA1: $(\text{CH}_3)_4\text{N-OH}$, MA2: $(\text{CH}_3\text{CH}_2)_4\text{N-OH}$, MA3: NaOH and MA4.....53

Figure 4.16: (b) Tauc plot for direct bandgap of magnetite nanoparticles. The intercept of a black lines with the horizontal axis defines the value of the bandgap at different bases with MA1: $(\text{CH}_3)_4\text{N-OH}$, MA2: $(\text{CH}_3\text{CH}_2)_4\text{N-OH}$, MA3: NaOH and MA4: $\text{C}_2\text{H}_7\text{N}$53

Figure 4.17: Emission spectrum of iron oxide nanoparticles synthesised with different precipitating agents MA1: $(\text{CH}_3)_4\text{N-OH}$, MA2: $(\text{CH}_3\text{CH}_2)_4\text{N-OH}$, MA3: NaOH and MA4: $\text{C}_2\text{H}_7\text{N}$54

Figure 4.18: TEM images and histogram of iron oxide nanoparticles prepared at different temperature with MM1:25 °C (a, b), MM2:45 °C (c, d), MM3:65 °C (e, f), MM4: 85 °C (g, h) and MM5: 105 °C (i, j).....58

Figure 4.19: The effect of temperature on the TEM size.....95

Figure 4.20: XRD patterns of iron oxide nanoparticles prepared at temperatures MM1:25 °C, MM2:45 °C, MM3:65 °C, MM4: 85 °C and MM5: 105 °C.....58

Figure 4.21: (a, b) FTIR spectrum of iron oxide nanoparticles prepared at different temperature with MM1:25 °C, MM2:45 °C, MM3:65 °C, MM4: 85 °C and MM5:105 °C.....59

Figure 4.22: Absorption of iron oxide nanoparticles synthesised at different temperature with MM1:25 °C, MM2:45 °C, MM3:65 °C, MM4: 85 °C and MM5:105 °C.....60

Figure 4.23: (a-e) Tauc plot for direct bandgap of magnetite nanoparticles. The intercept of a black lines with the horizontal axis defines the value of the bandgap at different temperature with MM1:25 °C, MM2:45 °C, MM3:65 °C, MM4: 85 °C and MM5:105 °C.....61

Figure 4.24: (a, b): The effect of temperature on the wavelength peak maximum of iron oxide nanoparticles.....96

Figure 4.25: The effect of temperature on the XRD size.....97

Figure 4.26: Emission spectrum of iron oxide nanoparticles synthesised at different temperature with MM1:25 °C, MM2:45 °C, MM3:65 °C, MM4: 85 °C and MM5:105 °C.....	62
Figure 4.27(a): Performance reproducibility analysis of M1 catalyst for removal of MB in 180 min.....	64
Figure 4.27: (b) pseudo 1st order performance reproducibility plot of the degradation of MB (M1) catalyst.....	64
Figure 4.28: (a) effect of reusing the catalyst on degradation of MB of M1 catalyst	66
Figure 4.28: (b) Influence of reusing the catalyst on the average rate per gram of catalyst.....	66
Figure 4.29: (a) pseudo-first order plots of the reusability study for degradation of MB of catalyst M1 in 180 min.....	97
Figure 4.29: (b) pseudo-second order plots of the reusability study for degradation of MB of catalyst M1 in 180 min.....	97
Figure 4.30: effect of catalyst synthesis temperature for MM1, MM3 and MM5 synthesised with iron (II) chloride and tetramethyl ammonium hydroxide base on MB degradation.....	67
Figure 4.31: Effect of catalyst synthesis temperature for M1, M3 and M3 synthesised with iron (III) nitrate and NaOH base on MB degradation	69
Figure 4.31.1: Picture of the Fenton reactor (a) and colour change (b) during MB removal.....	69
Figure 4.32: % MB removal over catalysts of different particles (M1:1.5, M3:2.3, M5:2.1, MM1:5.7, MM3: 7.6 and MM5:8.8 nm).....	70
Figure 4.33: (a) pseudo-first order and (b) pseudo-second order plots of the degradation of MB using iron oxide particles prepared with 0.04 mL (CH ₃) ₄ N-OH at 25, 65 and 105 °C.....	72
Figure 4.34: (a) pseudo-first order and (b) Pseudo-second order plots of the degradation of MB using iron oxide particles prepared with 0.04 mL NaOH at 25, 65 and 100 °C.....	73
Figure 4.35: Effect of the type of base on MB degradation in 180 min.....	75

Figure 4.36: (a) pseudo-first order and (b) pseudo-second order plots of the degradation of MB using iron oxide particles prepared with 0.04 mL $(\text{CH}_3)_4\text{N-OH}$, $(\text{CH}_3\text{CH}_2)_4\text{N-OH}$, NaOH and $\text{C}_2\text{H}_7\text{N}$77

Figure 4.37: Influence of reaction temperature on the discoloration of MB (10 mg/L MB, $\text{H}_2\text{O}_2 = 20$ mL, 0.1003 g iron oxide catalyst).....78

Figure 4.38: Influence of the amount of H_2O_2 on the removal of MB for M1 (50 °C, 10 mg/L MB, 0.1003 g iron oxide catalyst).....79

LIST OF TABLES

Table 3.1: List of chemicals used, purity and suppliers.....20

Table 3.2: Preparation conditions using the precipitation and oxidation (olation-oxolation).....22

Table 3.3: Preparation conditions using the oxidation-precipitation-oxidation (Olation-Oxolation).....23

Table 3.4: Measured MB, H_2O_2 and H_2O at each reaction.....24

Table 4.1: Calculated crystallite sizes calculation XRD.....29

Table 4.2: Calculated crystallite sizes calculation XRD.....39

Table 4.3: Calculated crystallite sizes calculation XRD.....49

Table 4.4: Calculated sizes calculation XRD.....58

Table 4.5: Measured mass at each run.....65

Table 5.6: Calculation of regression coefficient R^268

Table 4.7: Calculation of regression coefficient R^272

Table 4.8: Calculation of regression coefficient R^273

Table 4.9: Calculated sizes XRD, TEM and % MB removal for MA1, MA2, MA3 and MA475

Table 4.10: Calculation of regression coefficient R^277

LIST OF ABBREVIATIONS AND ACRONYMS

SEM - Scanning electron microscope

UV/VIS - Ultraviolet–visible spectroscopy

XRD - X-ray powder diffraction

XPS - X-ray photoelectron spectroscopy

TEM - Transmission Electron Microscopy

TMAOH –Tetramethyl ammonium hydroxide

TEAOH - Tetraethyl ammonium hydroxide

AOP- Advanced oxidation processes

MB – Methylene blue

PL - Photoluminescence

NPs - Nanoparticles

CMC - Carboxymethyl cellulose

PEG-Polyethylene glycol

PVP- Poly N-vinyl pyrrolidone

BPA- Bisphenol A

HRTEM - High Resolution Transmission Electron Microscopy

CHAPTER 1

INTRODUCTION

Water pollution by industries causes serious environmental problems since it affects human health and the ecosystem negatively. Water scarcity in South Africa is increasing rapidly as the population is also increasing, resulting in more utilisation of water for industries, agriculture and households each day (Wang *et al.*, 2012). Wastewater from industries and run-off water from agriculture often contain toxic contaminants, which get into water bodies (Wintgens *et al.*, 2008). As a result of increased industrialisation, clean water availability is also reduced, posing a great concern to water-dependent organisms (i.e. plants and humans) and the ecosystem (Inyinbor *et al.*, 2018). Depending on the source and type, water pollution affects human health and the ecosystem differently. For instance, pollutants such as dyes, heavy metals and other organic pollutants may be carcinogenic. Some pharmaceuticals, hormones and personal care product wastes are known to be endocrine-disruptive chemicals (Adejumoke *et al.*, 2018). These types of pollutants enter into various water channels and become a great concern due to different types of hazards they pose on the environment, human health and aquatic life.

Many industries, such as food, textile, pharmaceutical and leather industries, produce their products using dyes (Singh *et al.*, 2015). These industries produce large amounts of effluents, which are the main source of water pollution. These effluents contain both organic and inorganic compounds (Mohamed *et al.*, 2017). Organic pollutants consist of chemicals such as phenols, chlorinated phenols, endocrine chemicals, azo dyes, pesticides and herbicides (Eman *et al.*, 2017), whereas inorganic pollutants are non-carbon containing compounds, salts and metals. Many of these occurs naturally and are regarded as an integral part of those waters; for instance, hard water contains pollutants such as calcium carbonate and bicarbonate. Inorganic metal ions such as Pb^{2+} , Cd^{2+} , Hg^{2+} , As^{3+} and Ni^{2+} are toxic and have a long-term hazardous impact (Sharma *et al.*, 2018).

Organic pollutants are mostly human-induced chemicals. They enter into different water bodies via industrial chemicals, pesticides and as the by-products of degradation of other chemicals (Hossain *et al.*, 2012). These pollutants tend to bio-accumulate and bio-magnify, exhibiting toxicity. Some are mutagenic, carcinogenic and teratogenicity, causing chronic and acute

disorders (Barnes *et al.*, 2008). Dyes are substances mostly used in paint, paper, pharmaceutical, leather and textile industries. More than 100 000 commercial dyes are produced in a year and over 7×10^5 tonnes of these are used (Pearce *et al.*, 2003). Synthetic dyes can be grouped into three classes: (1) cationic dyes, (2) anionic dyes and (3) non-ionic dyes (Greluk & Hubacki., 2010). Methylene blue (MB) is a type of cationic aromatic organic synthetic dye, which is mainly used in food, textile, pharmaceutical and leather industries (Singh *et al.*, 2015). High concentrations, above the acceptable levels for water consumption, of this dye cause negative health effects such as breathing problems, eye damage and blood disorders (Özer *et al.*, 2007). MB, as one of the recalcitrant organic pollutants, is used as a model in this research.

Various methods have been reported for the removal of organic pollutants in water. These include coagulation, precipitation, filtration, adsorption, ozonation and ion exchange reverse osmosis (Rashed, 2013). However, these methods have high operational costs and may not be effective for some recalcitrant organic substances (Rashed, 2013). Advanced oxidation processes (AOP) such as photocatalysis, Fenton and electro-Fenton are being developed and applied for the degradation of organic pollutants, where the highly reactive hydroxyl radicals ($\cdot\text{OH}$) oxidise organic pollutants into inorganic ions or smaller and non-toxic products (Wan *et al.*, 2016).

Fenton reaction, as an advanced oxidation process, is an attractive process because it is simple, cost-effective, rapid, non-selective in contaminants degradation and environmentally friendly. This reaction can be classified into heterogeneous and homogeneous Fenton. In homogeneous Fenton reaction, the catalyst and the contaminant are in the same phase, usually in aqueous phase. In heterogeneous catalysis, the pollutant and the catalyst are in different phases (Ali *et al.*, 2014). The pollutant is usually in liquid phase while the catalyst is solid (Wang *et al.*, 2014). Heterogeneous Fenton reaction is preferred to homogeneous Fenton reaction because of the ease of separation of the catalyst from the mixture at the end of the reaction. Heterogeneous catalyst typically provides large surface area to volume ratio and consists of metals dispersed on support materials (Zhang *et al.*, 2019). This system provides for the generation of hydroxyl radicals ($\cdot\text{OH}$) for the oxidation or mineralisation of most organic compounds without secondary pollution. The solid catalyst can also be readily separated and recycled. (Zhang *et al.*, 2019). Heterogeneous process showed the highest removal efficiencies

under optimum condition with Dye removal of 85% in comparison with 82% of homogeneous (Sreeja & Sosamony., 2016)

1.1 PROBLEM STATEMENT

There is no doubt that the quality of water available for use has been declining worldwide as a result of excessive water pollution by non-biodegradable organic pollutants such as dyes. Synthetic dyes significantly compromise the quality of water bodies, increase biochemical, impair photosynthesis, inhibit plant growth and may promote the toxicity, carcinogenicity and mutagenicity when deposited in food chain. This pollution is a result of an increase in the number of industries globally. It is therefore important to develop simple but effective and efficient technologies to degrade these pollutants to protect the environment and the health of living organisms. One water treatment method that has been shown to have the potential to effectively remove these organic pollutants from water is heterogeneous Fenton oxidation. However, the success of this technique depends on the catalyst. Consequently, there is a need to synthesise and study the effects of various synthesis conditions on a promising catalyst like iron oxide with a view to obtaining a very active catalyst.

1.2 AIMS AND OBJECTIVES

The aim of the study was to investigate empirically the effects of preparation parameters such as temperature, the type and amount of precipitating agent, reaction time and oxidising agent on the size, shape, phase and Fenton catalytic activity of iron oxide nanoparticles.

The objectives are as follows:

- To determine the effect of the reaction temperature on the size, phase and shape of iron oxide particles. The temperature was varied from 25 °C-100 °C
- To assess the effect of pressure and temperature on the size, phase and shape of iron oxide particles when temperature was investigated from 25 °C-105 °C
- To study the effect of the type of precipitating agent on the size, shape and phase of iron oxide particles. Sodium hydroxide, ammonium hydroxide, tetramethylammonium hydroxide and tetraethylammonium hydroxide were used as precipitating agents
- To characterise the iron oxide nanoparticles using TEM, XRD, UV-Vis spectroscopy and PL spectroscopy
- To test the repeatability and reusability of the iron oxide nanoparticles catalysts

- To test the Fenton catalytic activity of the iron oxide nanoparticles
- To determine the influence Fenton operational parameters such a temperature and amount of hydrogen peroxide on the catalytic activity

1.3 OUTLINE OF DISSERTATION

The dissertation has five chapters:

Chapter 1

Discussions on water pollution, the various methods that are used for water purification and the problem to be addressed in this study are presented. The aim and objectives are also outlined.

Chapter 2

In this chapter, concepts and themes relevant to the study are reviewed. These include Fenton processes and heterogeneous catalysts for Fenton reactions.

Chapter 3

The materials, methods and instruments used in the work are presented in this chapter.

Chapter 4

In this chapter, the results of the various experiments conducted to achieve the aim of the study are presented and discussed.

Chapter 5

This chapter contains the conclusions and recommendations.

.

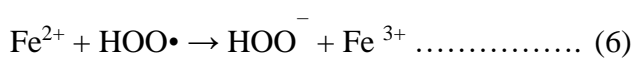
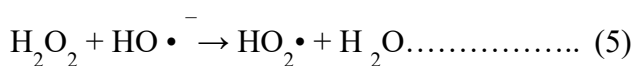
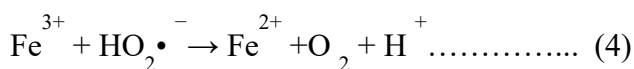
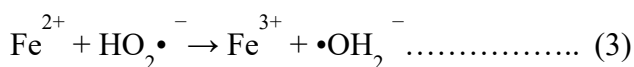
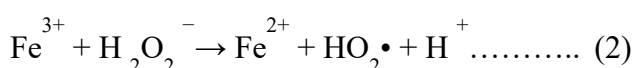
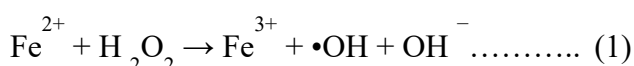
CHAPTER 2

LITERATURE REVIEW

2.1 FENTON REACTION

The Fenton reaction is one of the most effective and efficient advanced oxidation processes (AOPs) used for the removal of a wide range of harmful organic pollutants from aqueous environments. The reaction is simple, cost-effective, rapid, non-selective in contaminants degradation and environmentally friendly since the hydrogen peroxide decomposes into water and oxygen. Generally, the Fenton reaction uses H_2O_2 and ferrous ion (Fe^{2+}) to generate $\bullet\text{OH}$, which is environmentally benign and possesses a higher oxidation potential of 2.8 eV (higher than that of H_2O_2 , which is 1.78 eV) (Wang *et al.*, 2014).

For the reaction to occur the optimal condition is verified to be in the range of pH 2-4. Eqs.2-5 represent the rate of limiting steps in the reaction since the hydrogen peroxide is consumed and regeneration of ferrous ion (Fe^{2+}) from ferric ion (Fe^{3+}) (Wang *et al.*, 2014). Fenton reaction also show the radical-radical or hydrogen peroxide-radical reaction as a result of eqs.6-8. Few drawbacks may occur as a result of the wastage of oxidants from the scavenging effect of the hydrogen peroxide (eq.7) and another could result from continuous loss of the iron ions. The reactions involved in $\bullet\text{OH}$ generation are listed in equations 1-8:



(Wang *et al.*, 2014)

The Fenton reaction is divided into two categories, namely homogeneous and heterogeneous. In the homogeneous Fenton process, the Fe^{2+} and the contaminants are in the same phase and the process has no limitations for mass transfer (Zhao *et al.*, 2014; De Luna *et al.*, 2014). However, the formation of large amounts of sludge and catalyst deactivation owing to formation of Fe complex(es) and operation in narrow pH range of (2.0 - 4.0) are major drawbacks of the homogeneous Fenton process (Javaid & Qazi, 2019). These mentioned shortcomings of the homogeneous Fenton process can be circumvented by using a solid catalyst (heterogeneous catalysis) (Javaid & Qazi, 2019). In the heterogeneous Fenton reaction, the iron species may be immobilised on a support such that the contaminants in aqueous solution can be effectively oxidised without iron hydroxide sludge being formed. In addition, the ease of recovering and recycling the solid catalyst and operation over a wide pH range make heterogeneous Fenton catalysis more attractive than the homogeneous process. It is also of note that the catalyst supports may significantly enhance the catalytic performance of the system. A variety of materials, such as activated carbon, clay, silica, zeolite and so on, have been employed as supports for Fe in the heterogeneous Fenton system (Yu *et al.*, 2019).

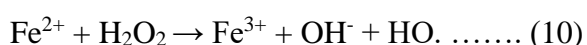
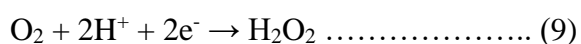
Commercially supported catalyst is used to enable easy separation by filtration which is not possible for nanomaterial. Support material is added to the catalyst composition to prevent nanoparticle agglomeration and sintering during catalytic operation. Furthermore, if a continuous fixed bed operation is used, support and shaped catalyst particles in the millimeter range are used to prevent large pressure drops in the reactor (Chorkendorff & Niemantsverdriet., 2003). However, supports often cause mass transfer limitations leading to the rate of mass transfer being the rate limiting step which leads to a decrease in the catalytic activity (Morris *et al.*, 2015). For example, when support with small pores were used, it caused the rate of reaction to decrease due to slow inter-particle diffusion (Khodakov *et al.*, 2002). In this study unsupported catalyst were used to study the effect of the size and shape of the iron oxide nanoparticles on the catalytic activity in the absence of mass transfer limitations.

2.2 ENHANCED FENTON PROCESSES

Various types of enhanced Fenton processes have been proposed for more efficient catalytic systems and improved degradation of organic pollutants in water. These include electro-Fenton, photo-Fenton, photoelectron Fenton, to name a few and only electro-Fenton and Photo-Fenton will be discussed since the photoelectron Fenton is the combination of the discussed reactions (Ameta *et al.*, 2018).

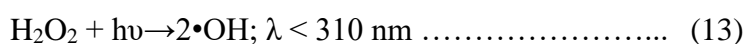
2.2.1 Electro-Fenton

The electro-Fenton process is a hybrid technology for improved oxidative removal of organic pollutants from water. It can overcome the economical limitations of the Fenton reaction by producing hydrogen peroxide *in-situ* (Dios *et al.*, 2014). This technology uses electricity to continuously generate the H₂O₂ at a suitable cathode through the reduction of the dissolved oxygen or air (Pushpalatha *et al.*, 2017). The *in-situ* formed hydrogen peroxide, together with an iron catalyst yields the reactive hydroxyl radicals (Pushpalatha *et al.*, 2017). The electro-Fenton process is thus very similar to the Fenton reaction and the only difference is the source of the hydrogen peroxide in equations 9-10. Electro-Fenton process may be advantageous since the contaminants are removed by Fenton reagents together with anodic oxidations on the surface, however few challenges such as slow production of H₂O₂ due to low solubility, low current efficiency at high pH and higher operational costs have limited the application of electro-Fenton.



2.2.2 Photo-Fenton process

In photo-Fenton process, light energy is incorporated to improve the overall process. Usually, the reaction occurs in the presence of UV-visible light below 600 nm (Shima *et al.*, 2014). The UV light in the reaction plays three roles, which lead to enhancement in the decontamination process. First, photo-reduction of Fe³⁺ to Fe²⁺ ions occur as shown in Equation (12); the photo-generated Fe²⁺ ions react with H₂O₂ in solution to produce more hydroxyl radicals. Secondly, direct photolysis of the H₂O₂ molecules to produce the reactive hydroxyl radicals can take place as shown in Equation 13. Lastly, the photons can also decompose some of the most problematic insoluble iron complex formed in the reaction mixture. Formation of iron complexes depletes the amount of iron in solution, thus adversely affects the efficiency of the process (Malato *et al.*, 2015).



2.3 IRON OXIDE NANOPARTICLES

The study of nanomaterials in the last decades has gained more attention from researchers due to their unique properties as compared to the bulk materials. Advances in the synthesis of nanomaterials, particularly iron oxide nanoparticles, has enabled different applications in diverse fields, such as biological and medical sciences and environmental technology (Mornet *et al.*, 2004; Xu *et al.*, 2012). In the laboratory, these iron oxides exist in nature, such as α -Fe₂O₃, γ -Fe₂O₃ and Fe₃O₄. They are prepared using methods such as co-precipitation (Miao *et al.*, 2011), thermal decomposition (Zhu *et al.*, 2011) and hydrothermal method (Tadic *et al.*, 2011). The important features, which make iron oxide nanoparticles very interesting and promising materials for extensive water decontamination are the ease of separation using external magnetic fields, high surface area to volume ratio, distinct and beneficial morphology and high stability (Sharma *et al.*, 2018). Depending on some specific properties and surface functionalities, iron oxide nanoparticles could be applied as photocatalyst, sorbent, or coagulant in water purification (Sharma *et al.*, 2018). The application of iron oxide nanoparticles as catalysts in heterogeneous Fenton process for water treatment has received tremendous interest. This is due to their special features such as high surface area to volume ratio, high activity and stability (Pastrana-Martinez *et al.*, 2014).

2.4 METHODS OF SYNTHESISING IRON OXIDE NPS

Various methods have been reported for the synthesis of iron oxide nanoparticles. These include wet chemical methods, dry processes and biological routes. A few wet chemical methods are discussed below.

2.4.1 Thermal decomposition

The syntheses of iron oxide nanoparticles by the thermal decomposition of iron complexes such as Fe(cup)₃, (cup = N-nitrosophenyl hydroxylamine), Fe(acac)₃ (acac = acetylacetonate) and Fe(CO)₅ have been reported (Wu *et al.*, 2008). Oxidation of the decomposed iron oxide precursor affords high-quality, monodispersed iron oxide nanoparticles (Wu *et al.* 2008). Although the method leads to the production of high-quality iron oxide, it is cumbersome and usually requires relatively high temperatures (Wu *et al.* 2008). In a study by Sun and Zeng (2002), monodispersed magnetite nanoparticles were obtained by the thermal decomposition of Fe(acac)₃ at 265 °C. The complex was in a solution of phenyl ether, alcohol, oleic acid and oleylamine. The magnetite NPs were reported to have average particle sizes of 20 nm.

2.4.2 Hydrothermal synthesis

Hydrothermal synthesis of nanoparticles is achieved by placing the aqueous solution of the precursor in a sealed reactor and the reactor is heated to temperatures ranging from 130-250 °C at a high vapour pressure (Citakovi, 2011). This method is known to yield better crystallites iron oxide NPs compared to thermal decomposition. There are many reports on the use of hydrothermal methods for the synthesis of iron oxide nanoparticles. Salazar *et al.* (2011) reported the synthesis of magnetic iron oxide nanoparticles with the size range of 10-40 nm by using ammonium bases R_4NOH ($R=CH_3, C_2H_5, C_3H_7$) with different alkyl group length to obtain different particles sizes under argon with hydrothermal treatment. An efficient route for simultaneous synthesis and self-assembly of 3D layered β -FeOOH nano rods was reported by Fang *et al.* (2010). The nature of particles depended on a pH-induced strategy, in which the continuous change of pH was achieved by hydrolysis of $FeCl_3 \cdot 6H_2O$ in the presence of urea under hydrothermal conditions. The electron microscopy observations revealed that the square-prismatic β -FeOOH nano rods were self-assembled in a side-by-side fashion to form highly oriented 2D nano rod arrays, and the 2D nano rod arrays were further stacked in a face-to-face fashion to form the final 3D layered architectures.

A novel nickel-assisted iron oxide ($Ni@FeO_x$) nanocomposites with various Ni/Fe ratio were successfully synthesized via a facile hydrothermal method (Xie *et al.*, 2017). A determined amount of nickel(II) chloride hexahydrate and pre-synthesized Fe_2O_3 nanoparticles was mixed with aqueous solution containing ethylene glycol, NaOH and N_2H_4 were transferred into a Teflon-lined steel autoclave for 12 h at 140 C.

It could be found that the increasing dosage of nickel precursor in the synthesizing process caused a phase transformation from hexagonal α - Fe_2O_3 to cubic Fe_3O_4 , accompanying with the morphology change from hexagonal nanoplates to microcubes at the same time. One of the advantages of this method is generation of nanomaterials with high vapour pressures are produced with minimum loss of materials. (Balaprasad. 2021) reported the hydrothermal synthesis of iron oxide nanoparticles, where iron chloride hexahydrate precursor reacts with reducing agent hydrazine hydrate in presence of polyvinylpyrrolidone surfactant at basic pH. The results shows formation of rod shaped iron oxide nanoparticles with a mixture of γ - Fe_2O_3 maghemite and Fe_3O_4 magnetite that exhibited length of the iron oxide nanoparticles ranging from 138-250 nm, whereas width was in the range 38-50 nm. (Kongat *et al.*, 2021; Mitar *et al.*, 2021) has confirmed that surfactant and microwave aid in successful synthesis of size, phase and shape controlled hematite NPS using hydrothermal method. However this

method also has a disadvantage of generating nanomaterials which are not stable at elevated temperatures.

2.4.3 Co-precipitation

Another conventional method for the synthesis of Fe_3O_4 or $\text{c-Fe}_2\text{O}_3$ NPs is by co-precipitation. The method involves mixing of two Fe ions, which are ferric and ferrous ions in alkaline solutions at ambient temperature with or without any surfactant. The size, shape and phase of the iron oxide NPs are dependent on the type of salt employed (such as nitrates, chlorides, sulphates and perchlorates), the ratio of Fe^{3+} to Fe^{2+} ions, the temperature of the reaction, pH ionic strength of the solution and other reaction parameters such as stirring rate and the reaction environment such as an inert atmosphere (Wu *et al.* 2008). Kang *et al.* (1998) studied the synthesis of monodispersed, uniform Fe_3O_4 nanoparticles with an average particle size of 8.5 ± 1.3 nm via co-precipitation without using surfactants, with a molar ratio of $\text{Fe}^{2+}/\text{Fe}^{3+}$ of 0.5 and a pH values of 11-12. Wu, He & Jiang. (2008) also show a successful synthesis of monodispersed magnetite particles with an average size of 39 nm by co-precipitation at 70 °C with $\text{N}(\text{CH}_3)_4\text{OH}$ solution from ferrous Fe^{2+} and ferric Fe^{3+} .

Although the above-mentioned methods have been successfully used to synthesise iron oxide nanoparticles, there are several disadvantages, including high temperatures, complicated processes. More expensive material are required for hydrothermal and thermal decomposition methods to give good control over the size and shape of the nanoparticles. On the other hand, low control of particle shape, aggregation of particles and broad size distribution are reported for the co-precipitation method (Mascolo *et al.* 2013). A precipitation method would commercially be preferred due to its simplicity and cost benefits and thus was chosen as the ideal method for synthesis of iron oxide nanoparticles in this study. This study focusses on determining, which preparation parameters can give control of the size, shape and catalytic activity of the nanoparticles.

2.4.4 Precipitation and oxidation method

The precipitation and oxidation method is the simplest method used for the synthesis of controlled size Fe_2O_3 nanoparticles without any surfactant. This method has simple operation reaction process, time-efficiency and sometimes require a single step of synthesizing nanoparticles with different shape, size and phase (Wan *et al.*, 2016). As one of the most valuable methods, Fe^{2+} can be easily oxidised by introducing oxidisers in the absence of

nitrogen. However, the preparation Fe₂O₃ nano-powders and monodispersed Fe₂O₃ NPs by the oxidation-precipitation alone method is rarely reported.

Zheng *et al.* (2020) reported a successful synthesis of highly stable monodispersed Fe₂O₃ nanoparticles with particle sizes in the range of 5-12 nm from a combination of oxidation-precipitation under ambient air as an oxidising agent while altering the addition of NaOH amount in order to control the phase of the nanoparticles. To date, preparation of monodispersed Fe₂O₃ NPs with uniform controllable particle sizes and the unique properties of iron oxide using a simple precipitation-oxidation process alone is problematic. This study presents a simple approach towards the preparation of Fe₂O₃ NPs with long-term stability by H₂O₂ oxidation-precipitation with common and affordable bases and inorganic salts selected as raw chemicals for the preparations.

2.5 SYNTHESIS AND EFFECTS OF PREPARATION PARAMETERS ON THE SIZE AND SHAPE OF IRON OXIDE NANOPARTICLES

The synthesis of iron oxide NPs is performed at a very high salt and base concentrations. However, the advantage of this process is that there is no need of surfactant removal from the nanoparticles before their desired applications. In this work, a simple oxidation-precipitation method was used for synthesis of iron oxide nanoparticles in aqueous solutions without any surfactants.

In particular, the effects of precipitating agent, effect of temperature and the effect the amount of the precipitating agent on the formation of iron oxide NPs were investigated (Zheng *et al.*, 2020).

The preparation pathway in the process of oxidation-precipitation reaction is expressed by:

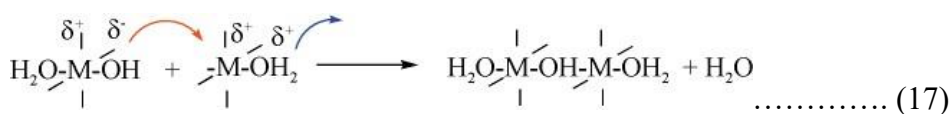


The formed Fe(OH)₂, is partially oxidised into Fe(OH)₃

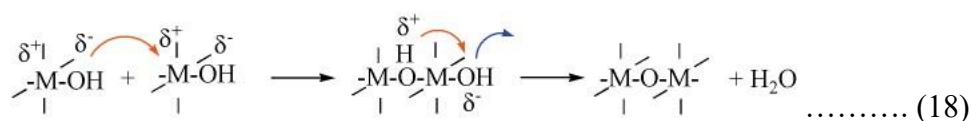


In the event where Fe(OH)₃ in (eq.15) above is unstable and results in FeOOH and Fe₂O₃, oxidation-oxalation process occurs and the following reactions are expected for iron cations in water.

Jolivet *et al.* (2019) reported that cations of iron tend to form aqua complexes of hexa-coordinated $[\text{Fe}(\text{OH}_2)_6]^{2+}$ in water. The coordinated H_2O molecules polarisation is then strongly dependent of the size and oxidation state of the cation, thus resulting in the ferrous complexes being less acidic than ferric aqua complexes. The hydroxylated complexes condensation occurs in two basic processes forming aquahydroxo and oxohydroxo complexes bridges by an olation-oxolation process(Jolivet *et al.*, 2019). In olation, water is eliminated from aquahydroxo complexes to form hydroxo bridges (Jolivet *et al.*, 2019). The reaction is expressed as:



For the oxolation process, the coordination sphere of oxohydroxo complexes does not contain water molecules, thus no leaving group present (Jolivet *et al.*, 2019) and the reaction is as follows.



2.5.1 Effect of the base type

The type of base used during preparation has been shown to influence the size and amount of agglomeration of the iron oxide nanoparticles since the base can potentially act like capping molecules during the formation of the nanoparticles. Mascolo *et al.* (2013) did a study of the compared potassium hydroxide with tetraethyl hydroxide as a base and found that the use of an organic amine base yielded nanoparticles that were less agglomerated, with sizes of 7.1 and 6.5 respectively. Santoyo-Salazar *et al.* (2011) used organic amine bases with varying chain lengths. The bases tested were tetramethylammonium hydroxide, tetraethylammonium hydroxide and tetrapropylammonium hydroxide. The resulted iron oxide particles showed a size decrease with an increase in the chain length. For a base to iron ion ratio of 3.8, the nanoparticle size range decreased from 40-35 nm, then 35-25 nm when the base was changed from tetramethylammonium hydroxide to tetraethylammonium hydroxide to tetrapropylammonium hydroxide. Therefore, based on the literature, one may suggest that the use of an organic base such as amines for the preparation of iron oxide NPs may assist in the size control of the NPs.

2.5.2 Effect of the amount of base

As stated in the literature that the type of base used during preparation has shown to influence the size and amount of agglomeration of the iron oxide nanoparticles since the base can potentially act like capping molecules during the formation of the nanoparticles as the amount of the base used, in addition of the base type can also influence the size, shape and the amount of agglomeration of the synthesised NPs. Based on the findings of Oh, Tajabadi and Khosroshahi *et al.*, (2012), when NH_4OH solutions with 0.9-2.1 mol were used as alkaline source, it is was observed that an increase in alkaline media concentration increased the particle size. The smallest particle size of 9.98 nm was obtained at alkaline media concentration of 0.9 mol at a temperature of 70 °C. Zheng *et al.* (2020) showed that the morphology of the monodispersed Fe_3O_4 NPs has also been affected by the amount of NaOH (base added). Their results show that when the addition amount of NaOH was relatively low (0.02 and 0.04 mol), the Fe_3O_4 NPs with a cubic or spherical morphology were obtained but when NaOH amount increased to is 0.06 mol, the phase composition of the spherical final product was a mixture of Fe_3O_4 and $\text{Fe}(\text{OH})_3$. Further increase with of NaOH amounts to 0.08 and 0.12 mol, resulted in rod shaped FeOOH nanostructures.

2.5.3 Effect of temperature

Mahdavi *et al.* (2013) found that Fe_3O_4 MNPs by chemical co-precipitation method particle sizes decreased when the temperature was increased from 25-45 °C and the size increased with a further increase in the temperature to 85 °C (see **Figure 2.1**). A minimum size of 8.3 nm was found at a temperature of 45 °C. Further increase in the temperature above 45 °C increased the size even more due to nucleation (small particles coming together to form larger particles as a result of nucleic growth), thus the XRD pattern of the material shows a more sharp peak. Based on the findings of Santoyo-Salazar *et al.* (2011), an increase in the hydrothermal treatment temperature from 150 °C-250 °C for 24 hr increased the size from 30-40 nm as a result of faster growth rate of nuclei due to longer exposure of the nanoparticles in higher temperature.

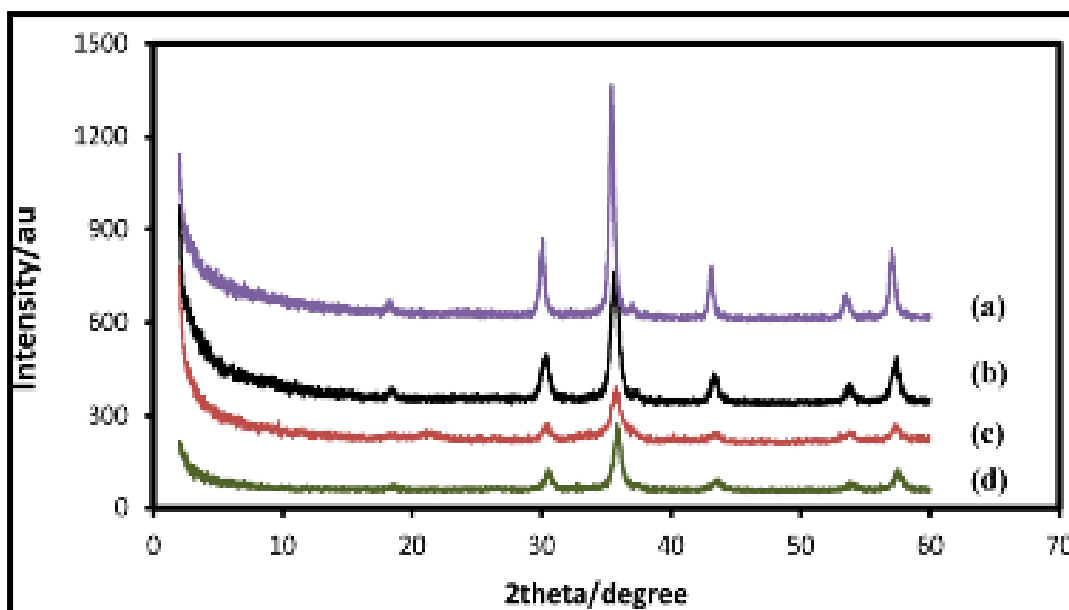


Figure 2.5: XRD patterns of the Fe_3O_4 at different temperatures; (a) 85 °C, (b) 65 °C, (c) 45 °C and (d) 25 °C (pH: 11) (Mahdavi *et al.*, 2013)

Another study by Oh, Tajabadi and Khosroshahi *et al.*, (2012) reports an effect temperature had on the synthesis of the Fe_3O_4 NPs. Their XRD analysis shows a decrease in particle size from 10.10-9.98 nm when the temperature was increased from 25-70 °C. It is observed that at elevated temperatures, smaller particle size and less crystal defects are achieved with the set reaction condition based on the co-precipitation method. The literature findings indicate that temperature has a significant effect on particle size and size distribution.

2.6 METHYLENE BLUE POLLUTANT AND DEGRADATION PATHWAYS

The release of large amounts of the coloured waste waters in the ecosystem into various bodies of water from industries, agriculture and households each day is a main source of non-aesthetic pollution, eutrophication and perturbation in the aquatic life (Wang *et al.*, 2012). Recalcitrant organic pollutants, particularly methylene blue (MB) dye, are harmful and need to be subjected to physicochemical approaches such as advanced oxidation process (AOP) to be degraded (Wang *et al.*, 2012). The following MB degradation (**Figure 2.2**) diagram are often applied in the cleaning-up of the water. The aromatic structure of the methylene blue dye and its degradation pathways are shown in **Figures 2.2 and 2.3**.

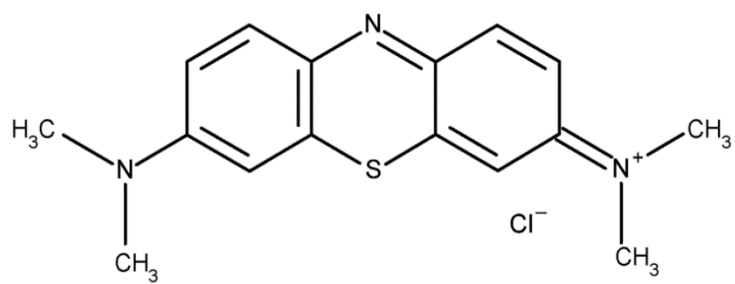


Figure 6.2: Structure of methylene blue dye (Wang *et al.*, 2012)

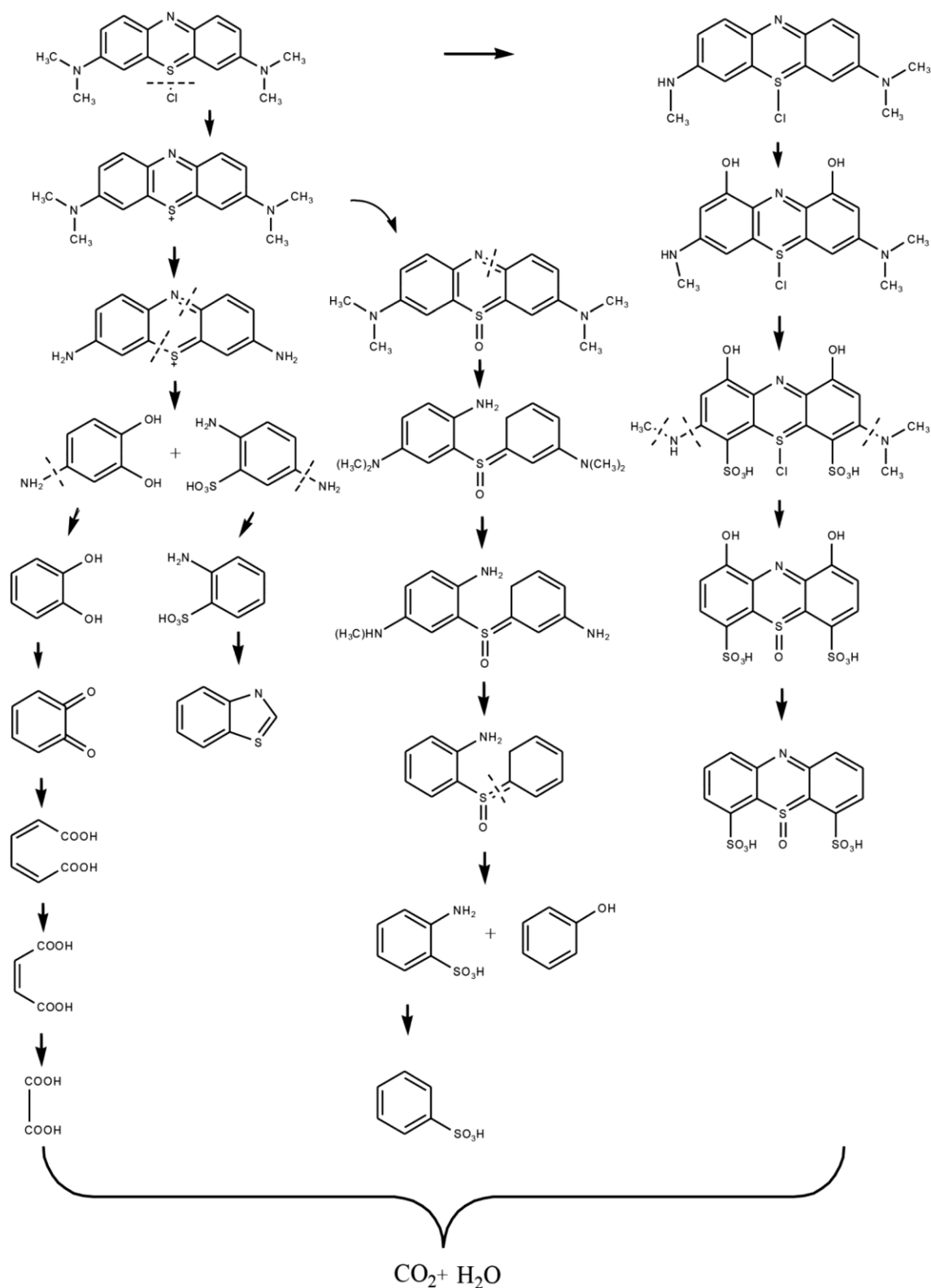


Figure 2.7: Degradation pathways of methylene blue dye (Wang *et al.*, 2014)

2.7 FACTORS THAT AFFECT FENTON CATALYTIC ACTIVITY

2.7.1 Effect of catalyst particle size

Wan *et al.* (2016) studied the effect of size on heterogeneous Fenton catalytic activities of Fe_3O_4 . They prepared spherical-shaped Fe_3O_4 particles with sizes of 30, 70, 250 and 600 nm catalyst. The efficiency of the nanoparticles increased with a decrease in the particle size. This could be explained by the smaller particles that had a higher number of active sites and high adsorption capacities because of their higher specific surface area in comparison to their volume ratio. Espinosa *et al.* (2018) showed that smaller iron oxide nanoparticles supported on hydroxylated surface of modified diamond were more active compared to larger supported iron oxide nanoparticles. The smallest particle tested by Wan *et al.* (2016) was 30 nm and one may argue that aiming for particles of smaller sizes than 30 nm could lead to a more active catalyst for the Fenton reaction.

2.7.2 Effect of phase on activity of iron oxide

Feng *et al.* (2016) studied on the effect of the oxidation state of iron in the oxide for the degradation of sulphanilamide. It was observed that Fe_3O_4 had higher removal efficiency as compared to Fe_2O_3 . Fe_3O_4 contains Fe^{2+} and is believed to be more reactive than Fe^{3+} towards H_2O_2 for the formation of hydroxyl radicals, thus leading to a larger amount of hydroxyl radicals being generated. In contrast, Rusevova *et al.* (2012) showed that the catalytic activity did not increase with an increase of the quantity of Fe^{2+} . They increased the amount of Fe^{2+} in their catalyst by the reduction of Fe_3O_4 with NaBH_4 . The increased amounts of Fe^{2+} in their catalyst did not increase the degradation catalytic activity since the increased amount of Fe^{2+} in their catalyst only led to the non-productive decomposition of the hydrogen peroxide to oxygen and water. Therefore one may conclude that the oxidation state of the iron in the oxide has no effect on the activity of the material.

2.7.3 Effect of oxidation state on size and activity of iron oxide

Frison *et al.* (2013) investigated the effect of size on the oxidation state (phase) of iron oxide nanoparticles with the range of 5-15 nm. The larger particles had a core-shell configuration with a magnetite (Fe_3O_4) core and a maghemite (Fe_2O_3) shell. The outer shell was more oxidised than the inner core. The smaller particles did not have a core-shell configuration since they were fully oxidised to maghemite. Carvalho *et al.* (2013) had similar research findings. They indicated that a nanoparticle smaller than 7 nm will not contain a shell but will be fully oxidised. Magnetite nanoparticles are prepared under an inert atmosphere to prevent them from

oxidising; however, if these particles are used as Fenton catalysts, they will be exposed to a very oxidising environment containing hydroxyl radicals, which will lead the magnetite to oxidise. It may thus not be useful to carefully prepare magnetite nanoparticles under inert conditions to yield a catalyst containing more Fe^{2+} ions on the surface.

2.7.4 Effect of shape on activity of iron oxide

Huang *et al.* (2016) study suggested that nanorods and nanoplates confined with ferrous ions indicated a higher formation of hydroxyls than the unconfined counterpart. Greater activity for degradation of organic pollutants was observed when the hematite shape was nanorods than nanoplate shaped. However, most researchers have reported efficient degradation of organic pollutants with iron oxide nanoparticles of small sized spherical shapes. Sun *et al.* (2016) study has shown that iron oxide nanocatalysts of nanotubes shapes have shown an improved catalytic activity as compared to nanorods shape, due to the interactions between the inside surface of the cavity and the reactant. Another study conducted by Zheng *et al.* (2006) revealed that quasicubic $\alpha\text{-Fe}_2\text{O}_3$ nanoparticles have 100 % catalytic performance as compared to those of other morphologies such as spherical and cubic. The exposure of crystal planes of $\alpha\text{-Fe}_2\text{O}_3$ nanocatalyst affect the catalytic activity, especially the external morphology for catalytic oxidation of CO.

2.7.5 Effect of type of capping agent and iron precursor on catalytic activity

The adsorbed capping agent on the nanoparticle surface tends to affect the catalytic activity of the catalyst material since it acts as dynamic shells or passivation coating, resulting in electronic and steric effects (Rossi *et al.*, 2018). Lee *et al.* (2011) reported that residuals of the capping agent on the surface of iron oxide can either have a negative or a positive impact on heterogeneous catalytic reactions. Their study also shows that nanoparticles of similar shape have different catalytic activities due to their synthetic route. A study by Radoń *et al.*, (2020) reported that treating Fe_3O_4 nanoparticle surface with malonic acid adversely influenced the catalytic activity in Fenton reaction, where their activities decreased from 86 % to 35% and from 93 % to 85.5 %, respectively, due to the malonic acid residuals blocking the active sites. However, the catalyst was reported to have more stability and less agglomeration.

Another study by Parimala *et al.* (2014) showed synthesis of iron nanoparticles with carboxymethyl cellulose (CMC), Polyethylene glycol (PEG) and poly N-vinyl pyrrolidone (PVP) as nanoparticle precipitating agent. The nanoparticles synthesised with PEG were found to exhibit smallest size of 9 nm, as compared to 14 nm and 17 nm of CMC and PVP,

respectively. The three prepared different iron nanoparticles (Fe NPs) were applied as catalysts for various substitution of aromatic ketones to alcohols with NaBH_4 with the progress of the reaction being monitored with time-variance UV spectra, kinetic plots and the pseudo-first order rate coefficient values in the hydrogenation reaction. The catalytic efficiency of the synthesised Fe NPs were found to be in the order $\text{PEG} > \text{CMC} > \text{PVP}$ for a single product, showing that better catalytic performance was obtained from nanoparticles synthesised with PEG. This could be attributed to the small particle size, which gave more room for adsorption of substituted aromatic ketones.

Neamtu *et al.*, (2018) has also evaluated the effect of the iron source precursor with iron (II) oxalate (FeO) and iron (III) citrate (FeC) on magnetite (M) nanoparticles stabilised with polyethylene glycol (PEG) on the catalytic activity of the nanoparticles. Their study shows that a complete photo-degradation of BPA was achieved when M/PEG/FeO catalyst was used in less than 15 minutes. The catalytic efficiency of the nanoparticles was established in this order: $\text{M/PEG/FeO} > \text{M/PEG/FeC} > \text{M/PEG}$. Di et al. (2020) synthesised iron catalyst with three different iron precursors: ferric nitrate $\text{Fe}(\text{NO}_3)_3$, ferrous sulfate FeSO_4 , ferrous oxalate using continuous co-precipitation method for the Fischer–Tropsch synthesis reaction to study their catalytic performance. When Fe-N was used as a precursor, Fe_2O_3 was obtained while Fe_3O_4 was obtained when Fe-S and Fe-C were used as precursors. In comparison with the other two catalysts, ferrous oxalate (Fe-C) has shown the highest catalytic activity, the best stability for the CO conversion with 96.16, 80.84 and 73.17 % for Fe-C, Fe-S and Fe-N respectively. One may conclude that the properties of iron precursors may be affect phase structure, morphology, reduction behaviours and catalytic performances of the catalyst.

2.7.6 Effect of induction period on activity

Xu & Wang. (2011) suggested that the inductive period is an activation process of the surface of iron species by dissolution and oxidation. The graph (see **Figure 2.4**) shows that a decrease in pH results in the disappearance of the induction period, which indicates that the pH of the solution plays a major role. When the pollutant is oxidised, organic acids like oxalic acid and acetic acid form and the pH drops, which in turn accelerates the rate of Fenton reaction.

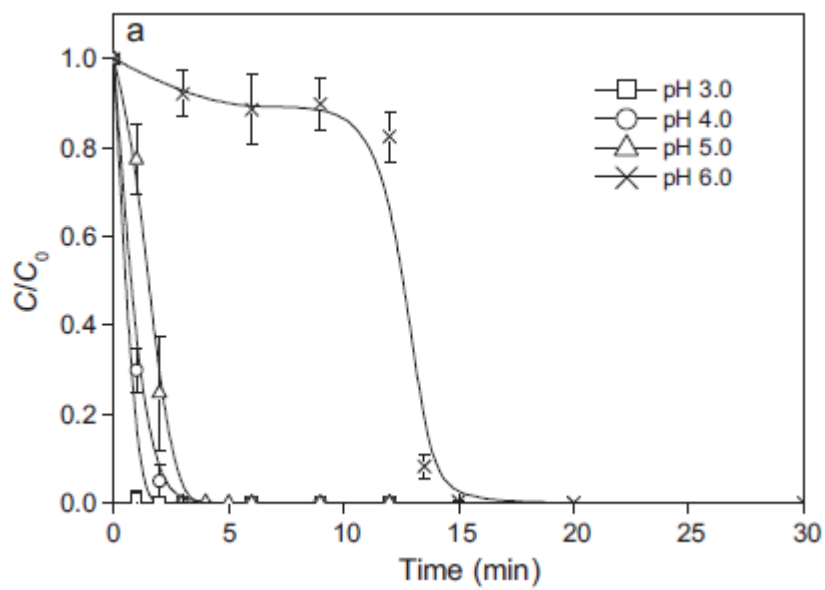


Figure 2.8: Effect of operating parameters on CMP degradation in the NZVI/H₂O₂ heterogeneous system: (a) pH (Xu & Wang, 2011)

CHAPTER 3

This chapter highlights the materials and methods used and a full description of the experimental setup and analytical instruments employed.

3. MATERIALS

Table 3.6: List of chemicals used, purity and suppliers

Chemicals	Purity (%)	supplier
FeCl ₂ .4H ₂ O (Iron (II) chloride tetrahydrate)	99.98 %	Sigma-Aldrich
Hydrogen peroxide (H ₂ O ₂)	30 %	Glass world
Hydrochloric acid (HCl)	37 %	Sigma-Aldrich
Sodium hydroxide (NaOH)	98 %	Glass world
Fe(NO ₃) ₃ .9H ₂ O(iron(III) nitrate anhydrous	99 %	Sigma-Aldrich
Tetraethylammonium hydroxide(N(C ₂ H ₅) ₄ -OH)	20 %	Sigma-Aldrich
tetramethylammonium hydroxide (N(CH ₃) ₄ -OH)	25 %	Sigma-Aldrich
Ethyl amine (C ₂ H ₇ N)	66-72 %	Sigma-Aldrich
Methylene blue (MB)	82 %	Sigma-Aldrich
Isopropanol	99 %	Glass world
Methanol	99 %	Glass world

All chemicals were used without any additional purification. Deionised water was used in preparation of solutions throughout the experiment.

3.1 NANOPARTICLES SYNTHESIS METHODS

3.1.1 Preparation of the iron oxide nanoparticles catalyst

The iron oxide particles were prepared with using two methods, namely the precipitation and oxidation method and the one-step oxidation-precipitation-oxidation method. In the precipitation and oxidation method, the iron salt was first precipitated with a base and thereafter oxidation-condensation occurs was carried using hydrogen peroxide to form iron oxide. In the

oxidation-precipitation-oxidation method, the iron salt was mixed with the hydrogen peroxide and oxidation of the iron (II) to iron (III) occurs. Thereafter, the iron solution was mixed with a base and the iron hydroxide precipitate that simultaneously underwent oxidation-condensation to form iron oxide.

3.1.1.1 Precipitation and oxidation method

A volume of 100 mL of water was mixed with a calculated amount of base (**Table 3.2**) in a three-neck flask (**Table 3.2 base type and amount**). The basic solution was either kept at room temperature or heated (**Table 3.2 Precipitation temperature**). Appropriate amount of an iron salt (**Table 3.2**) was dissolved in 10 mL of water at room temperature. The iron salt solution was added dropwise to the basic solution. Precipitation occurred to form iron hydroxide (Fe(OH)_2 or Fe(OH)_3) particles. The mixture was either kept at the precipitation temperature or further heated. After precipitation of the iron salt (Fe^{2+}) in to Fe(OH)_2 with OH^- from base, oxidation occurred and the temperature was denoted as the oxidation temperature. At the oxidation temperature 1 mL of 30 % H_2O_2 was added to the precipitate dispersion to oxidize the iron hydroxide to form iron oxide and the mixture was kept for a certain amount of time at the oxidation temperature to mature. Resulted solid metal oxide formed was cooled by placing the round bottom flask in cold water and then washed thrice with 0.1 M hydrochloric acid in order to dissolve the unreacted iron hydroxide molecules followed by washing with deionised water twice. Methanol was used for the final wash to remove water and the iron oxide nanoparticles was air dried for three days in the fume hood for characterisation using XRD, TEM and UV-Vis spectroscopy.

Table 3.7: Preparation conditions using the precipitation and oxidation (olation-oxolation)

Catalyst name	Iron salt	Iron salt (mol)	Base name	Base (mol)	Precipitation Temperature and time (°C, min)	Oxidation-Maturation temperature and time (°C, min)
M1	Fe(NO ₃) ₃ .9H ₂ O	0.02	NaOH	0.06	RT, 5	25, 60
M2	Fe(NO ₃) ₃ .9H ₂ O	0.02	NaOH	0.06	RT, 5	45, 60
M3	Fe(NO ₃) ₃ .9H ₂ O	0.02	NaOH	0.06	RT,5	65,60
M4	Fe(NO ₃) ₃ .9H ₂ O	0.02	NaOH	0.06	RT,5	85,60
M5	Fe(NO ₃) ₃ .9H ₂ O	0.02	NaOH	0.06	RT,5	100,60
B1	Fe(NO ₃) ₃ .9H ₂ O	0.02	(CH ₃ CH ₂) ₄ N-OH	0.06	85, 60	85, 30
B2	Fe(NO ₃) ₃ .9H ₂ O	0.02	(CH ₃ CH ₂) ₄ N-OH	0.09	85, 60	85,30
B3	Fe(NO ₃) ₃ .9H ₂ O	0.02	(CH ₃ CH ₂) ₄ N-OH	0.12	85,60	85,30
T1	Fe(NO ₃) ₃ .9H ₂ O	0.02	(CH ₃) ₄ N-OH	0.06	85,60	85,30
T2	Fe(NO ₃) ₃ .9H ₂ O	0.02	(CH ₃) ₄ N-OH	0.09	85,60	85,30
T3	Fe(NO ₃) ₃ .9H ₂ O	0.02	(CH ₃) ₄ N-OH	0.12	85,60	85,30

3.1.1.2 Oxidation-precipitation-oxidation method

A volume of 100 mL of water was mixed with a calculated amount of base (**Table 3.3**) in a three-neck flask (**Table 3.3 base type**). The basic solution was heated (**Table 3.3 Precipitation-oxidation temperature**). Appropriate amount of iron salt (**Table 3.3, iron salt type**) was dissolved in 10 mL of water and mixed with 1 mL of 30 % H₂O₂ at room temperature. Mixture of iron salt and H₂O₂ solution was added dropwise to the basic solution. Precipitation, oxidation and condensation occurred simultaneously to form iron oxide particles. The temperature of the basic solution when precipitation-oxidation occurs is denoted as to the precipitation-oxidation temperature. The mixture is either kept at the precipitation-oxidation temperature or heated to desired temperature and that temperature was denoted as the maturation temperature. Formed solid metal oxide was cooled by placing the round bottom flask in cold water and then washed thrice with 0.1 M hydrochloric acid to dissolve the unreacted iron hydroxide molecules followed by washing with deionised water twice, then with methanol for the final wash to remove water and air-dried for three days in a fume hood for characterised with XRD, TEM and UV-Vis spectroscopy.

Table 3.8: Preparation conditions using the oxidation-precipitation-oxidation (Olation-Oxolation)

Catalyst name	Iron salt	Iron salt (mol)	Base name	Base (mol)	Precipitation-Oxidation Temperature and time (°C, min)	Maturation temperature and time (°C, min)
MA1	FeCl ₂ .4H ₂ O	0.02	(CH ₃) ₄ N-OH	0.04	85,5	85,60
MA2	FeCl ₂ .4H ₂ O	0.02	(CH ₃ CH ₂) ₄ N-OH	0.04	85,5	85,60
MA3	FeCl ₂ .4H ₂ O	0.02	NaOH	0.04	85,5	85,60
MA4	FeCl ₂ .4H ₂ O	0.02	C ₂ H ₇ N	0.04	85,5	85,60
MM1	FeCl ₂ .4H ₂ O	0.02	(CH ₃) ₄ N-OH	0.04	25,5	25,60
MM2	FeCl ₂ .4H ₂ O	0.02	(CH ₃) ₄ N-OH	0.04	45,5	45,60
MM3	FeCl ₂ .4H ₂ O	0.02	(CH ₃) ₄ N-OH	0.04	65,5	65,60
MM4	FeCl ₂ .4H ₂ O	0.02	(CH ₃) ₄ N-OH	0.04	85,5	85,60
MM5	FeCl ₂ .4H ₂ O	0.02	(CH ₃) ₄ N-OH	0.04	105,5	105,60

3.2 CHARACTERISATION OF NANOPARTICLES

The synthesised catalysts were characterised using different techniques such as X-ray diffraction (XRD), UV-Vis spectroscopy, transmission electron microscopy (TEM), Fourier-transform infrared spectroscopy (FTIR) and photoluminescence spectroscopy (PL).

3.2.1 X-ray powder diffraction (XRD)

The X-ray powder diffraction spectra of iron oxide nanoparticles were obtained using a Shimadzu XRD-700 X-Ray Diffractometer Maxima., where Cu target K α -ray (operating at 40 kV and 40 mA, $\lambda = 0.15406$ nm) was used as the X-ray source. Crystals were finely crushed and evenly distributed on the small sample disc. The sample was placed on a sample holder inside the diffractometer. The scan range was from 15-80 ° 2theta with a step of 0.02 ° at a scan speed of 1°/min. The Shimadzu XRD Maxima has iron source and the scan was done at 40kV and 30 mA. The sample rotated at a rate of 60 rpm. The program Fityk was used to fit Gaussian peaks to obtain the FWHM values to calculate the crystallite size. The Scherrer equation was applied to calculate the size. It was assumed that the peak broadening is only from the small

size and therefore peak broadening possibly originating from the instrument and micro strain were assumed to be negligible.

The average crystallite size was calculated using the Scherrer equation. : $\tau = \frac{K\lambda}{\beta \cos \theta}$ (Eq. 3.1)

Where: τ is the mean size of the ordered (crystalline) domains

K is the Scherrer constant

λ is the wavelength

β is the line width at half of the maximum peak intensity on a 2θ scale

θ is the angle of the considered Bragg reflection

3.2.2 Fourier-transform infrared spectroscopy (FTIR)

FTIR was used for the characterisation of functional groups present in the synthesised catalyst in the range of 600-4000 cm^{-1} . FTIR spectra of synthesised catalyst samples vibrations were analysed on a Perkin Elmer spectrum 400 Fourier transform infrared spectrophotometer. A spatula tip of the dried nanoparticle samples was placed on the diamond cuvette on the FTIR instrument and the FTIR spectrum of the samples were collected.

3.2.3 Transmission electron microscopy (TEM)

The TEM images were collected using a HITACHI JEOL 100 S transmission microscope operated at 80 kV. For the sample preparation, samples were dispersed in toluene and a drop of the dispersion was placed on a carbon-coated copper grid and allowed to dry at ambient conditions. The nanoparticles samples were dried at room temperature prior to analysis. The shape and size of the dried sample was determined using HITACHI JEOL 100 S with an acceleration voltage of 120 kW and tungsten wire filament. The IONPs catalysts were finely crushed into 5 mL methanol in 30 mL sample bottles using a blunt smooth glass rod. Activated carbon-coated, copper grids were used for holding the finely methanol dispersed particles. The samples were left in a filter paper for complete drying. After the drying process, the samples were viewed under the TEM at different magnifications. Images were then taken with a Proscan slow scan CCC digital camera to establish the particles size and shape. The program ImageJ was used to measure the sizes of the nanoparticles. On average, about 20-100 particles were manually and randomly measured from the images for each catalyst at 95 % confidence level.

3.2.4 UV-Vis and PL analysis

UV-Vis spectra of the samples were obtained on T80+ a UV-Vis spectrophotometer. The nanoparticle particles were crushed using a mortar and pestle and a small amount (spatula tip) of the crushed crystals were transferred into sample bottles and dispersed in 10 mL distilled water, Then sample was placed in an ultrasonic bath for 30 minutes to ensure the dispersion of the nanoparticles and transferred into quartz cuvette (with path length of 1 cm) for analysis. Baseline was corrected using only distilled water in both 10 mm reference and sample cells. Distilled water was used for the reference and the spectrum was run between 1100 nm-190 nm. The concentration abatement of the pollutant was also monitored using UV-Vis spectroscopy at its wavelength of maximum absorbance of 664 nm. The photoluminescence properties of the catalysts were investigated on a LS 45 fluorimeter (Perkin Elmer) at the excitation wavelength from 200 nm- 400 nm.

3.3 FENTON DEGRADATION OF METHYLENE BLUE

3.3.1 Fenton catalytic decolourisation testing

To investigate the catalytic activity of the synthesised oxides for the degradation of the pollutant, 0.01 g of the catalyst were dispersed in 50 mL of distilled water and sonicated for 30 minutes in an ultrasonic bath. After this, 10 mL of methylene blue stock solution (1000 mg/L) and 20 mL of di-ionised water were then added and the mixture was stirred with a magnetic stirrer at 500 rpm until a temperature of 50 °C is achieved. The mixture was poured into the 250 mL beaker covered with a foil to prevent photodegradation stirred in the dark for 1 h to ensure adsorption-desorption equilibrium.

Fenton reaction was initiated with the addition of 20 mL of H₂O₂ (30%). At selected time intervals, 1 mL of the samples were collected and transferred into 100 mL volumetric flask, followed by addition of 1 mL isopropanol (OH radical scavenger) to quench the reaction The sample was then diluted with cold di-ionised water up to 100 mL and centrifuged for 5 minutes at 500 rpm for separation of solid catalyst from the liquid phase.

The methylene blue degradation rate was monitored for 3 hrs while collecting samples at selected time intervals and the diluted sample was then analysed by T80+ UV-Vis spectrophotometer to monitor the rate of methylene blue degradation. The catalysts (MM1, MM3, MM5, M1, M3, M5, MA1, MA2, MA3 and MA4) were selected for degradation tests and their kinetics models were also studied.

➤ **Reusability of the degradation runs**

According to the procedure outlined in 3.3, under the following optimised conditions. The reusability experiments were performed to investigate the MB concentration in solution versus following the conditions: 50 °C, 100 mg/L MB, 0.1003 g iron oxide catalyst and H₂O₂ = 20 mL. After each run, the iron oxide catalyst particles suspended in solution were filtered out, rinsed with water, dried at room temperature, weighed and further used in the first, second and third rounds. The weighed mass after each run is shown in **Table 4.4**.

3.3.2 Effect of degradation temperature

Reaction temperature is part of the important operational parameters influencing the efficiency of a catalytic oxidation process. Effect of reaction temperature on the degradation of 10 mg/L MB in the presence of 20 mL H₂O₂ and 0.1003 g iron oxide was also tested at temperatures 27, 50, 70 °C using the method stated in 3.3.1 and the result is shown in **Figure 4.33**.

3.3.3. Effect of the dosage of H₂O₂ on the degradation of MB

Hydrogen peroxide (H₂O₂) serves as the source of •OH radicals, the amount of H₂O₂ used may affect the efficiency of the Fenton catalytic degradation process. Thus, the effect of the amount of H₂O₂ (20,40 and 60 mL) on the degradation was studied with initial methylene blue concentration of 10 mg/L at temperature of 50 °C, in the presence of 0.1003 g catalyst as described by the Fenton catalytic testing method in 3.3.1. The following dilutions (Table 3.4) were made to ensure that the concentration of MB remains at 100 mg/L.

Table 3.4: Measured MB, H₂O₂ and H₂O at each reaction

MB Volume (mL)	H ₂ O Volume (mL)	H ₂ O ₂ Volume (mL)
10	70	20
10	50	40
10	30	60

CHAPTER 4

RESULTS AND DISCUSSIONS (PART 1)

The chapter is divided into two sections. The first section consists of the optimisation of the synthesis of the iron oxide and its characterisation using FTIR, XRD, TEM, UV-VIS and PL analysis. The second section discusses the Fenton catalytic degradation of methylene blue solution conducted in the presence of heterogeneous catalysts with parameters varied during MB removal reaction/process and their removal efficiencies.

4.1 EFFECT OF TEMPERATURE OF REACTION ON SYNTHESIS OF IRON OXIDE NANOPARTICLES.

The parameters that were used to prepare the catalyst are summarised in **Table 3.2** in **chapter 3**. In this method the iron nitrate was precipitated with stoichiometric amount of optimum precipitating agent NaOH and the precipitate was subsequently oxidised with hydrogen peroxide as oxidising agent. The reaction temperature varied from 25 °C to 85 °C keeping reaction time at 1 hr and discussed in this section.

4.1.1 XRD ANALYSIS

Figure 4.1 shows the XRD patterns of the synthesised samples, in comparisons to the XRD reference spectra of orthorhombic phase goethite [01-075-550565] and rhombohedral phase hematite [01-073-8431]. At temperatures of 25, 45 and 85 °C, the XRD patterns shows that the samples exhibit a highly amorphous peaks and the crystallite sizes are hard to calculate, thus may be assumed to be < 5 nm as shown in Figure 4.1(a). At a temperature of 65 °C in Figure 4.1(b), the XRD patterns shows narrow peaks and indexed to a mixture of orthorhombic phase of goethite and rhombohedral phase of hematite with an average particle size of 10.2 and 19.3 nm respectively for each iron oxide phase. At the highest reaction temperature of 100 °C in Figure 4.1(b), the diffraction pattern shows that the peaks become slightly broader than the peaks obtained for a preparation temperature of 65 °C and were indexed to hematite [01-073-8431] with a rhombohedral phase and an average crystalline size of 19.3 nm. The diffraction peaks were narrower when the nanoparticles were prepared at 65 and 100 °C which shows change in the strain/crystallinity, however in terms of the crystallite sizes, it is difficult to compare the materials in (a) to those in (b) since there are no visible peaks in (a).one can deduce that the nanoparticles become larger (see the zoomed out TEM images in figure 4.2(b) below.

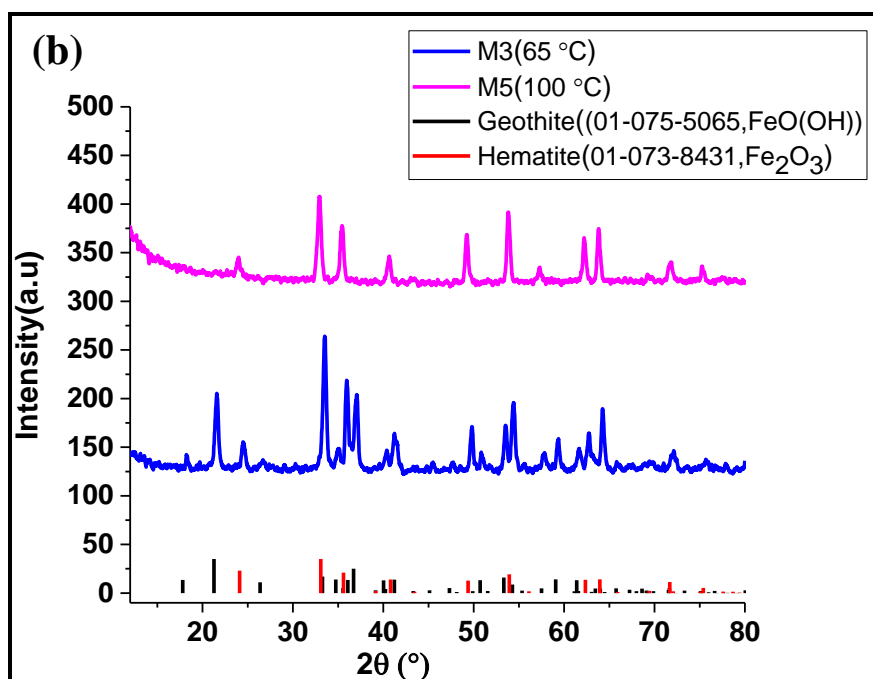
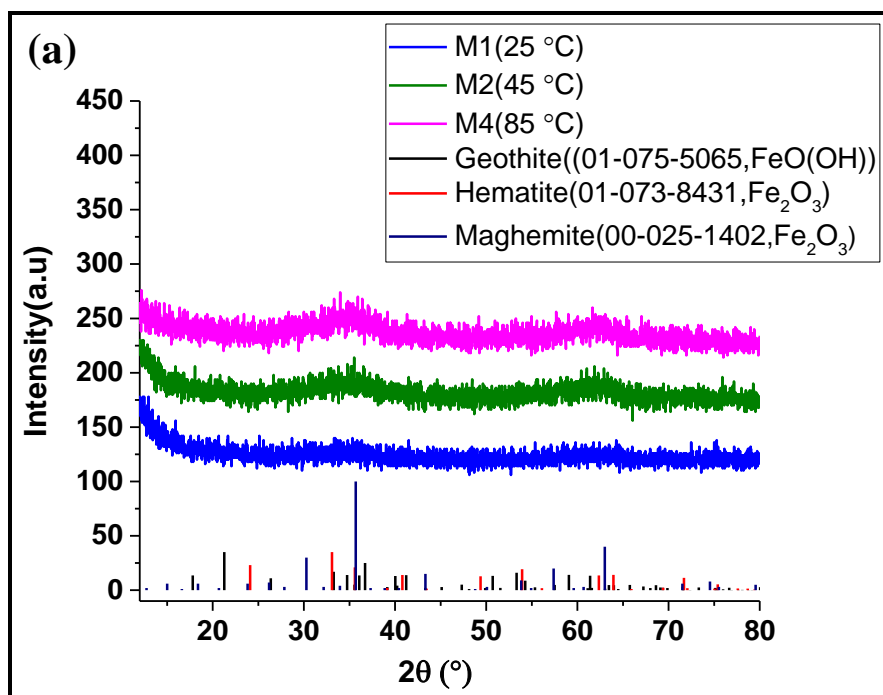


Figure 4.1: XRD patterns of iron oxide nanoparticles prepared at (a) 25, 45 and 85, (b) 65 and 100 °C

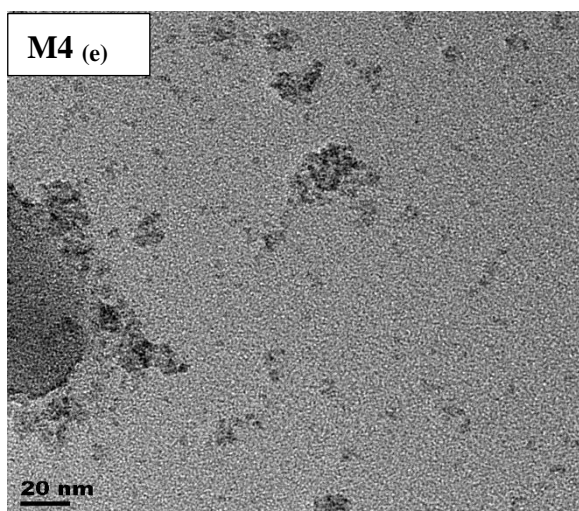
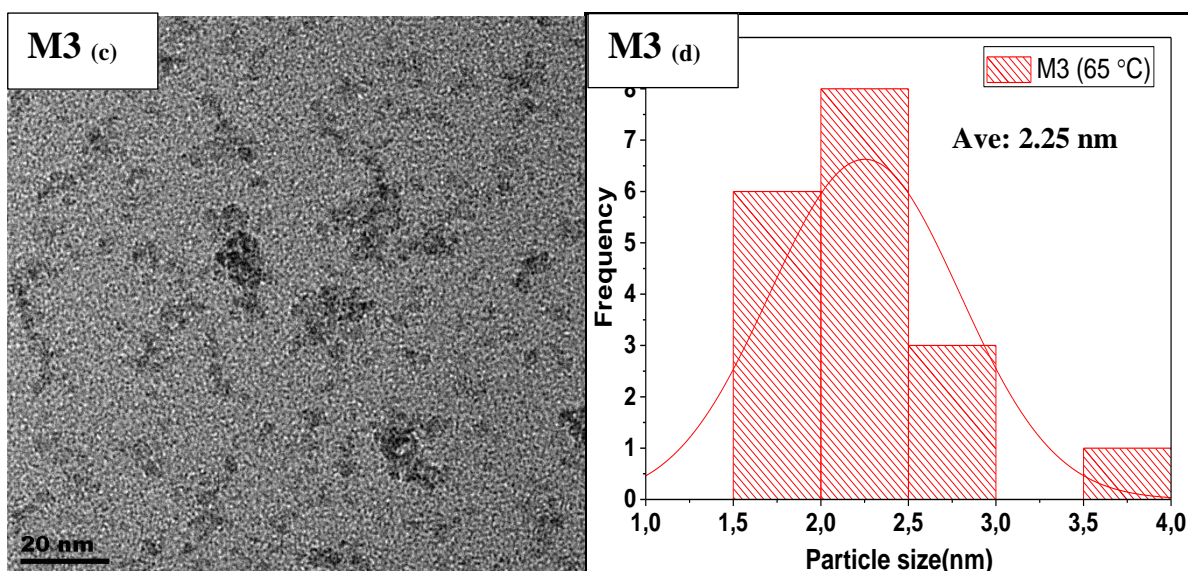
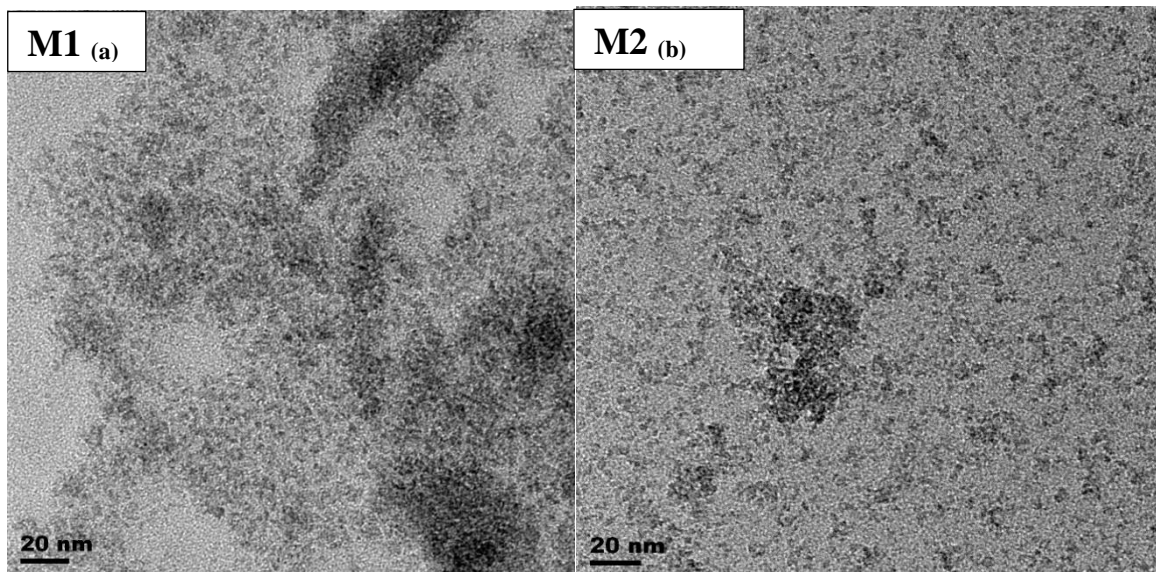
The average crystallite sizes shown in **Table 4.1** were calculated from the full width at half maxima of the FeOOH for Figure 4.1(b)

Table 4.1: Calculated crystallite sizes calculation XRD

Sample name	Temperature (°C)	Angle (2 θ °)	Average size (nm)
M1	25	-	<5 nm
M2	45	-	<5 nm
M3	65	21.66 & 24.10	10.2 & 19.3 nm
M4	85	-	<5 nm
M5	100	24.13	19.3 nm

4.1.2 STRUCTURAL ANALYSIS (TEM)

The influence of synthesis conditions (temperature) on the morphology was analysed by TEM (**Figure 4.2**). The TEM showed the formation of spherical nanostructures with an estimated average particle size of about 2 nm for M1(a), M2(b), M4(e) and 2.3, 2.1 nm for M3(c,d), M5(f, g) respectively. These sizes are smaller than that estimated by XRD and it may be that there were larger particles, which were not visible in the TEM images. As evidenced by TEM images the particles in the image M1 (a), M2 (b) and M4 (e) synthesised at temperatures of 25, 45 and 85 °C are very small, aggregated and have indistinct boundaries, thus it is not possible to obtain accurate size values. The XRD patterns in support of the TEM images also shows that these nanoparticles prepared at temperatures lower than 65 °C are very small. Upon increasing the preparation temperature from 25-100 °C, the particles morphology was found to be composed of smaller and randomly oriented interconnected particles, which suggests the occurrence of a polycrystalline material, which also contributed to difference in particles sizes obtained from XRD calculation. The temperature can influence both the rate of nucleation and growth (Wei *et al.*, 2017). An increase in the rate of nucleation is expected to decrease the average size and an increase in the rate of grow is expected to increase the average size of the nanoparticles. One could speculate that the rate of growth increased when the temperature was increased due to the size increase as shown by the zoomed TEM images in M3(h) and M5(i).



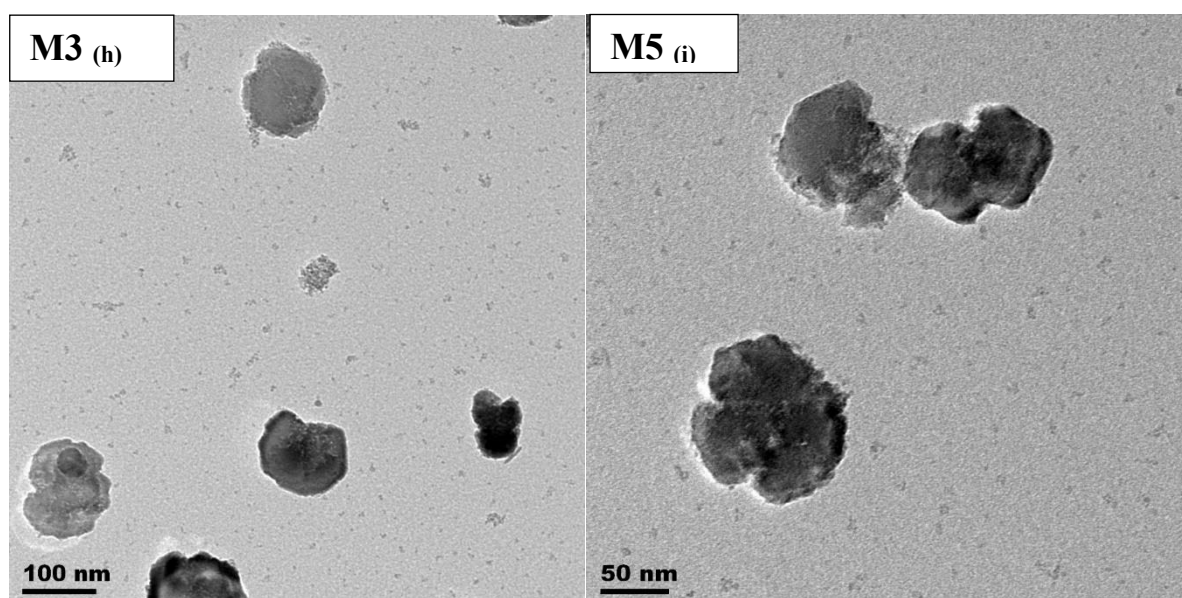
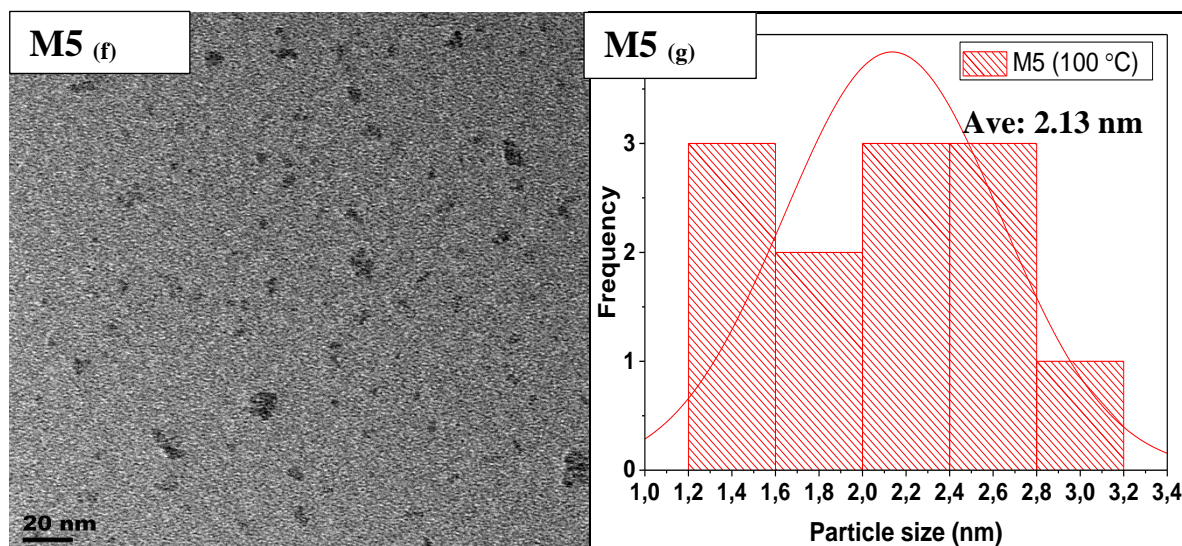


Figure 4.2: TEM images and histogram of iron oxide nanoparticles prepared at different temperature with M1 (a):25 °C, M2 (b):45 °C, M3 (c, d) 65 °C, M4 (e): 85 °C, M5: (f, g) 100 °C and zoomed out M3 (h) and M5 (i)

4.1.3 FTIR ANALYSIS

The chemical and structural changes that occurred during the temperature change were monitored by FTIR analysis. **Figure 4.3** shows the FTIR spectra of the dried nanoparticles at 25-100 °C in the range of 470-4200 cm^{-1} . The dried powder of sample M1-M5 showed the characteristic bands at

about 3700 and 2988-2901 cm^{-1} corresponding to the O-H group from the water adsorbed on the surface of iron oxide nanoparticles from the washing process and from the precipitating agent NaOH, 1405-1256 cm^{-1} stretching is attributed to N-O from the nitro compounds which indicates that the washing process was not effective enough to remove all the organic and at around 570 cm^{-1} vibrations are attributed to the Fe-O of FeOOH. At 65 °C the O-H stretching is stronger compared to the O-H at temperatures of 25, 45, 85 and 100 °C, which could be due to mixture of phases as confirmed by XRD, which resulted with the sample being more oxygenated, which shows temperature had an effect on the surface of the nanoparticles.

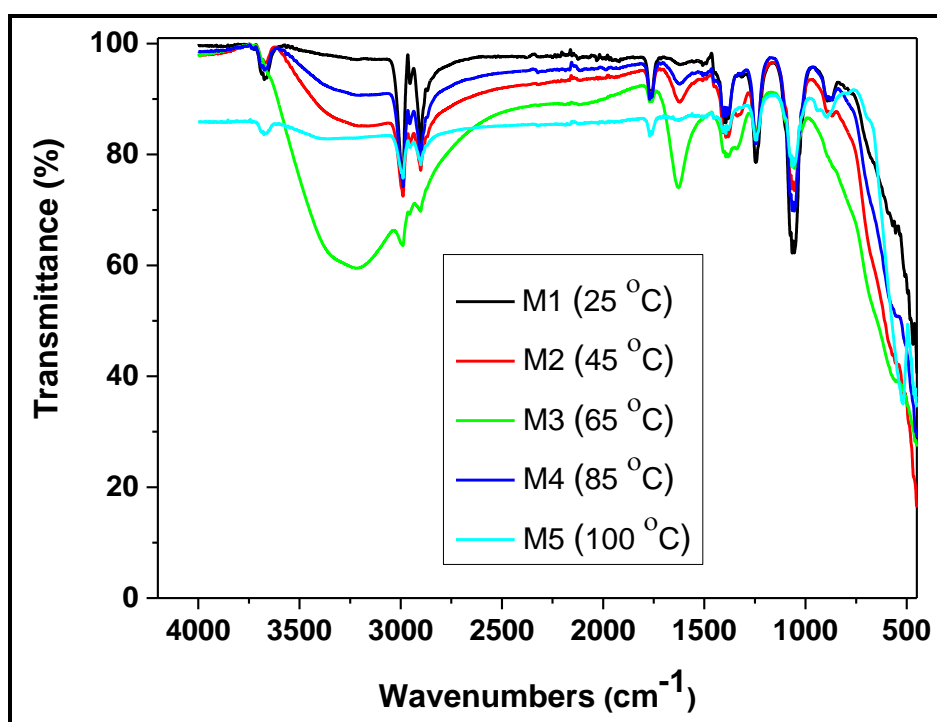


Figure 4.3: FTIR Spectrum of iron oxide nanoparticles prepared at different temperature with M1:25 °C, M2:45 °C, M3:65 °C, M4: 85 °C and M5:100 °C

4.1.4 UV-VIS AND PL RESULTS

Optical properties of the samples were investigated using UV-Vis. **Figure 4.4(a)** shows the optical absorption spectra of iron oxide nanoparticles prepared at different temperatures. It can be observed that all the samples show strong absorptions in the near UV region extending to the lower wavelength of the visible region (~550 nm). This absorption is responsible for their red-brownish color of the iron oxides. The peak maxima of absorptions for the particles prepared at 65 °C and 100 °C were at higher wavelengths than those prepared at the other temperatures. A smaller band gap are thus present for the particles prepared at 65 °C and 100 °C. This is indicative of smaller band gap energies. The

band gap is expected to decrease when the particle size increases (Vidyasagar *et al.*, 2012). Therefore, the smaller band gaps indicate that the particles are larger when preparation temperatures of 65 °C and 100 °C were used in comparison to the other preparation temperatures, this confirms the finding of the XRD diffratograms that indicated that the particles prepared at 65 °C and 100 °C were larger than those made at the other temperatures. The following band-gaps values were collected from Tauc plots in **Figure 4.4 (b)** with the assumption of a direct transition. Where band-gaps of 2.1 eV, 2.0 eV, 1.8 eV, 1.7 eV and 1.9 eV for particles grown at 25, 45, 65, 85 and 100 °C, respectively are observed. These values are significantly red-shifted with respect to the literature data for bulk iron (III) oxides, which are typically close to 2.10-2.50 eV of goethite (Zhang *et al.*, 2011) and hematite 1.9-2.2 eV (Schwaminger *et al.*, 2017).

A similar finding by Schwaminger *et al.*, (2017) suggests that hematite have distinct absorption at around 300 nm, 420 nm and around 550 nm regions, which is due to different transitions. The difference in ligand-field transitions are dependent on the binding state of Fe^{3+} ions and ligand-to-metal charge transfer transitions lead to the absorption spectra of the nanoparticle in M3 and M5. The double excitation process and the corresponding absorption around 425 nm for M3 and M5 belong to the $\text{O}(2p) \rightarrow \text{Fe}(3d)$ charge transfer and broad absorption with the edge at 495 nm is due to the ligand field ($\text{Fe } d \rightarrow d$) transitions. This double excitation process is also responsible for the observed red colour of hematite and goethite mixture in a sample (Qi, 2013)

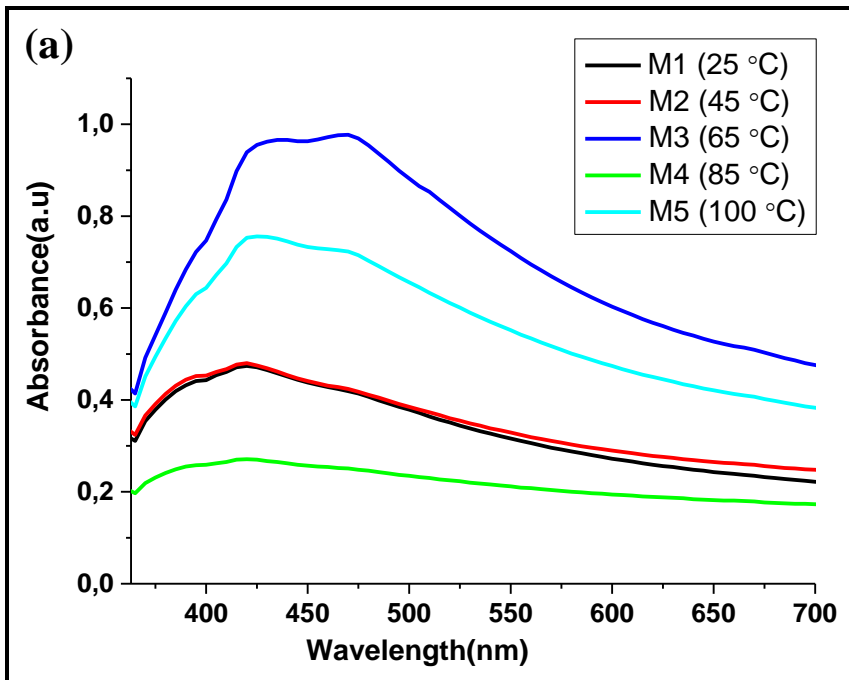


Figure 4.4: (b) Absorption of iron oxide nanoparticles synthesised at different temperature with M1:25 °C, M2:45 °C, M3:65 °C, M4: 85 °C and M5:100 °C

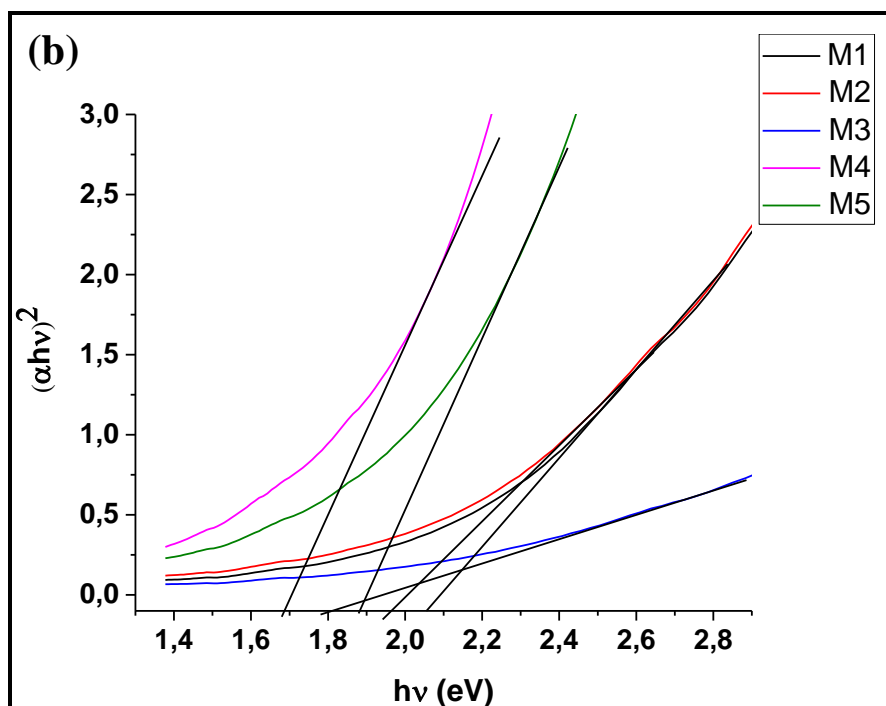


Figure 4.4: (b) Tauc plot for direct bandgap of goethite and hematite nanoparticles. The intercept of a black lines with the horizontal axis defines the value of the bandgap at different temperature with M1:25 °C, M2:45 °C, M3:65 °C, M4: 85 °C and M5:100 °C

The photoluminescence properties of iron oxide nanoparticles are shown in **Figure 4.5**. The nanoparticles were excited at 400 nm wavelength as obtained in the UV-Vis absorption bands for M1-M5. All the obtained nanoparticles samples were found to have an emission peak at 425 nm, which is similar to the first absorption peaks observed for UV-Vis analysis in **Figure 4.4(a)**, suggesting that the emission wavelength is independent of the particle's size, since all obtained nanoparticles samples gave the same wavelength. The peak intensities of particles at 25,45 and 85 °C are more higher than that of particles obtained at 65 and 100 °C, this could be as a results of smaller particles sizes allowing more light to penetrate between the colloids as compared to those with larger particle sizes.

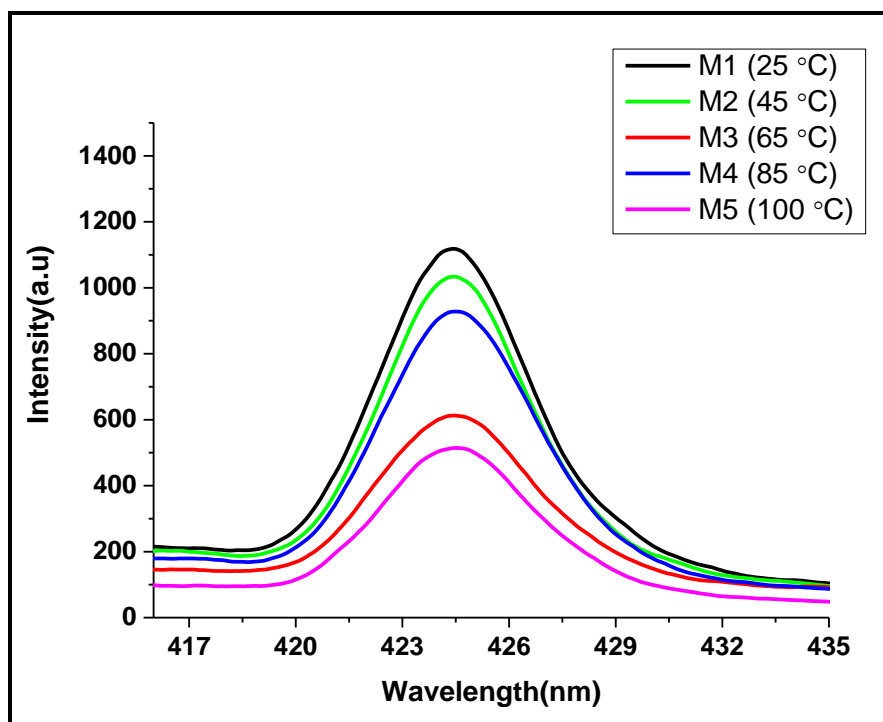


Figure 4.5: Emission spectrum of iron oxide nanoparticles synthesised at different temperature with M1:25 °C, M2:45 °C, M3:65 °C, M4: 85 °C and M5:100 °C

The synthesis conditions (temperature) show that different phases of the iron oxide nanoparticles were successfully synthesised with different particle size and spherical shape as observed by XRD and TEM analysis. The XRD analysis of the synthesised samples shows that as the temperature increased also the diffraction peaks were narrower when the nanoparticles were prepared at 65 and 100 °C a change in the strain/crystallinity. TEM analysis also shows that particle shapes and sizes were nearly unaffected by the difference of the preparation temperature. FTIR shows a more intense O-H functional group at sample obtained at the temperature of 65 °C compared to samples obtained at 25, 45, 85 and 100 °C, which could be due to the mixture of phases. The UV-VIS analysis shows that the all samples are red-shifted with $O(2p) \rightarrow Fe(3d)$ and $(Fe d \rightarrow d)$ different transitions observed at other temperatures. However, the samples obtained at all synthesis temperatures shows less photo luminance properties in terms of wavelength as supposed to intensities as a result of different particle sizes .

4.2 EFFECT OF AMOUNT AND TYPE OF PRECIPITATING AGENT

The effect of the amount and type of ammine (tetraethyl ammonium hydroxide, TEAOH, $(\text{CH}_3\text{CH}_2)_4\text{N-OH}$ and tetramethylammonium hydroxide, TMAOH $(\text{CH}_3)_4\text{N-OH}$) were investigated and discussed in this section. Investigated parameters are shown in **Table 2.3** in chapter 3 for samples T1, T2, T3, B1, B2 and B3.

4.2.1 XRD ANALYSIS

The XRD patterns shown in **Figure 4.6 (a) and (b)** represent iron oxide nanoparticles prepared at 1.0, 1.5X and 2X the stoichiometric amounts for TMAOH and TEAOH, respectively. The diffraction patterns in Figure 4.6 (a): T2-T3 and Figure 4.6 (b): B2-B3 are highly crystalline exhibiting reflections peaks at 020, 110, 120, 130, 040, 111, 220, 141, 231, 151 and 042 are relatively indexed to the major peaks goethite reference spectra [01-075-550565] with orthorhombic phase and traces amounts of hematite [01-073-8431]. The sharp peaks at $2\theta = 21.07^\circ$, 33.04° and 36.07° for T2-T3 in Figure 4.6(a) became more prominent indicating that the nanoparticles becomes more crystalline and larger. The same trend was observed in Figure 4.6 (b) at $2\theta = 21.36^\circ$, 33.31° and 36.12° . The increase of the precipitating agent amount to 1.5X and 2X for both precipitating agents (TMAOH and TEAOH) enhanced the crystallisation of iron oxide nanoparticles and accelerated transformation of amorphous phase into crystalline orthorhombic phase. Therefore, it may be concluded that amount of the base during reaction affects the crystallinity of the synthesised nanoparticles.

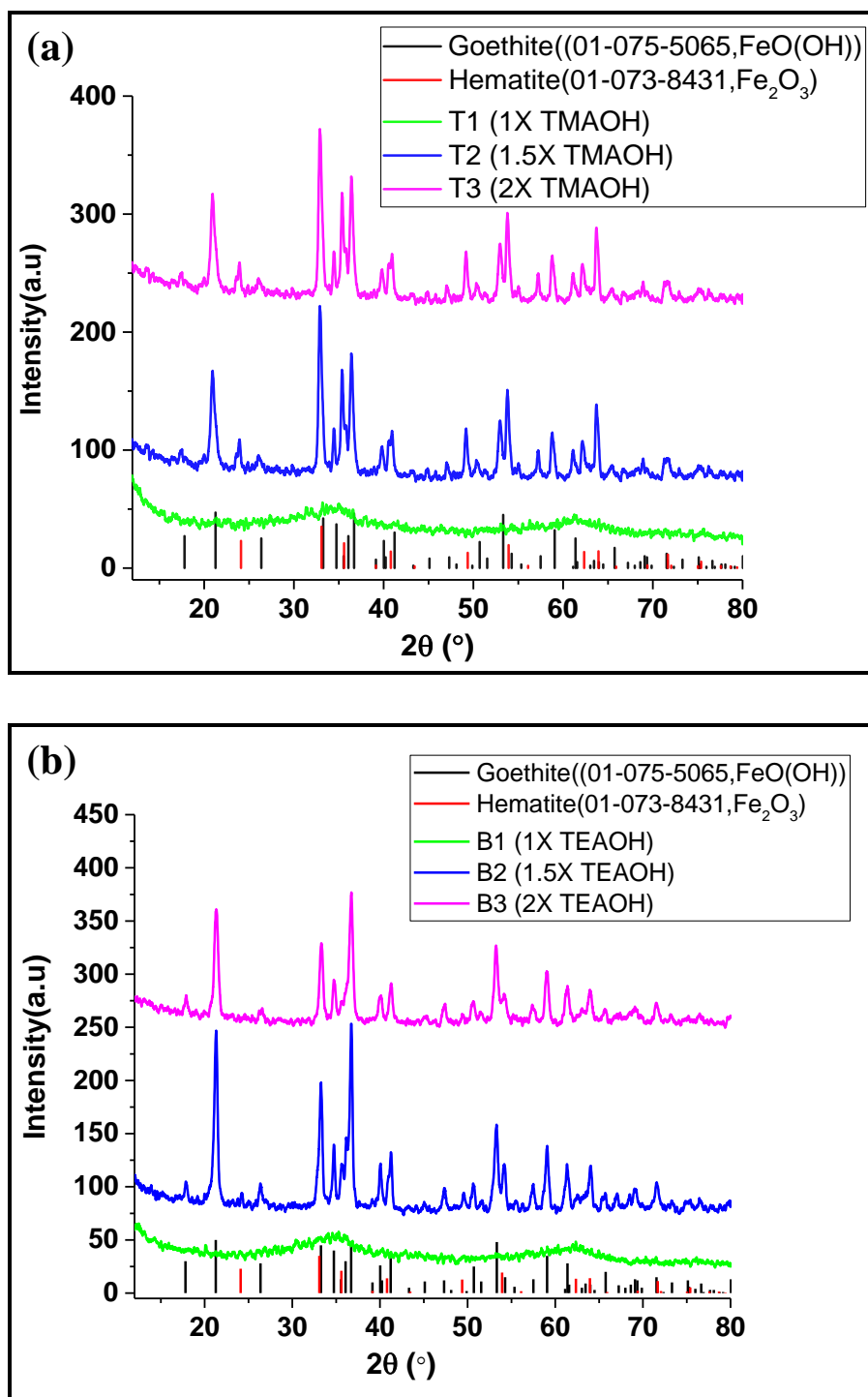


Figure 4.6: XRD patterns of iron oxide nanoparticles prepared at amine amounts of TMAOH (a): T1 0.06 mol, T2 0.09 mol, T3 0.12 mol, TEAOH (b): B1 0.06 mol, B2 0.09 mol and B3 0.12 mol

The average crystallite sizes shown in Table 4.2 were calculated from the full width at half maxima of the FeOOH for Figure 4.6 (a): T2-T3 at $2\theta = 21.07^\circ$ for TMAOH and **Figure 4.6(b):** B2-B3 at $2\theta = 21.36^\circ$ for TEAOH diffraction peaks using the Scherrer equation. The smallest FeOOH nanocrystallites formed when a stoichiometric amount of precipitating agents was used.

Table 4.2: Calculated crystallite sizes calculation XRD

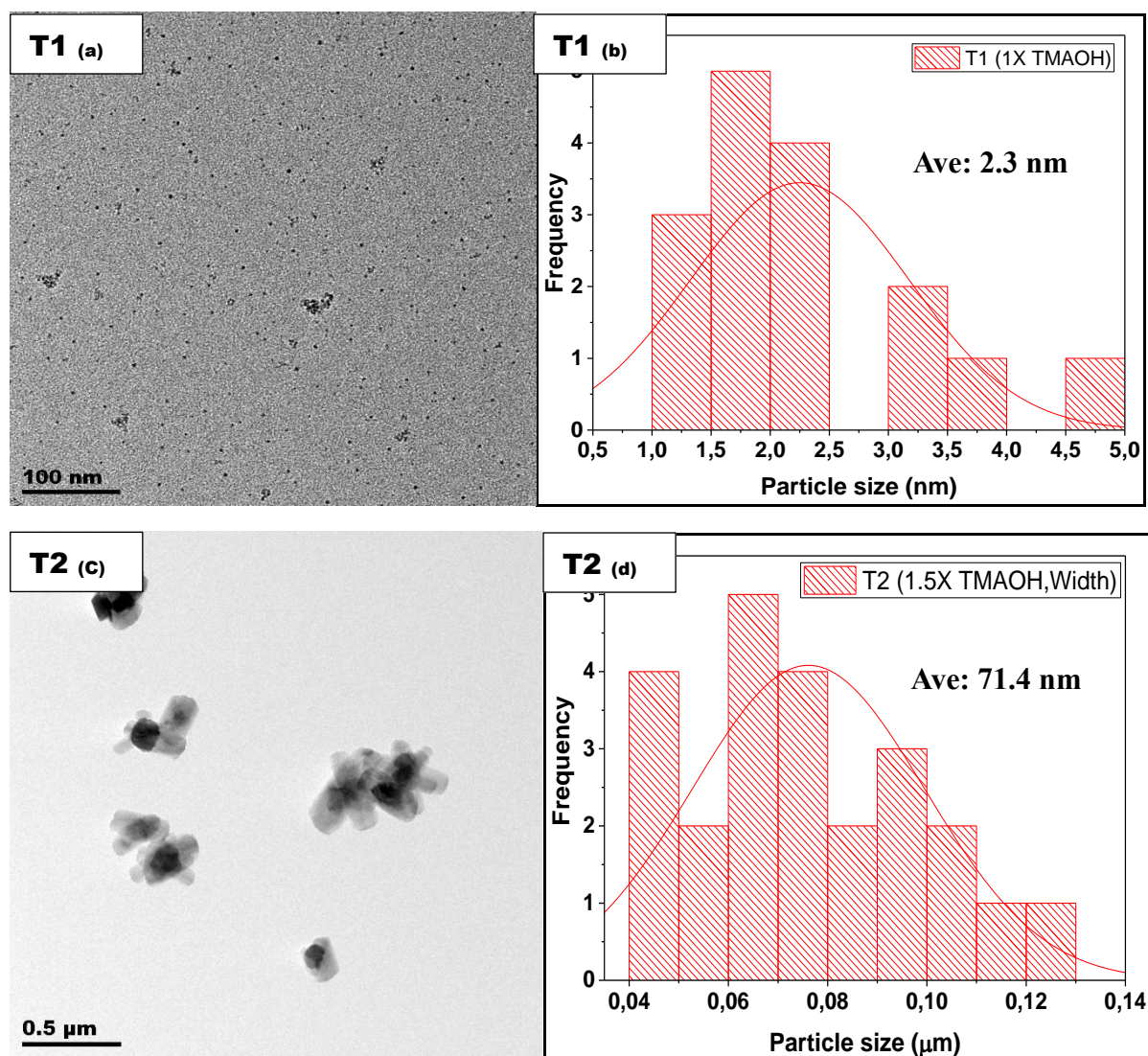
Sample name	Angle (2 θ (°))	Average size (nm)
T1	-	<5 nm
T2	21.07	6.5
T3	21.07	6.6
B1	-	<5 nm
B2	21.36	8.3
B3	21.36	7.8

4.2.2 TEM ANALYSIS

Figure 4.7 and 4.8 shows the TEM images for iron oxide nanoparticles prepared at 1.0, 1.5 and 2.0 times the stoichiometric amounts of TMOAH and TEAOH. The TEM images and particle size distributions for particles prepared at the stoichiometric amounts of TMOAH and TEAOH ammine shown in **Figure 4.7.: T1 (a, b)** and **Figure 4.8: B1 (a, b)** shows a uniform well dispersed spherical shapes for iron oxide nanoparticles with the particle average size of 2.3 ± 0.93 and 2.5 ± 0.70 nm respectively for T1 and B1. When the ammine was increased to 1.0-1.5 times the stoichiometric amounts for TMOAH, the nanoparticle's shape changed from spherical to irregular flower-like shape (hexagonal with rods extensions) with an increased particles size particle size from 2.3-71.4 nm. Similarly the same trend was observed with TEAOH with particle size of 2.5-73.1 nm, as observed in as the ammine is increased to 1.5 times and 2.0 times. The stoichiometric amounts for TMOAH, the nanoparticle remained irregular flower-like shape (hexagonal with rods extensions) with a decreased particles size particle size of 71.4-50.3 nm and the same trend was observed with TEAOH with particle size of 73.1-52.4 nm.

It can be observed that as the particle size increase, the particle shape also changed drastically and this could be resulting from the faster growth rate of nuclei at 1.5 times and 2.0 times the stoichiometric amounts of the amines as a result of more OH groups on the surface at higher base leading to more oxalation/olation. Similarly, Oh, Tajabadi & Khosroshahi *et al.*, 2012, observed that the use of 0.9-2.1 mol of NH_4OH as a precipitating agent affected the sizes and shapes of particles. Tis was linked to the balance between nucleation and growth rates and when all reactants were used-up no particle growth is expected, rather the Ostwald ripening and aggregation of the particles could result in the increase in the particle size. Also, it was reported that when the addition of the alkaline species and iron salts has occurred, some cations of NH_4 and other intermediate products such as

Fe(OH)_2 and Fe(OH)_3 were produced. Once the iron oxide nuclei are produced, particle aggregation or Ostwald ripening (larger particles grow at the expense of dissolving smaller one) caused the particle growth (Oh, Tajabadi & Khosroshahi *et al.*, 2012), therefore, one can assume that the same phenomena occurred when the use of alkane base and the increase of the ingredient (alkaline media) concentration may be the cause of the shape and size changes as observed in TEM images in Figures 4.7 and 4.8.



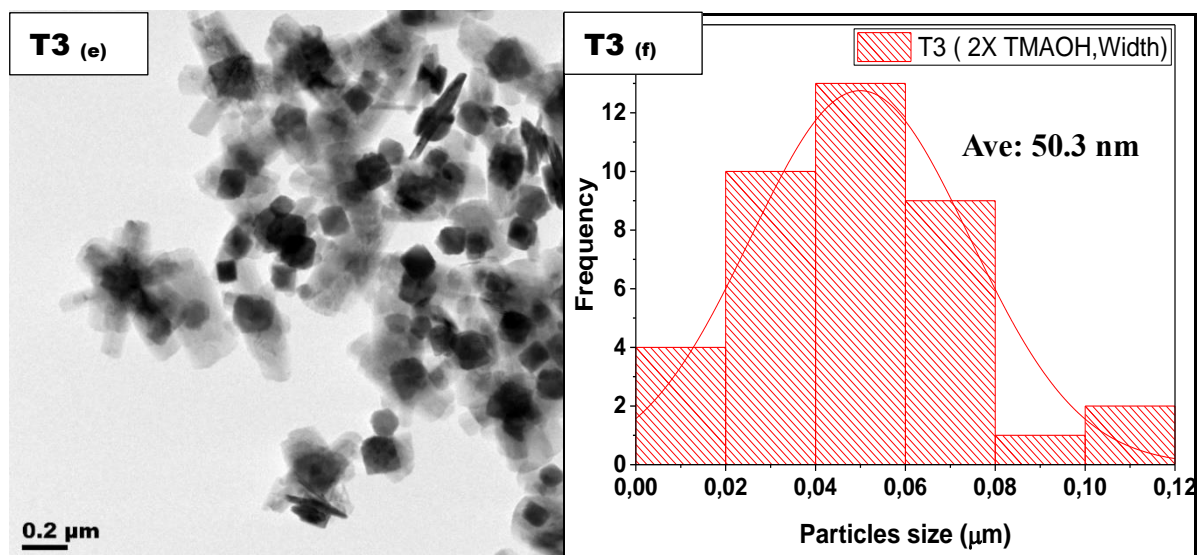
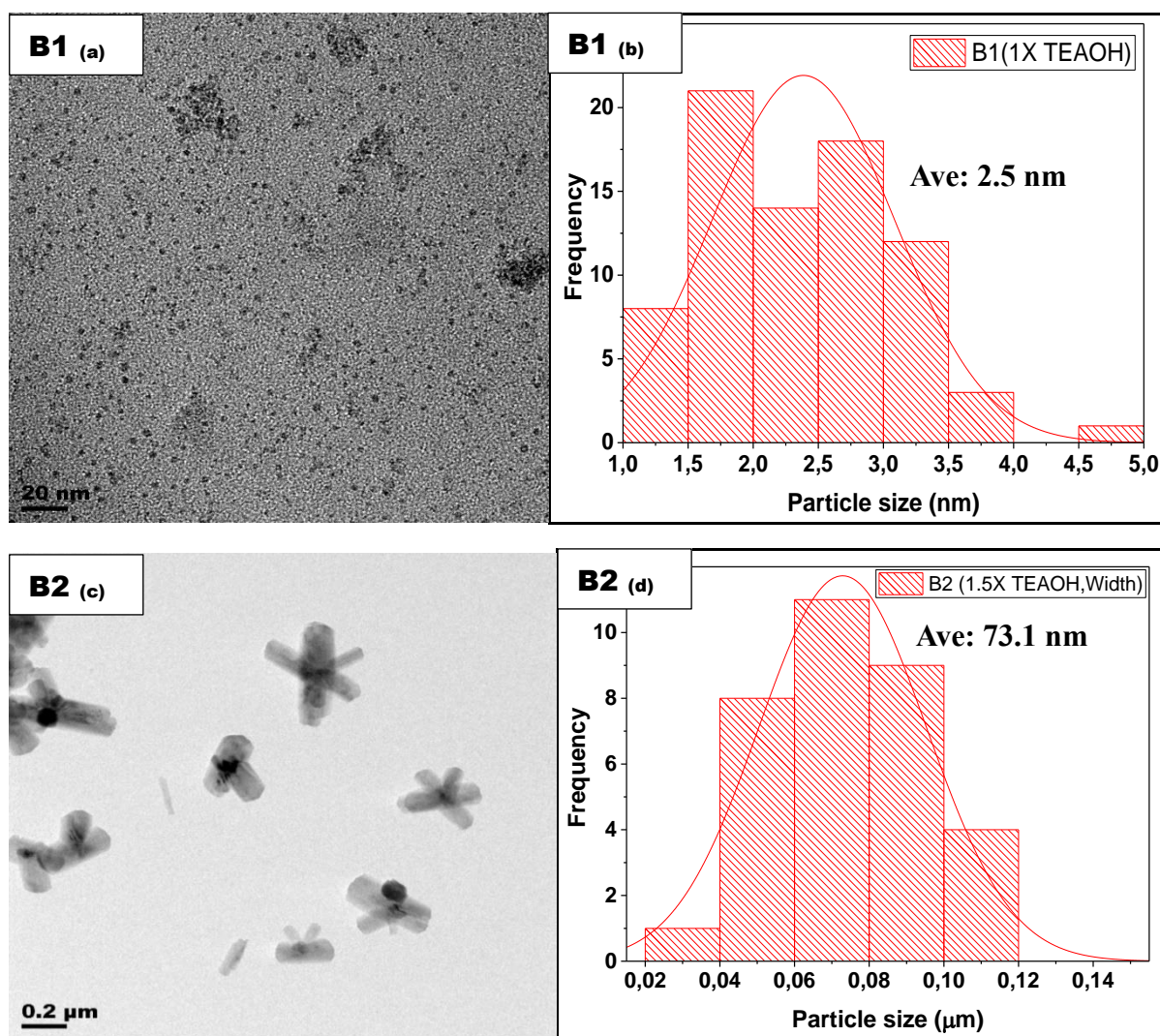


Figure 4.7: TEM images and histogram of iron oxide nanoparticles prepared ammine amounts of TMAOH: T1 (a, b) 0.06 mol, T2 (c, d) 0.09 mol and T3 (e, f) 0.12 mol



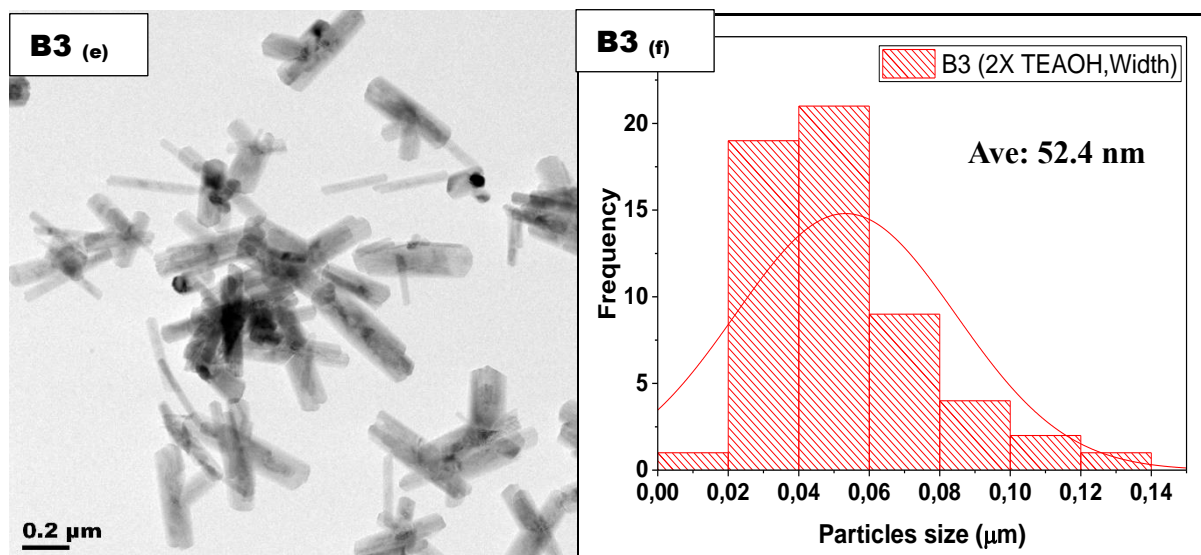


Figure 4.8: TEM images and histogram of iron oxide nanoparticles prepared at ammine amounts of TEAOH: B1 (a, b) 0.06 mol, B2 (c, d) 0.09 mol and B3 (e, f) 0.12 mol

4.2.3 FTIR ANALYSIS

The FTIR analysis was done to determine the quality of a sample and concluded the functional groups present. Dahon *et al.* (2018) concluded that the position and the widening of the IR absorption bands depends on the size and shape of the synthesised particles. **Figure 4.9:(a) and (b)** shows FTIR spectrums of the iron oxide nanoparticles synthesised using different amounts of the precipitating agents TMAOH and TEAOH. The spectrums in **Figure 4.9:(a) and (b)** shows little shift in vibrational peaks as the base amounts changes from 1 to 2X stiochiometric amount. The presence of hydroxyl stretching(O-H) peaks at 3700 cm^{-1} , terminal primary amine group (C-N) at $2260\text{--}2210\text{ cm}^{-1}$ stretching vibration and alkane (C-H) peaks at $1450\text{--}780\text{ cm}^{-1}$ are attributed to the precipitating base TMAOH and TEAOH.

Figure 4.9(a) shows the sharp absorption peak at $3500\text{--}3300\text{ cm}^{-1}$ which is attributed to stretching vibration band N-H vibration peaks,confirming that TMAOH precipitating agent also acted as capping agent during synthesis of nanoparticles and similar trend is also observed in **Figure 4.9(b)** with the O-H vibration band at $3200\text{--}3100\text{ cm}^{-1}$ for TEAOH base. Absorption bands at around $580\text{--}570\text{ cm}^{-1}$ corresponding to the Fe-O vibration observed in both **Figure 4.9(a) and (b)**, which is related to iron bonding with oxygen with a small shoulder peak at 580 cm^{-1} (weak) at 1.5 X stoichiometric amount. The shape of the iron oxide nanoparticles affectedthe position and widening of the IR peaks as indicated by Dahon *et al.*, (2018).

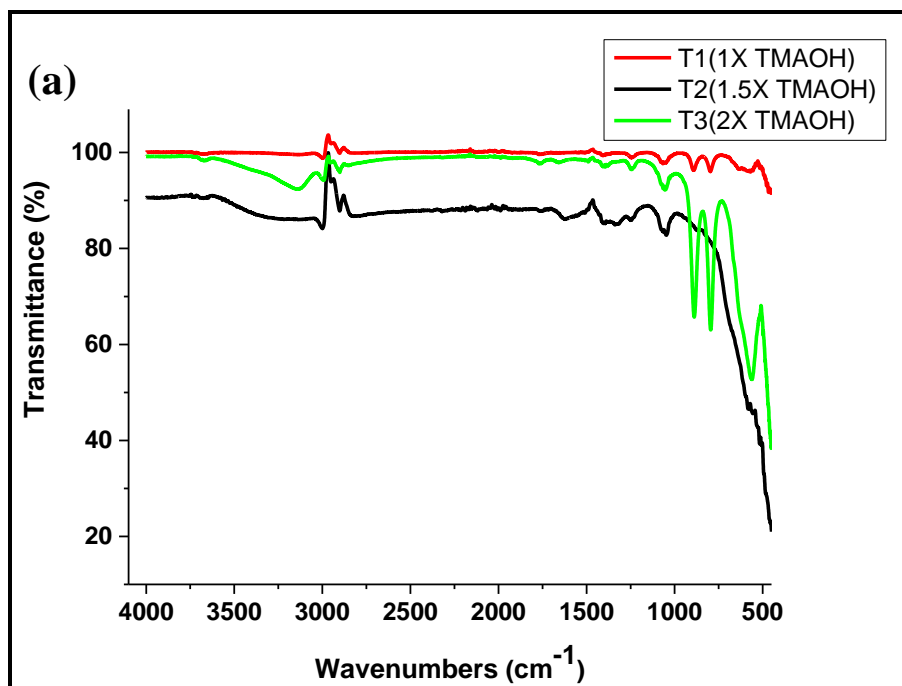


Figure 4.9: (a) FTIR spectrum of iron oxide nanoparticles prepared with TMAOH amine at T1 0.06 mol, T2 0.09 mol and T3 0.12 mol

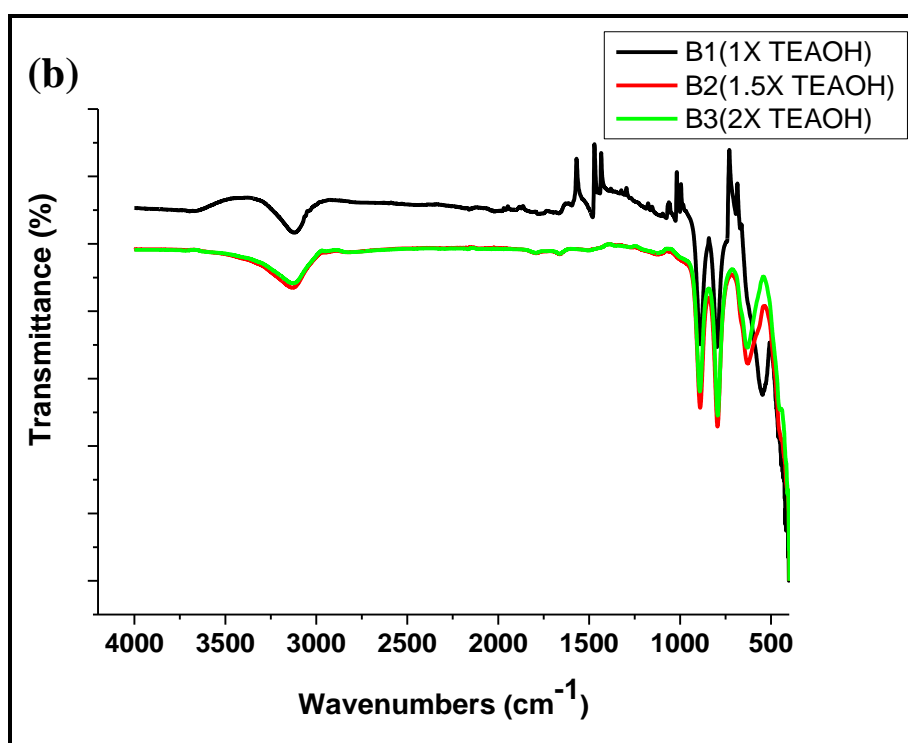


Figure 4.9: (b) FTIR spectrum of iron oxide nanoparticles prepared with TEAOH amine at B1 0.06 mol, B2 0.09 mol and B3 0.12 mol

4.2.4 UV-VIS AND PL RESULTS

Figure 4.10 (a) and (b) shows the absorption spectra of iron oxide nanoparticles synthesised at 1.0 X, 1.5X and 2X the stoichiometric amounts for TMAOH and TEAOH, respectively. Three electronic transitions have been reported for goethite (FeOOH), which are O(2p) \rightarrow Fe(3d) charge transfer and ligand field (Fe d \rightarrow d) transitions and interactions between magnetically coupled Fe(III) ions. The peak around 250 nm is due to the charge transfer. The d-d electron transitions are at higher wavelengths. Goethite is mostly direct band gap material but also contains significant amounts of indirect band gap structure due to the atomic structure distortion that is present in nano-crystallites (Zhang *et al.*, 2011). Therefore, both direct and indirect band gaps were determined with Tauc plots as shown in (**Appendixes A: Figure 4.11.1: (a-f) and Figure 14.11.2: (a-f)**). A red shift (T1-T3) was observed for TMAOH with direct band gaps from 1.91-2.46 eV. Red shift band gaps of 2.40, 2.46 and 2.55 eV for B1, B2 and with a blue shift in sample B3 respectively was observed from the direct Tauc plots for TEAOH relative the bulk band gap of 2.50 eV of Goethite (FeOOH) (Zhang *et al.*, 2011). The indirect Tauc plots obtained for the samples prepared using both TMAOH and TEAOH also shows smaller band gaps due to the atomic structure distortion that is present in nano-crystallites as confirmed by (Zhang *et al.*, 2011).

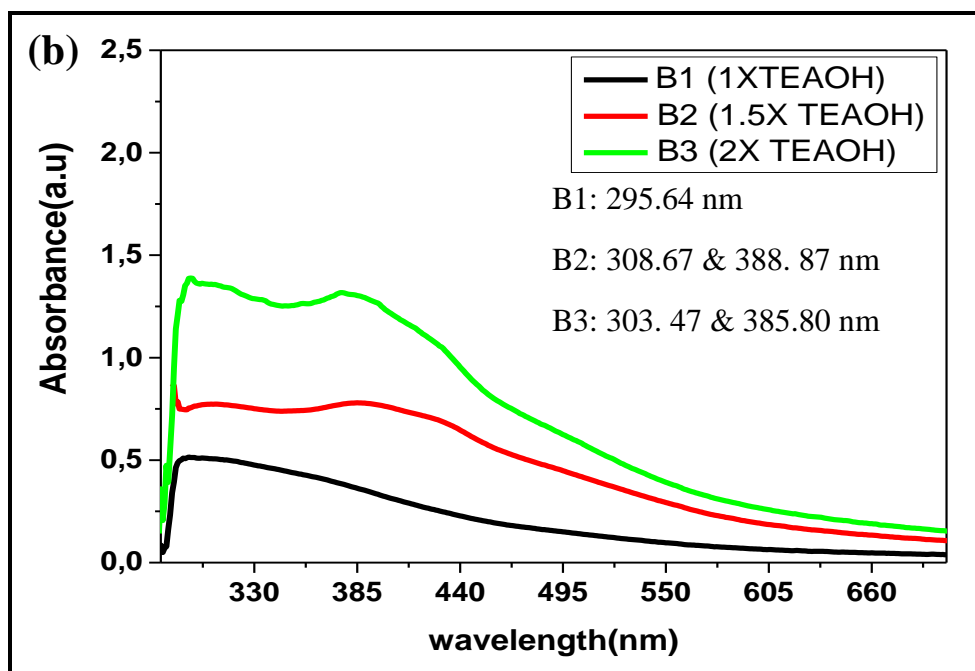
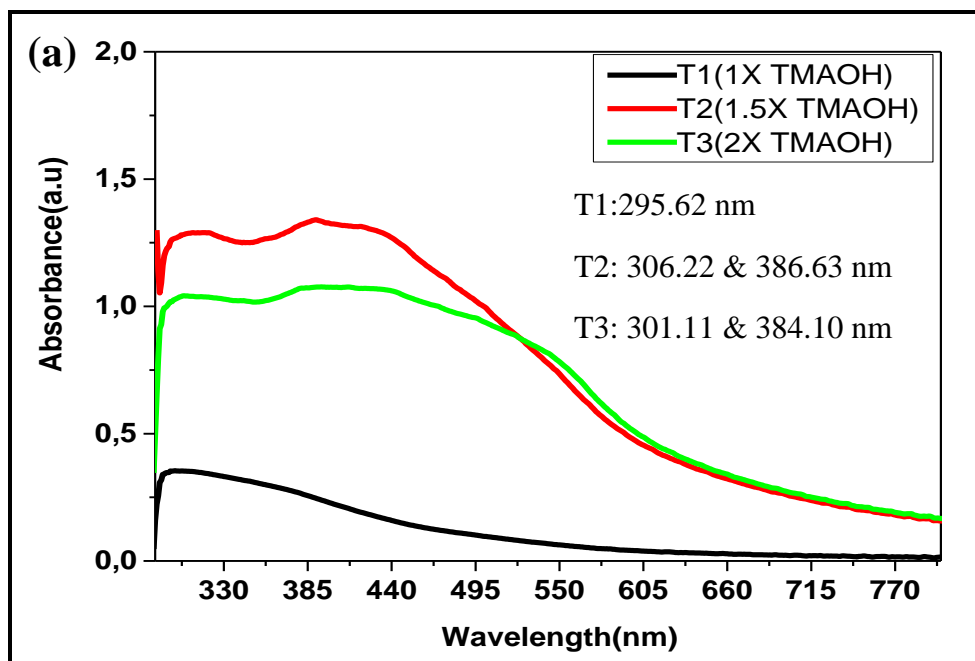
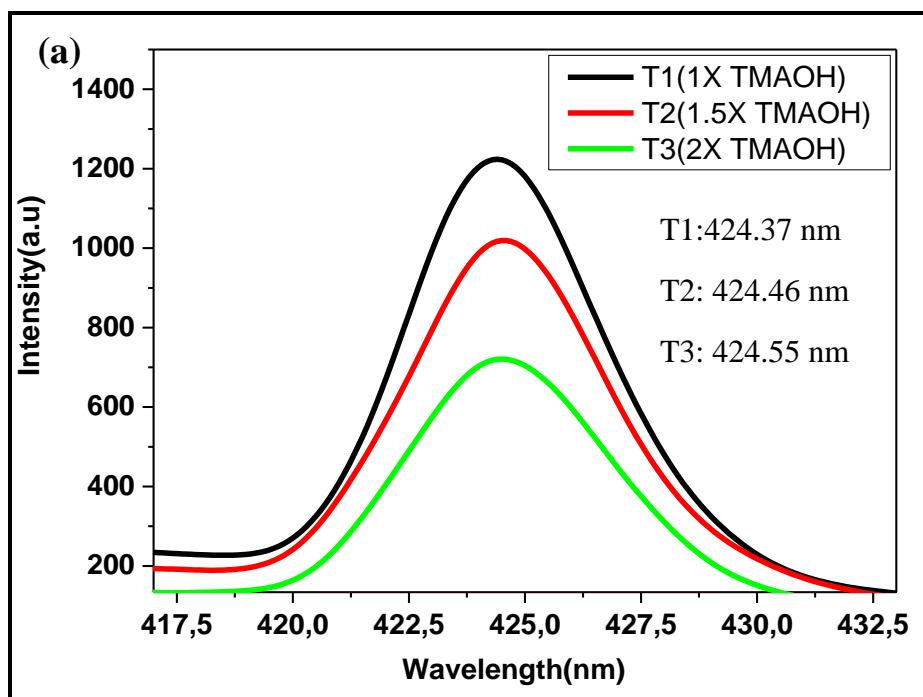


Figure 4.10: Absorption of iron oxide nanoparticles synthesised with amine TMAOH **(a)** at amounts of T1: 0.06, T2: 0.09, T3: 0.12 mol, B1: 0.06, B2: 0.09 and B3: 0.12 mol for TEAOH **(b)**

Figures 4.12 (a) and (b) shows emission spectra of iron oxide nanoparticles synthesised at 1.0, 1.5 and 2 times the stoichiometric amount of TMAOH and TEAOH. Both precipitating agents show a strong emission peaks in the visible region from 424 nm to 459 nm for TMAOH and TEAOH at different amount of base, similar strong emission peak was reported by Manikandan *et al.* (2014) at 341 nm, which was due to the presence of defects and oxygen. The emission peaks from 424.37-459.26 nm showed a typical red shift from their absorption peaks as indicated by their UV-Vis analysis in **Figure 4.12 (a and b)** . Both **Figures 4.12 (a) and (b)** show a slight shift from the lower wavelength to the higher wavelength as the base amount is increased from 0.06 mol to 0.12 mol. As the amount of ammine was increased, there was a slight change of the peak intensities, which this could be due to the change in morphology as confirmed by TEM image in **Figure 4.7 and 4.8**. The observed shift is small; therefore, one may assume that emission wavelength may be independent of the particle's sizes.



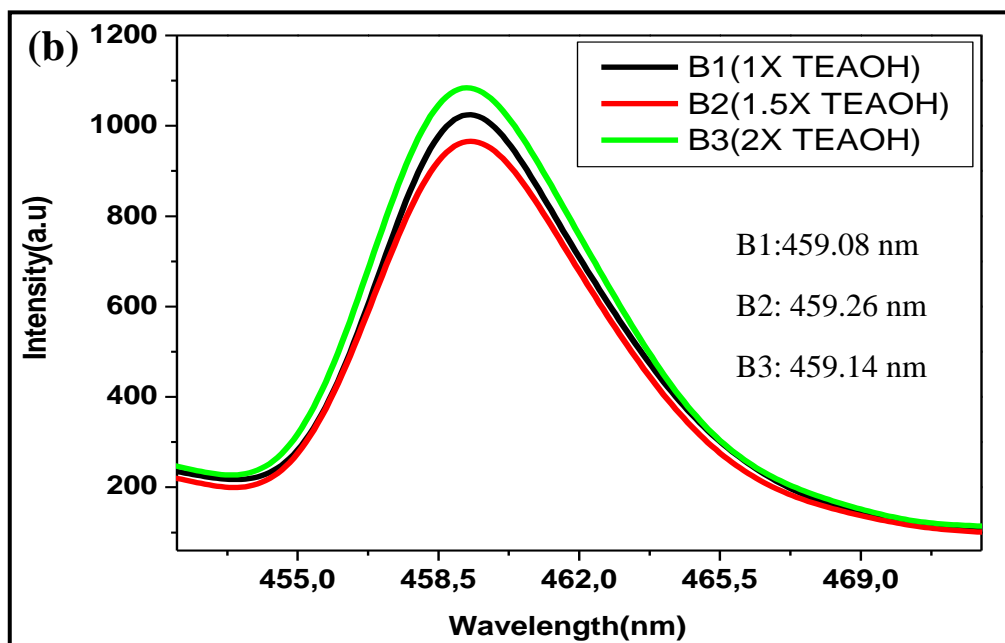


Figure 4.12: Emission spectrum of iron oxide nanoparticles synthesised with amine TMAOH (a) at amounts of T1: 0.06, T2: 0.09, T3: 0.12 mol, B1: 0.06, B2: 0.09 and B3: 0.12 mol for TEAOH (b)

In conclusion, the method of precipitation and oxidation at stoichiometric amount of ammine, 1.5 times and 2.0 times the stoichiometric amounts required to form $\text{Fe}(\text{OH})_3$ allowed the formation of nanoparticles with different shapes and sizes by analysing the TEM images. It was observed that particles significantly changed in the morphological structures due to an increase in the basic amine solution during reaction thus also affected the size of the obtained nanoparticles (**Figure 4.6 and 4.7**) and showing XRD calculated sizes smaller than sizes obtained from TEM images. Goethite (FeOOH) with orthorhombic phase shows dominance in the XRD analysis of samples at both precipitating agents. UV-Vis spectra comparison concludes similar composition in both TMAOH and TEAOH amine. FTIR spectra confirms that presence of functional groups of the precipitating agent, therefore it can be assumed that the precipitating agent also acted as a capping agent during synthesis. The emission spectra in was in agreement with other characterisations.

4.3 EFFECT OF THE TYPE OF PRECIPITATING AGENT

Here the iron (II) chloride was precipitated with the stoichiometric amount of different precipitating agents $(\text{CH}_3)_4\text{N-OH}$, $(\text{CH}_3\text{CH}_2)_4\text{N-OH}$, NaOH and $\text{C}_2\text{H}_7\text{N}$ as outlined in **Table 3.3**

4.3.1 XRD ANALYSIS

The XRD results of the nanoparticles samples prepared by different precipitating agents are shown in **Figure 4.13** below. The characteristics of all the 2θ angles samples obtained correspond very well

with the standard sample of magnetite/maghemite with card no: [JCPDS 00-019-0629] / [JCPDS 00-025-1402], proving that the samples could be identified as Fe_3O_4 / $\gamma\text{-Fe}_2\text{O}_3$ with a spinel structure. The broadness of the reflection peaks and their intensities changed slightly along with the change in the precipitating agent. The broadening of the XRD peaks could be attributed to the small crystallite size and poor crystallinity. Based on the Scherrer equation from half-width of the XRD main peak at (311), the average crystallite sizes were estimated to be 4.5, 4.1, 4.8 and 4.7 nm respectively for MA1-MA4 (**Table 4.3**). According to the calculated average sizes of the nanoparticles, all the precipitating agents used to synthesise the samples prove to be great precipitating agents as they give small particles sizes of less 5 nm of Fe_3O_4 / $\gamma\text{-Fe}_2\text{O}_3$. The precipitation agent did not have a significant effect on the crystallite size. No other phases were observed for this method, which gives the advantage of having many options when choosing a precipitating agent for the synthesis of pure Fe_3O_4 / $\gamma\text{-Fe}_2\text{O}_3$ with small average sizes.

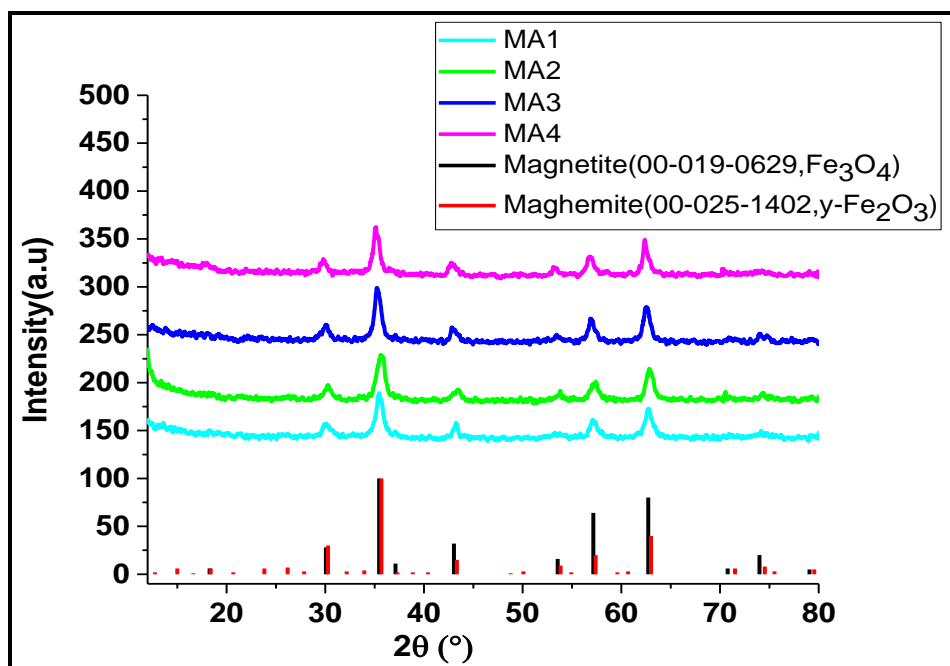


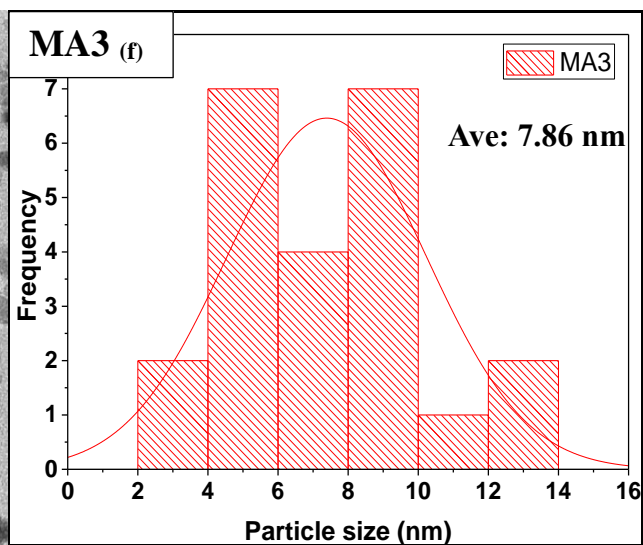
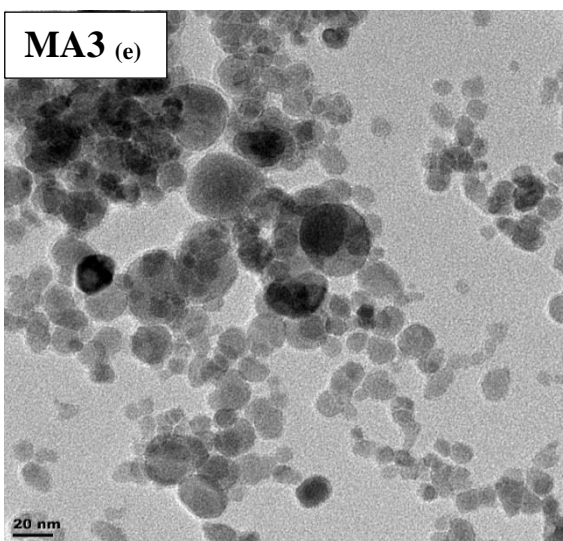
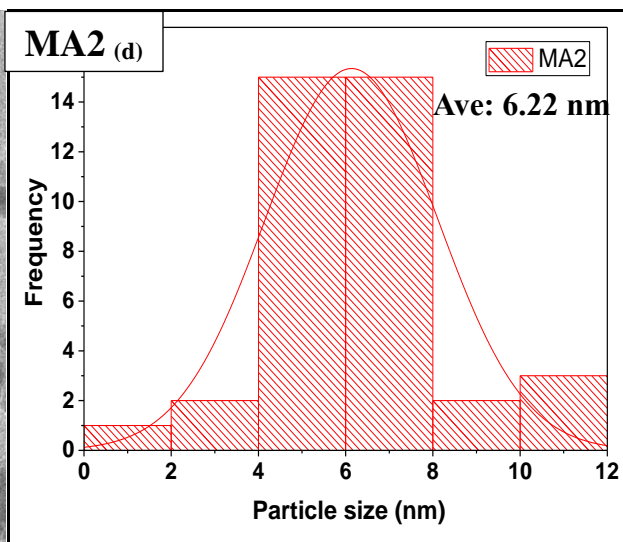
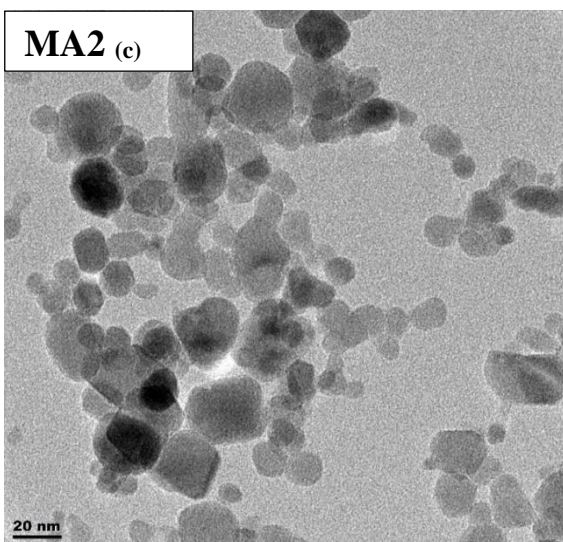
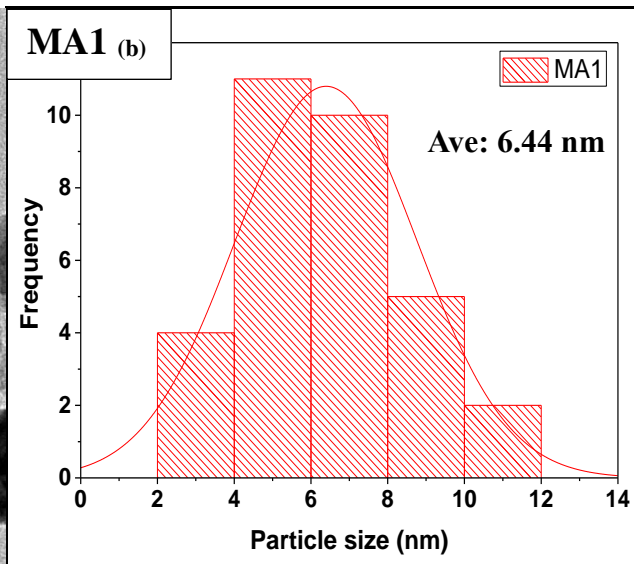
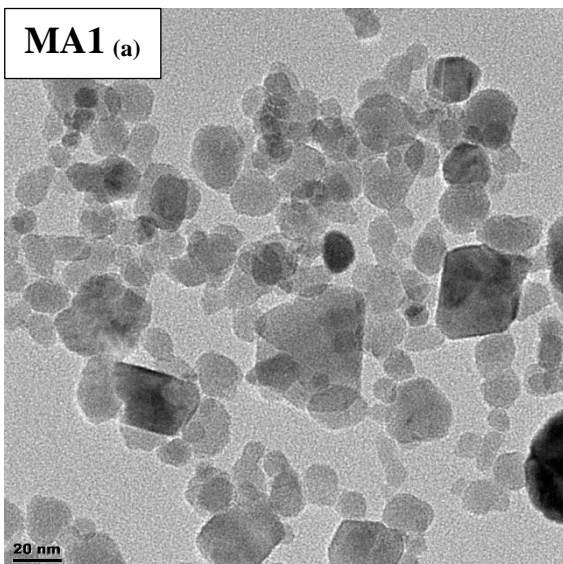
Figure 4.13: XRD diffractograms of iron oxide nanoparticles synthesised using different precipitating agents with MA1: $(\text{CH}_3)_4\text{N-OH}$, MA2: $(\text{CH}_3\text{CH}_2)_4\text{N-OH}$, MA3: NaOH and MA4: $\text{C}_2\text{H}_7\text{N}$

Table 4.3: Calculated crystallite sizes calculation XRD

Sample name	Angle (2 θ °)	Average size (nm)
MA1	35.57	4.5 nm
MA2	35.71	4.1 nm
MA3	35.41	4.8 nm
MA4	35.26	4.7 nm

4.3.2 TEM ANALYSIS

The TEM images in **Figure 4.14** show Fe₃O₄ / γ -Fe₂O₃ nanoparticles prepared using different precipitating agent bases. The morphologies of nanoparticles prepared were all nearly spherical in shape. Interestingly, nanoparticles obtained with different base (precipitating agent) have different particle sizes. The average particle sizes of the nanoparticles seem to be slightly decreasing with an increase in alkyl groups in the type of base. Mascolo, Pei & Ring. (2013) also reported that the number of aliphatic chains in a base has an effect in the particle sizes of the Fe₃O₄ nanoparticle. Furthermore, it was shows that (CH₃CH₂)₄N-OH base resulted in small particle size of 6.5 nm as compared to 10.2 nm, 7.1 nm for NaOH and KOH base respectively. The same assumption can be made from the TEM analysis obtained for this method, where MA2: (CH₃CH₂)₄N-OH shows to have smaller average particle size of 6.22 nm followed by MA1: (CH₃)₄N-OH (6.44 nm), M4: C₂H₇N (7.39 nm) and M3: NaOH (7.86 nm). The decrease in nanoparticle sizes in alkyl chain ions containing basic solution results from the steric hindrance formed by a positively-charged ions around each magnetite particle, raising the energy required for the particles to agglomerate forming large particles (Mascolo, Pei & Ring, 2013). The TEM image in **Figure 4.13** shows that sizes calculated are larger than the sizes obtained from XRD, however, it is expected that the larger mean size of the particles in the case of TEM samples are due to higher tendency of particles in sample to aggregate where two particles may appear to be one. The smaller XRD sizes may also arise from imperfections like strain and dislocations in the crystal structure, leading to a broad diffraction peak. The Scherrer equation, which was used to calculate the XRD crystallite sizes, assumes that the peak broadness is only due to size effects.



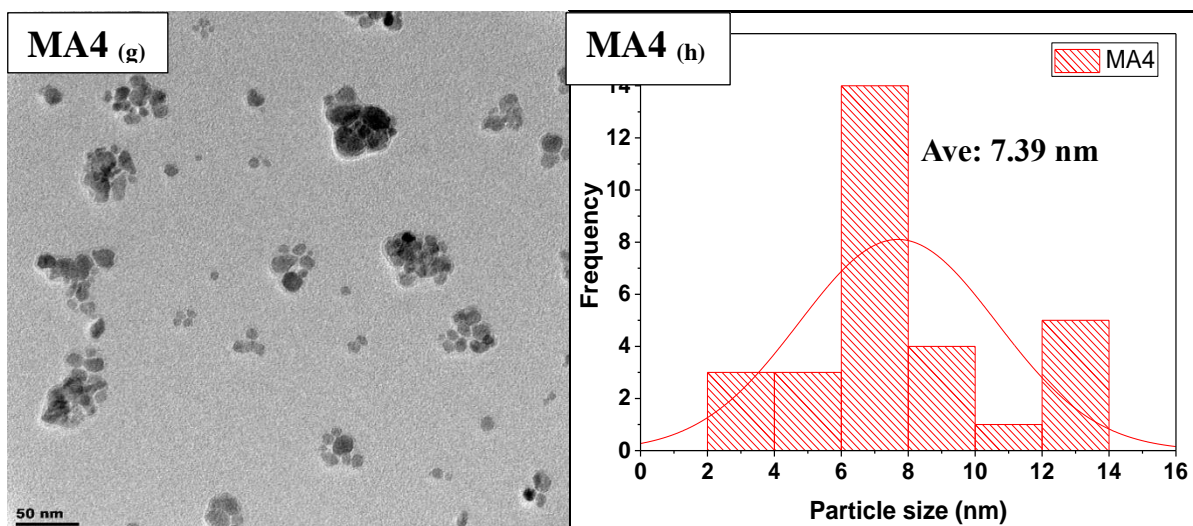


Figure 4.14: TEM images and histogram of iron oxide nanoparticles prepared by MA1 (a, b): $(\text{CH}_3)_4\text{N-OH}$, MA2 (c, d): $(\text{CH}_3\text{CH}_2)_4\text{N-OH}$, MA3 (e, f): NaOH and MA4 (g, h): $\text{C}_2\text{H}_7\text{N}$ precipitating agents

4.3.3 FTIR ANALYSIS

The FTIR spectra of Fe_3O_4 nanoparticles **Figure 4.15** prepared using different precipitating agent base in **Figure 4.15** show the presence of trace amounts of the functional groups characteristics of the precipitating agents used. The main peaks due to base consists of a broad peak observed at 3348.80 cm^{-1} attributed to the O-H stretching vibration of organic hydroxyl group containing compounds, namely $(\text{CH}_3)_4\text{N-OH}$, $(\text{CH}_3\text{CH}_2)_4\text{N-OH}$, NaOH as well as H_2O in $\text{C}_2\text{H}_7\text{N}$ from the washing process. The band at 1580.11 cm^{-1} indicates symmetric C-C bending from the amine group in MA1, MA2 and MA4 samples. The FTIR magnetite's/maghemite FTIR spectrum also reveals functional group characteristic of Fe-O stretch showing a strong peak at 569 cm^{-1} and a weak small shoulder peak at 475 cm^{-1} . The observed peaks matched the findings of the study by Dahon *et al.* (2018).

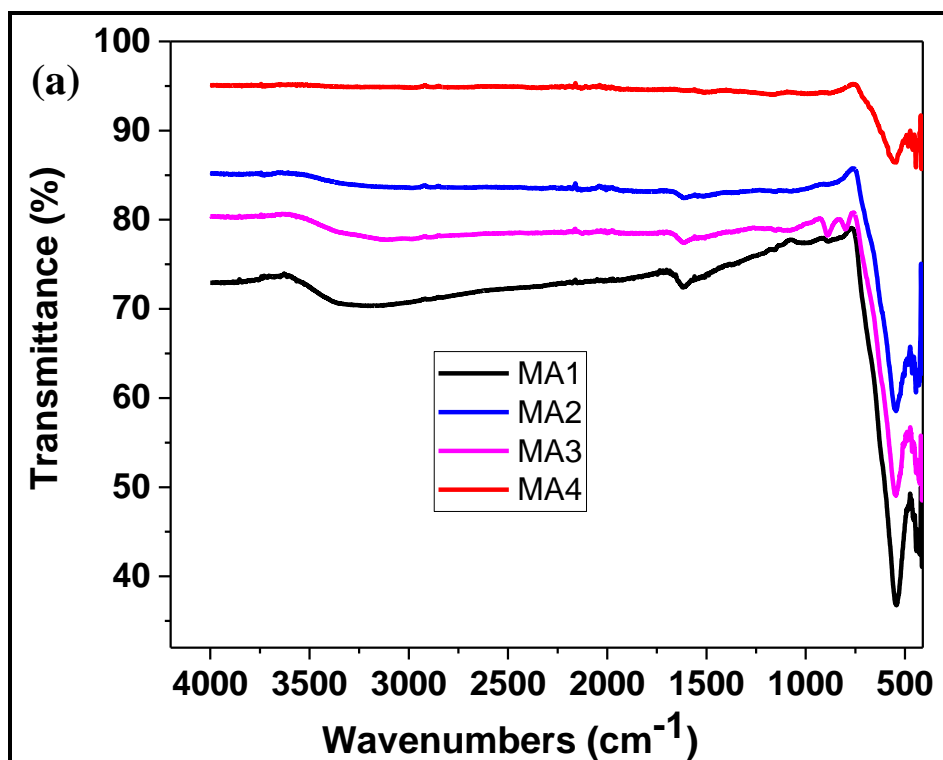


Figure 4.15: FTIR spectrum of iron oxide nanoparticles prepared with different precipitating agents MA1: $(\text{CH}_3)_4\text{N-OH}$, MA2: $(\text{CH}_3\text{CH}_2)_4\text{N-OH}$, MA3: NaOH and MA4: $\text{C}_2\text{H}_7\text{N}$

4.3.4 UV/ VIS AND PL RESULTS

Figure 4.16 (a) shows the absorption spectrums for the synthesised iron oxide nanoparticles using different precipitating agents. The following band-gap values were obtained from Tauc plots in **Figure 4.16: (b)** 1.51 eV, 1.49 eV, 1.54 eV and 1.59 eV for particles using different precipitating agents ($(\text{CH}_3)_4\text{N-OH}$, $(\text{CH}_3\text{CH}_2)_4\text{N-OH}$, NaOH and $\text{C}_2\text{H}_7\text{N}$), (see **Table 3.3**) respectively, in the assumption of a direct transition allowed. Particles prepared at different precipitaing agents shows a difference in the band edges of the obtained absorption spectras. Although all the prepared samples shows a red shift as compared to 2.2 eV of the bulk Fe_3O_4 / $\gamma\text{-Fe}_2\text{O}_3$ (Saha and Bhunia, 2013; Manikandan *et al.*, 2014). **Figure 4.16 (a)** shows that MA2 has the lowest absorption band edges of 293.98 nm as compared with MA1-MA4 with band edges of 295.04, 297.31 and 299.57 nm, respectively. This is mainly due to the longest alkyl group attached to the base $(\text{CH}_3\text{CH}_2)_4\text{N-OH}$, which resulted in more steric hindrance, resulting in the smallest size obtained from XRD calculations. A larger band gap is expected for smaller particles as observed for the MA2 nanoparticles. The direct Tauc plots of the nanostructures also shows red shifted absorption as

compared to 2.2 eV (Saha and Bhunia, 2013; Manikandan *et al.*, 2014) of the bulk as seen in TEM analysis, this significant observation could be due to growth of the particles.

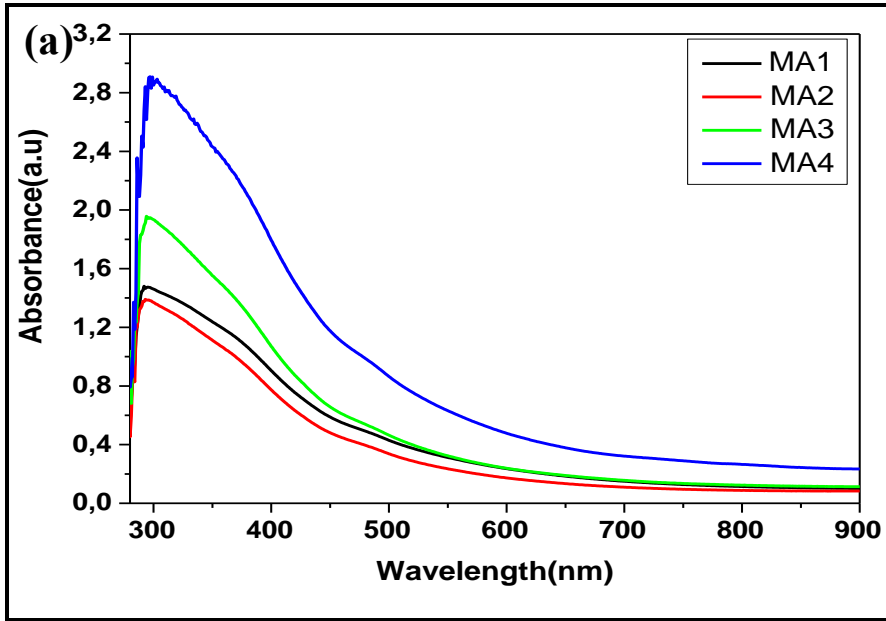


Figure 4.16: (a) absorption of iron oxide nanoparticles synthesised using different precipitating agents with MA1: $(\text{CH}_3)_4\text{N-OH}$, MA2: $(\text{CH}_3\text{CH}_2)_4\text{N-OH}$, MA3: NaOH and MA4: $\text{C}_2\text{H}_7\text{N}$

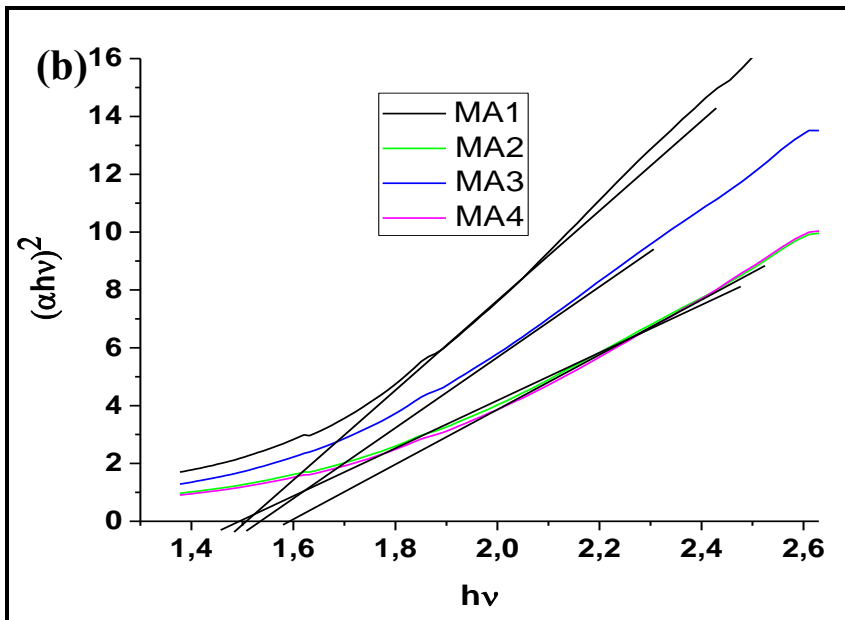


Figure 4.16: (b) Tauc plot for direct bandgap of magnetite nanoparticles. The intercept of a black lines with the horizontal axis defines the value of the bandgap at different bases with MA1: $(\text{CH}_3)_4\text{N-OH}$, MA2: $(\text{CH}_3\text{CH}_2)_4\text{N-OH}$, MA3: NaOH and MA4: $\text{C}_2\text{H}_7\text{N}$

Figure 4.17 shows the emission peaks of samples obtained using different precipitating agents. The nanoparticles were excited at the wavelength of 220 nm. It is observed that the emission wavelengths were all blue shifted relative to their absorption band edges and it also shows a slight shift from the lower wavelength of (259.8 nm) to the higher wavelength of (260.4 nm) as the precipitating agents used is changed. The emission spectrum shows that precipitating agents with longer alkyl groups exhibits lower wavelength due to a change in size of nanoparticles between MA1, MA2 and MA4. However, MA3(NaOH) shows blue shift as compared to MA4(C₂H₇N), thus with faster excitation from valence band to conduction band. The observed results in the PL analysis can also be supported by the other analysis done in this method (XRD, TEM, UV-Vis and FTIR) to conclude that the nature of the precipitating agent used had an impact in the optical response of the material.

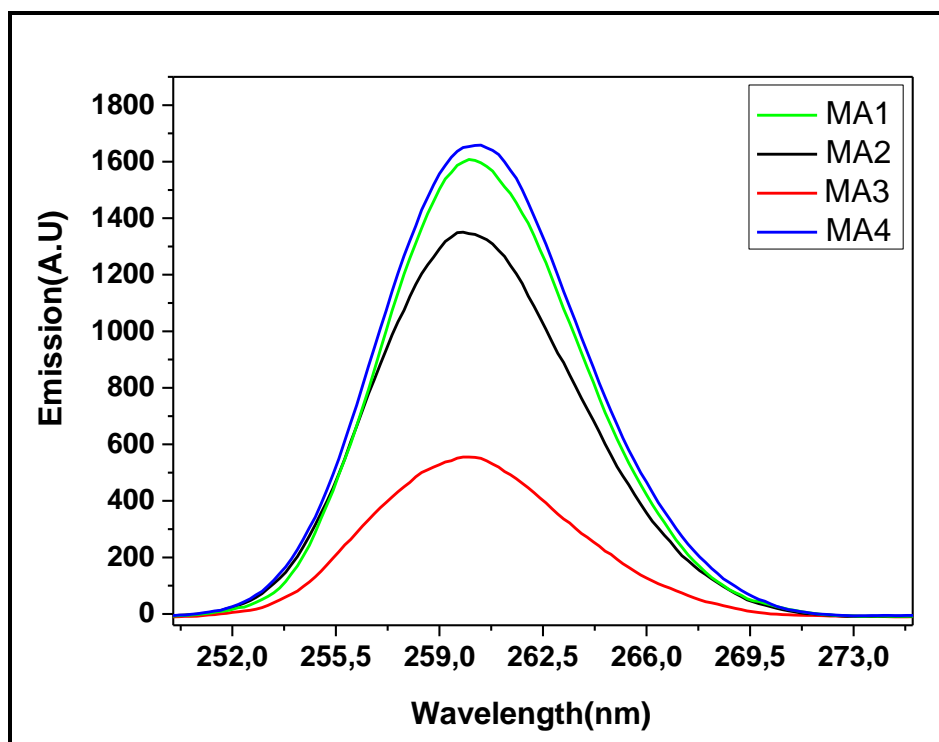


Figure 4.17: Emission spectrum of iron oxide nanoparticles synthesised with different precipitating agents MA1: (CH₃)₄N-OH, MA2: (CH₃CH₂)₄N-OH, MA3: NaOH and MA4: C₂H₇N

In conclusion, the Fe₃O₄ / γ -Fe₂O₃ nanoparticles Mixture with different particles sizes has successfully synthesised using various precipitating agents. XRD patterns shows a well define peaks, which clearly indicate greater crystallinity and imperfections like strain and dislocations in the crystal structure. The well indexed of both phases require XPS analysis for further confirmation. TEM image analysis shows that the samples exhibit a spherical morphology a smaller sizes as the number of alkyl

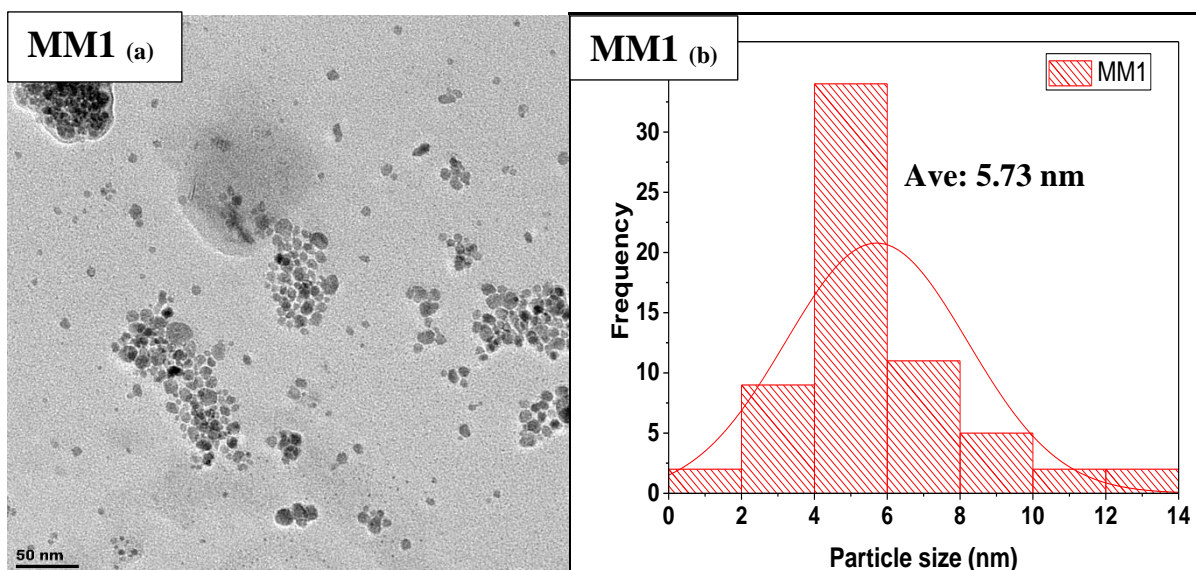
group attached to the precipitating agent. FTIR analysis shows traces of the functional groups of the used precipitating agents on the surface of the obtained samples and the optical properties were red shift in comparison with the bulk sample (i.e., UV-Vis and PL analysis) with size differences.

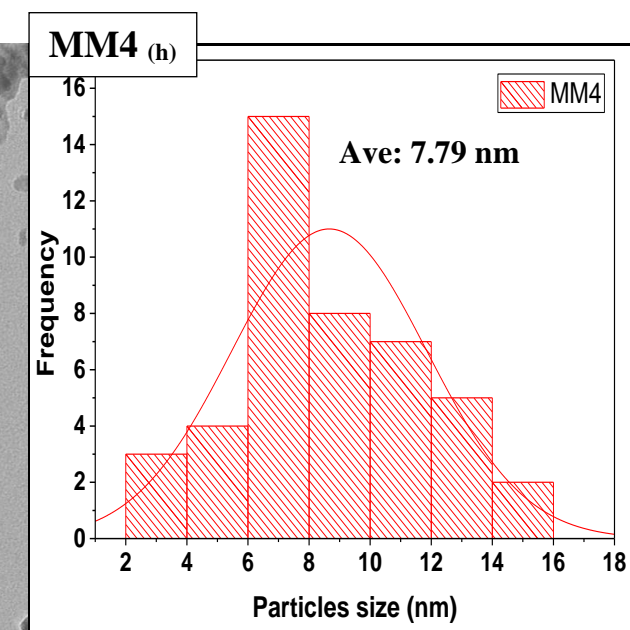
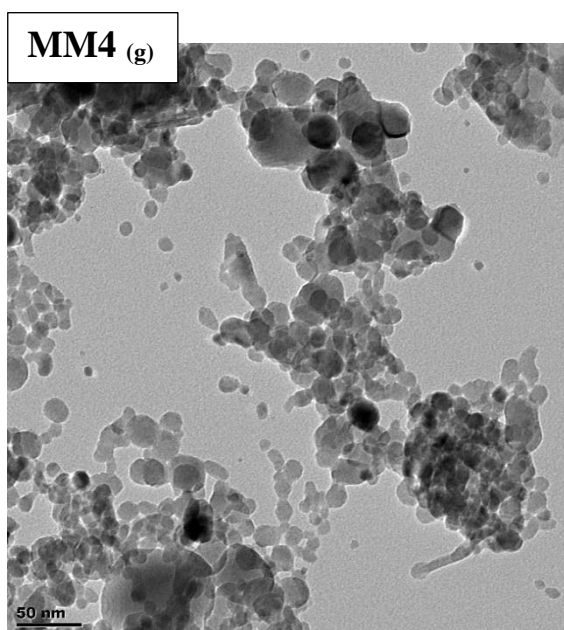
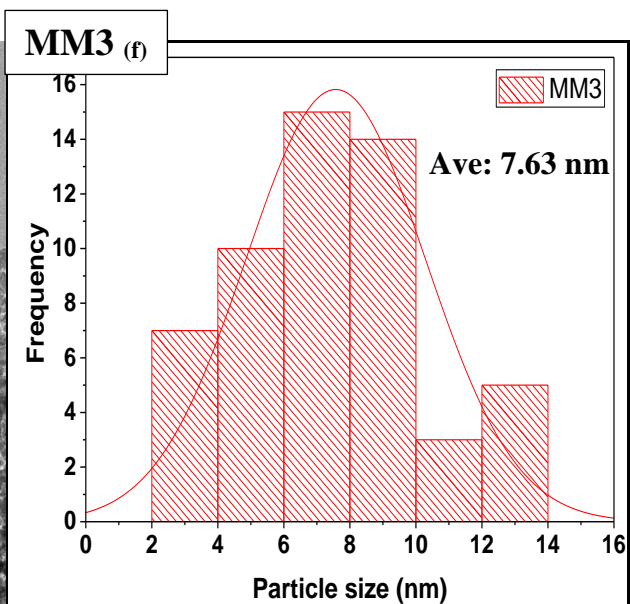
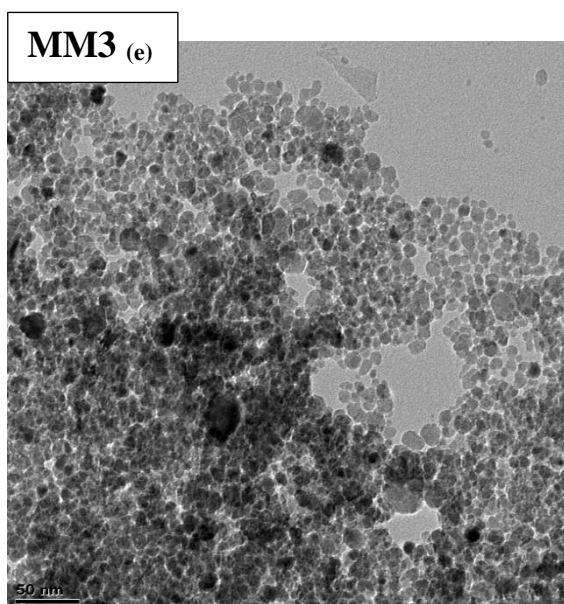
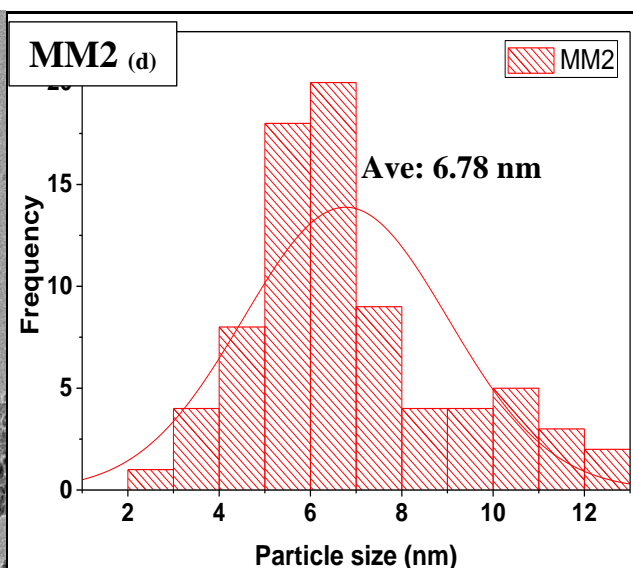
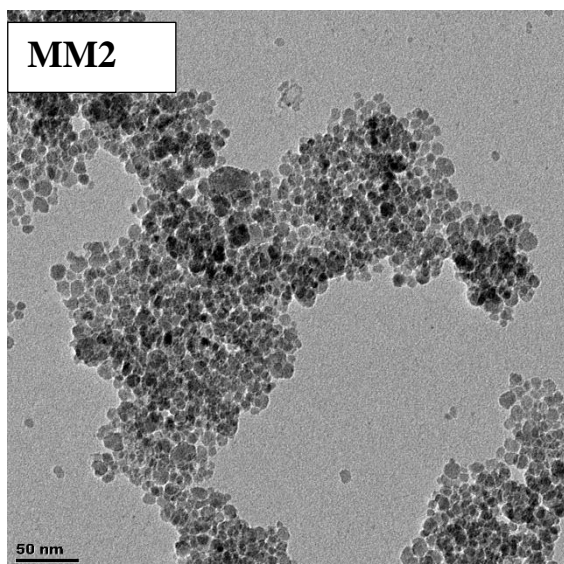
4.4. EFFECT OF TEMPERATURE USING OXIDATION-PRECIPITATION-OXIDATION METHOD.

Effect of temperature on the synthesis of iron oxide nanoparticles with tetramethyl ammonium hydroxide ((CH₃)₄N-OH)) as a precipitating agent for iron (II) chloride precursor. The influence synthesis temperature was examined at reaction time of 1 hr (**Table 3.3**) and the findings are discussed in this section. Variation in temperature performed during this experiment was to access temperature effects on the synthesis of nanoparticles in terms of size, shape and phase.

4.4.1 TEM ANALYSIS

Figure 4.18 shows the TEM images and size distribution of the iron oxide nanoparticles synthesised at temperature 25, 45, 65, 85 and 105 °C. A uniform spherical shape was observed for the iron oxide nanoparticles synthesized at all temperatures (25-105°C) with a size distribution 5.73-8.76 nm. When the reaction temperature was increased, there was no change in the particle's shape; uniform spherical nanoparticles were observed at all temperature variations. However, it was observed that as the temperature was raised from 25-105 °C, the particle sizes gradually linearly increased (**Figure 4.19**). It is evident that temperature plays an important role in the synthesis of nanoparticles, which is shown by the evolution of different sizes and aggregation of the nanoparticles as the temperature varied from 25-105 °C (Ozel, Kockar & Karaagac 2015).





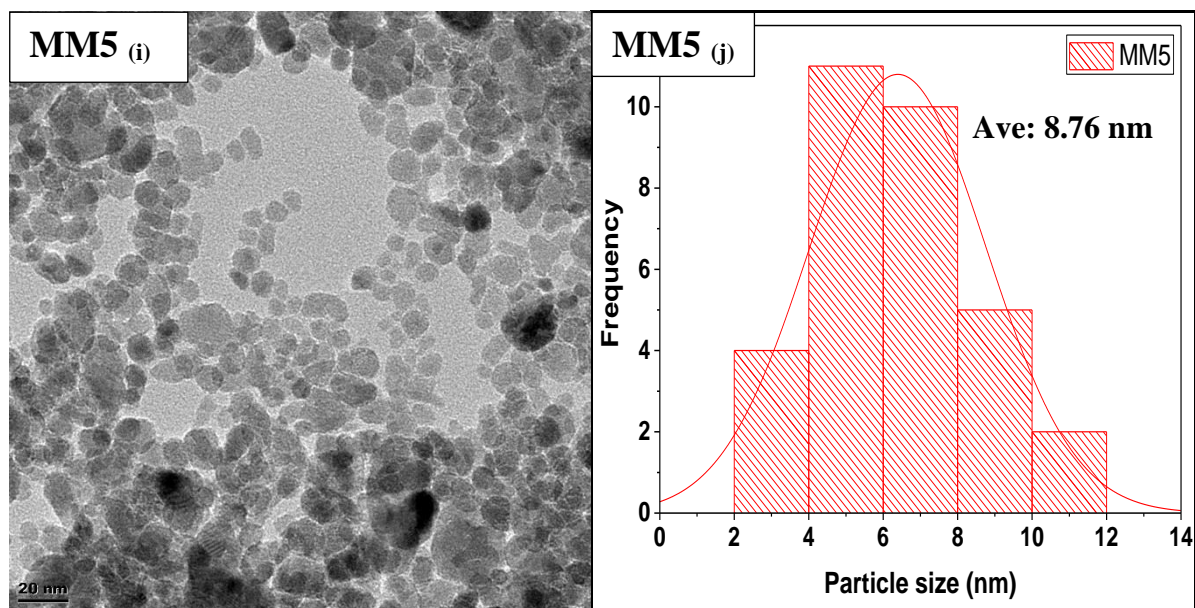


Figure 4.18: TEM images and histogram of iron oxide nanoparticles prepared at different temperature with MM1:25 °C (a, b), MM2:45 °C (c, d), MM3:65 °C (e, f), MM4: 85 °C (g, h) and MM5: 105 °C (i, j)

4.4.2 XRD ANALYSIS

The XRD patterns shown in **Figure 4.20**: (MM1), (MM2), (MM3), (MM4) and (MM5) represent Fe_3O_4 nanoparticles prepared at different temperatures (25, 45, 65, 85 and 105 °C). All the diffraction peaks can be indexed to the cubic phase of Fe_3O_4 [JCPDS, 00-019-0629] with no peaks of hematite, hydroxides and other impurities detected. The strong and sharp peaks at $2\theta = 30.1^\circ, 35.2^\circ, 43.3^\circ, 57.1^\circ$ and 63.5° shows that $\text{Fe}_3\text{O}_4 / \gamma\text{-Fe}_2\text{O}_3$ nanoparticles were of high purity and well crystalline. The average crystallite sizes of the nanoparticles were calculated using Debye Scherrer formula with the average crystallite sizes of 5.7-8.8 nm (**Table 4.4**) calculated from the full-width at maximum of $\text{Fe}_3\text{O}_4 / \gamma\text{-Fe}_2\text{O}_3$ (311) diffraction peak. A linear increase in the crystalline sizes with increased reaction temperatures was also observed (**Figure 4.19**) as the crystallites are exposed to higher temperatures for a long time similar to what was observed with TEM, resulting in easier growth of the nuclei causing an increase in the particle sizes (Mahdavi *et al.*, 2013). Moreover, the intensities of the peaks became more prominent for all the samples as the temperature of the reaction was increased from 25-105 °C, which this could be due to the increase in the particle sizes.

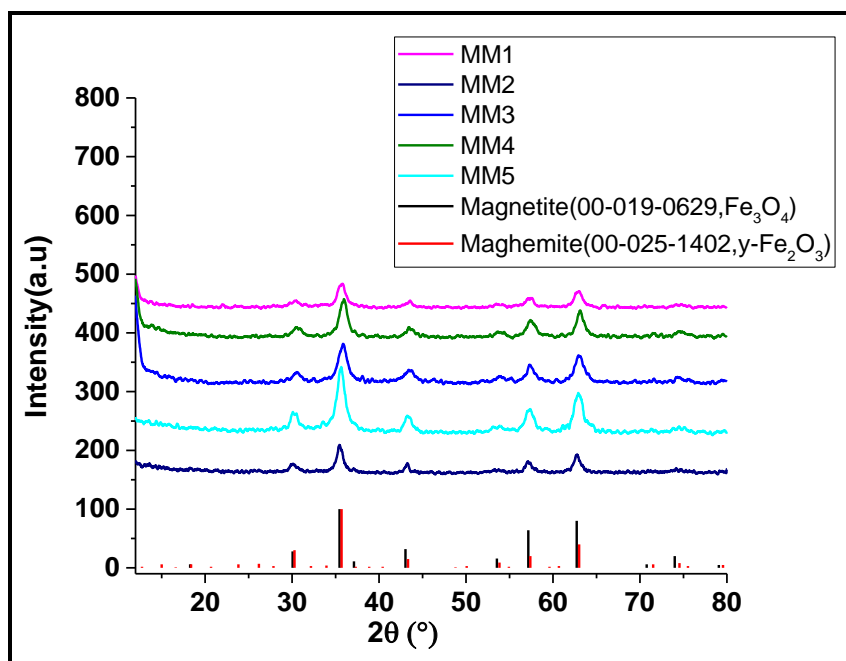


Figure 4.20: XRD patterns of iron oxide nanoparticles prepared at temperatures MM1:25 °C, MM2:45 °C, MM3:65 °C, MM4: 85 °C and MM5: 105 °C

Table 4.4: Calculated sizes calculation XRD

Sample name	Angle (2θ (°))	Average size (nm)
MM1	35.67	5.71
MM2	35.41	6.80
MM3	35.94	7.62
MM4	35.94	7.73
MM5	35.67	8.80

4.4.3 FTIR ANALYSIS

FT-IR spectra of nanoparticles heated at different temperatures are shown in **Figure 4.21. (a)** and **(b)**. The symmetric stretching of Fe-O is indicated by a band at 568-565 cm^{-1} (**Figure 4.21: (b)**). A medium sharp peak at around 3700 cm^{-1} shows an O-H stretching, which is attributed to the hydroxyl group from the precipitating base used. A smaller band assigned to the symmetrical methyl (CH_3) appears near to 1530 cm^{-1} . A single band, which appeared at 2280 cm^{-1} is attributed to the (C-N) (Andrade *et al.*, 2012). The band around 3700 cm^{-1} is due to the bulk O-H stretching. This band is said to be sensitive to the temperature of de-hydroxylation and is one of the main bands used to characterise the level of iron oxide de-hydroxylation. The increase in reaction temperature from 25-105 °C decreased the appearance of the N-H stretching ammine group, which is at around 3300-3500 cm^{-1} which suggests that precipitating agent ($(\text{CH}_3)_4\text{N-OH}$) functional groups is present on the

surface. This N-H stretching ammine group is less prominent at MM3 (45 °C) and MM5 (105 °C), thus leading to particle size increase as supported by the XRD and TEM analysis.

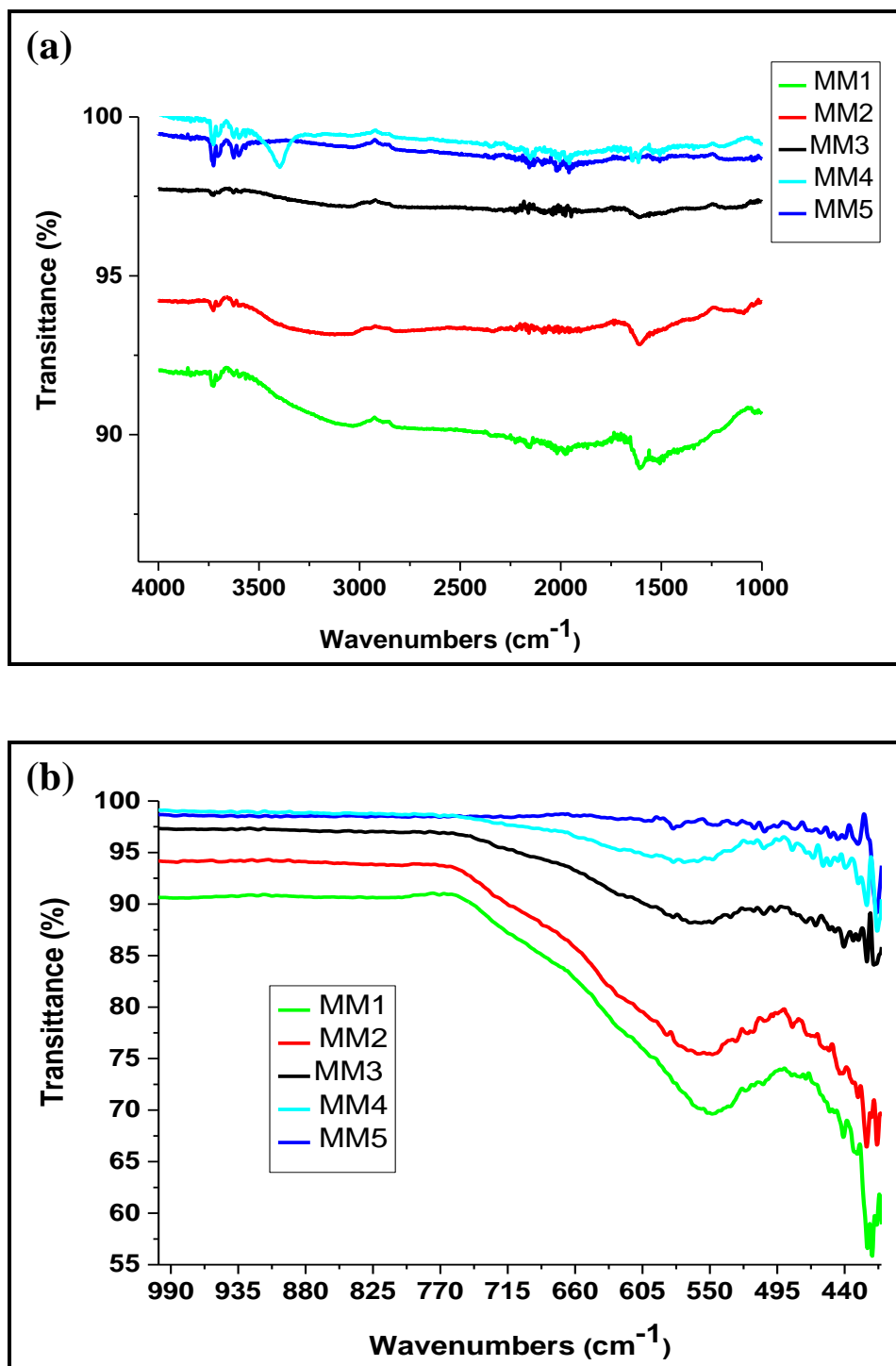


Figure 4.21: (a, b) FTIR spectrum of iron oxide nanoparticles prepared at different temperature with MM1:25 °C, MM2:45 °C, MM3:65 °C, MM4: 85 °C and MM5:105 °C

4.4.5 OPTICAL PROPERTIES

The UV-Vis absorption spectra for the prepared Fe_3O_4 nanoparticles at temperatures ranging from 25-105 °C are shown in **Figure 4.22**. Differences were noted in band edges from MM1- MM5 were the band edges increased with increasing temperature from 25-105 °C. The direct Tauc plots in Figure 9.7(a-e) of the nanostructures also shows an increase in band gaps values, which were 1.98, 2.07, 2.09, 2.11 and 2.18 eV for MM1-MM5, respectively. The values indicate that the absorption edges are red-shifted compared to 2.2 eV of the bulk Fe_3O_4 (Saha and Bhunia, 2013; Manikandan *et al.*, 2014).

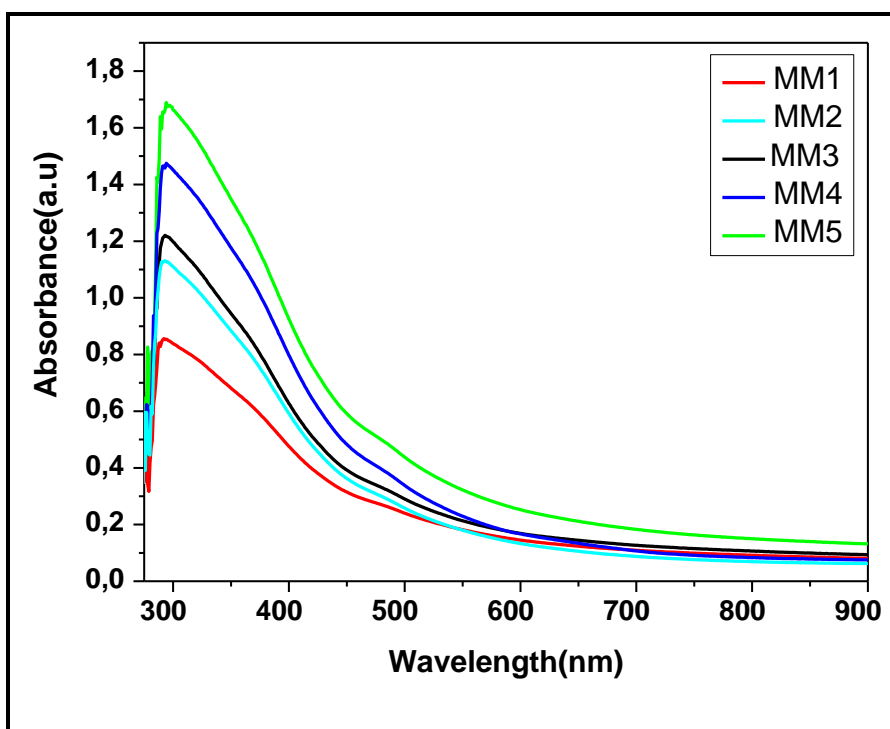


Figure 4.22: Absorption of iron oxide nanoparticles synthesised at different temperature with MM1:25 °C, MM2:45 °C, MM3:65 °C, MM4: 85 °C and MM5:105 °C

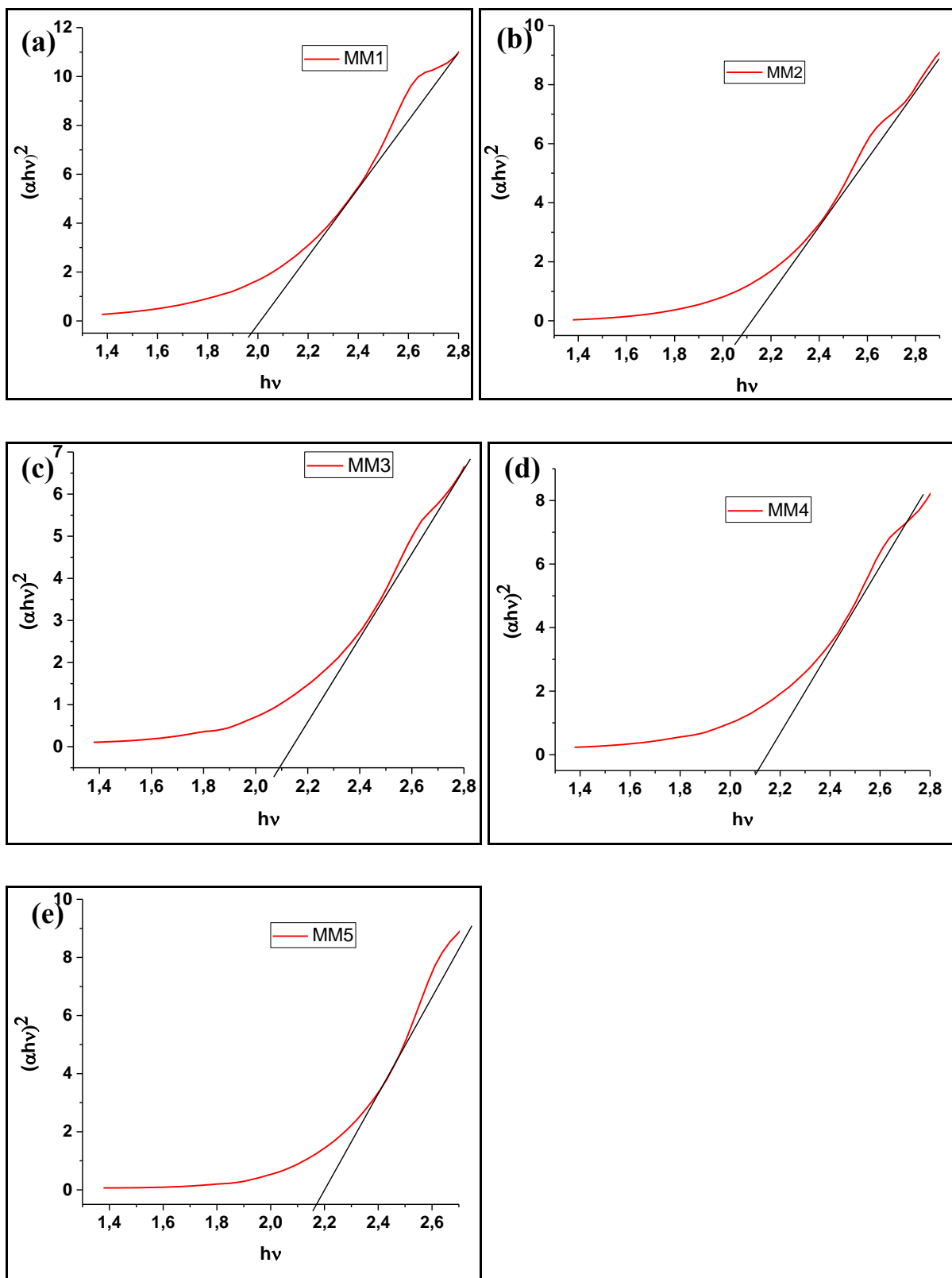


Figure 4.23: (a-e) Tauc plot for direct bandgap of magnetite nanoparticles. The intercept of a black lines with the horizontal axis defines the value of the bandgap at different temperature with MM1:25 °C, MM2:45 °C, MM3:65 °C, MM4: 85 °C and MM5:105 °C

Figure 4.26 shows the emission peaks from the nanoparticles prepared at different temperatures. The nanoparticles were excited at the smallest wavelength of 289 nm as obtained in the UV-Vis absorption bands for sample MM1-MM5. It is observed that the emission wavelengths were all blue shifted in comparison to their corresponding absorption band edges. **Figure 4.26** shows a shift from the lower wavelength of (286.4 nm) to the higher wavelength of (288.1 nm) as the temperature was raised from 25-105 °C, which suggests a change in size of nanoparticles. The change in the optical properties for the prepared nanoparticles is in agreement with the structural analysis in **Figure 4.25 (a) and (b)(Appendix A)**. The shift to higher wavelength is attributed to the excitation of electrons from occupied valence bands into conduction states band as the temperature increase from 25-105 °C due to an increase in the band gaps. Comparable results were obtained by Vidyasagar *et al.*, (2012), which shows the increase annealing temperature from 400-800 °C for CuO nanoparticles, with emission peaks slightly shifting in the direction of longer wavelength, which may be attributed to the increase in particle size at an increased annealing temperatures. Therefore, one may suggest that similar explanation could be applied for the trend observed for Fe₃O₄ nanoparticles.

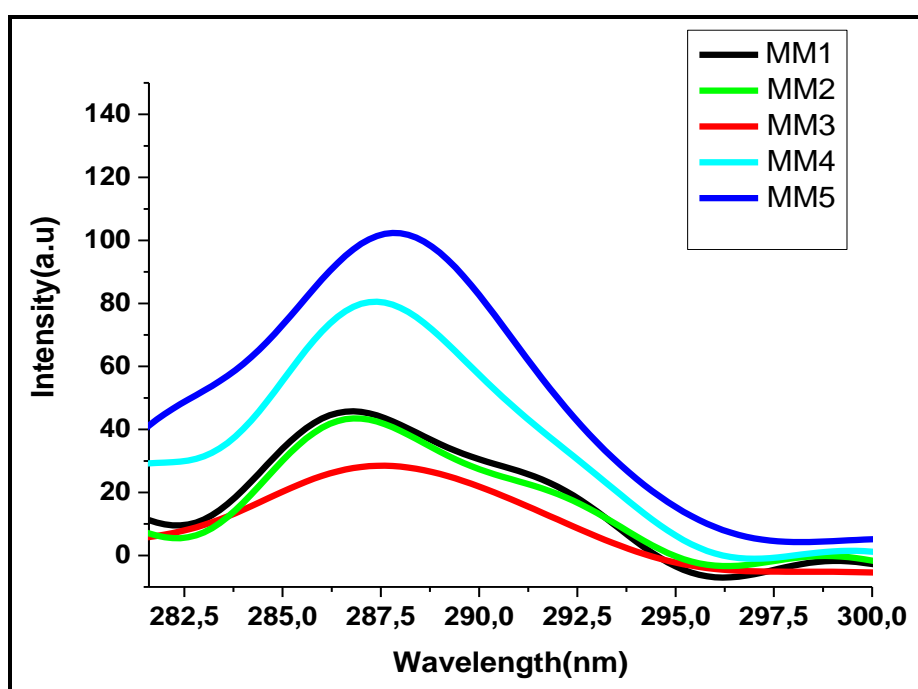


Figure 4.26: Emission spectrum of iron oxide nanoparticles synthesised at different temperature with MM1:25 °C, MM2:45 °C, MM3:65 °C, MM4: 85 °C and MM5:105 °C

In conclusion, stable $\text{Fe}_3\text{O}_4/\text{Fe}_2\text{O}_3$ nanoparticles have been synthesised by this method at different temperatures. XRD patterns depict well-defined diffraction peaks, which show that the samples are crystalline. The peaks were also easily indexed to magnetite/maghemite., TEM images show that the nanoparticles have the spherical morphology and are small-sized. The FTIR spectra show that functional groups of TMAOH precipitating agent were on the surface of the material, however, the degree of its appearances differs as the reaction temperature increased. The optical properties of the nanoparticles show a red shift in comparison with the bulk sample (i.e. UV-Vis and PL analysis) due to growth of the particles and an increased in band gaps as the temperature increase.

4.5 RESULTS AND DISCUSSION (PART 2): FENTON DEGRADATION OF MB AND KINETIC STUDIES

This section presents and discusses the Fenton kinetic results of the degradation o of MB. Selected catalysts from each method were used to identify catalysts with more catalytic efficiency in order to study further on the following in detail:

- **Performance reproducibility analysis of catalyst (M1)**
- **Re-usability of the catalyst (M1)**
- **Optimization of Fenton MB degradation reaction parameters**
 - Effect of reaction temperature of catalyst synthesis on catalytic activity
 - Effect of type precipitating agent (base) during synthesis of catalyst on catalytic activity
- **Effect of temperature on the degradation of MB**
- **Effect of H_2O_2 dosage on the degradation of MB**

4.5.1.1 Performance reproducibility analysisof catalyst (M1)

In order to check the stability and reliability of MB removal efficiency using catalyst (M1), the experiment was carried out 5 times under the same reaction conditions: 50 °C, 10 mg/L MB, 0.1000 g iron oxide catalyst and $\text{H}_2\text{O}_2 = 20$ mL, using new catalysts each time. The results in **Figure 4.27(a, b)** show that the Fenton reaction catalyst test performed repeatedly, for the production of consistent efficiency of MB of 84 % in 180 min under the same laboratory operational conditions with an R^2 of more than 0.95 for pseudo first-order reaction. Which imply that catalyst is stable and slow reactive to moisture and may be stored for a longer period and used to save costs of synthesizing new catalyst.

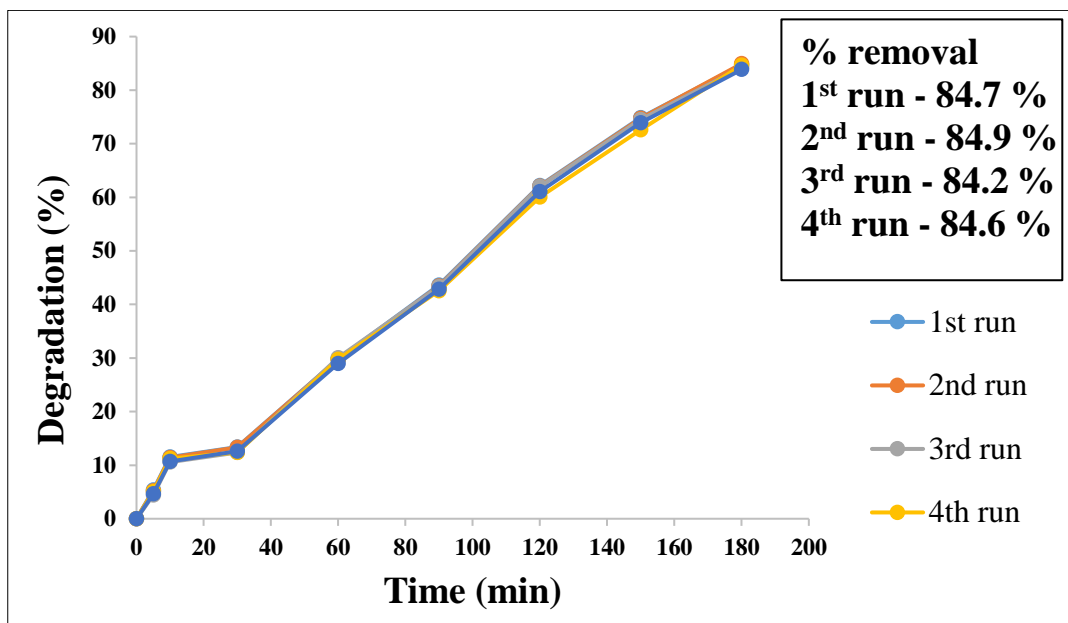


Figure 4.27(a): Performance reproducibility analysis of M1 catalyst for removal of MB in 180 min

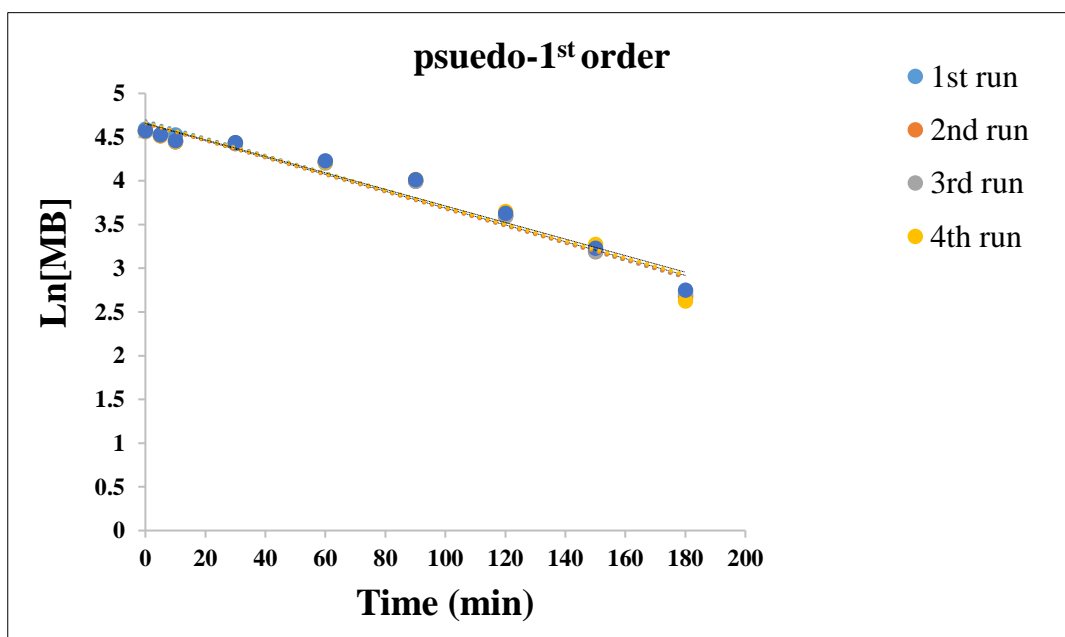


Figure 4.27: (b) pseudo 1st order performance reproducibility plot of the degradation of MB (M1) catalyst

4.5.1.2 Re-usability of the catalyst for MB degradation

To investigate the stability of catalysts used in this study, experiments were carried out under the following conditions: 50 °C, 10 mg/L MB, 0.1003 g iron oxide catalyst and $\text{H}_2\text{O}_2 = 20$ mL. The abatement in the concentration of MB was monitored. The results presented in **Figure 4.28(a)** provide insight into the stability of iron oxide catalyst for the heterogeneous Fenton-like reaction.

The % mass lost between the runs were found to be 1.60, 2.74 and 9.20 %, respectively (**Table 4.5**), which could be the cause of the drastic decrease in MB removal. The results shown in Figure 10.2(a) indicate that there was a considerable decrease in degradation efficiency from 84.7 % of the initial efficiency to 58.8 % after 3 cycles for 3 h reaction. The decrease in degradation efficiency may be attributed to loss of catalyst during filtration, washing process and small amount of catalyst dissolving in aqueous solution during the discoloration/removal of MB reaction. The iron oxide catalyst particles suspended in solution displayed high catalytic activity even after being reused three times (catalyst was used four times in total). **Figure 4.28 (b)** shows that some deactivation took place when the change in catalyst mass per re-use is taken into account by plotting the average % decolourisation per gram of catalyst. Fenton catalytic deactivation may be due to fouling and the formation surface organometallic-like compound with lower activity (poisoning) (Luca *et al.*, 2014; Lu *et al.*, 2015). Similar results are observed by Wang, Tian and Ning. (2014) where the MB removal percentage decreased from 100-99.50 % with only 1.12 % of Fc dissolving after ferrocene (Fc) was successively used for three cycles in a heterogeneous Fenton reaction. The kinetics of the reactions were determined and recorded in ((**Figure 4.29(a)** and **4.29(b)**) and **Table 4.6**, which show from the rate constants (1st order) that MB removal efficiency was declining.

Table 9.5: Measured mass at each run

Number of runs	Mass of catalyst(g/L)	Mass lost (%)
0	0.1003	0
1	0.0987	1.60 %
2	0.0960	4.29 %
3	0.0872	13.06 %

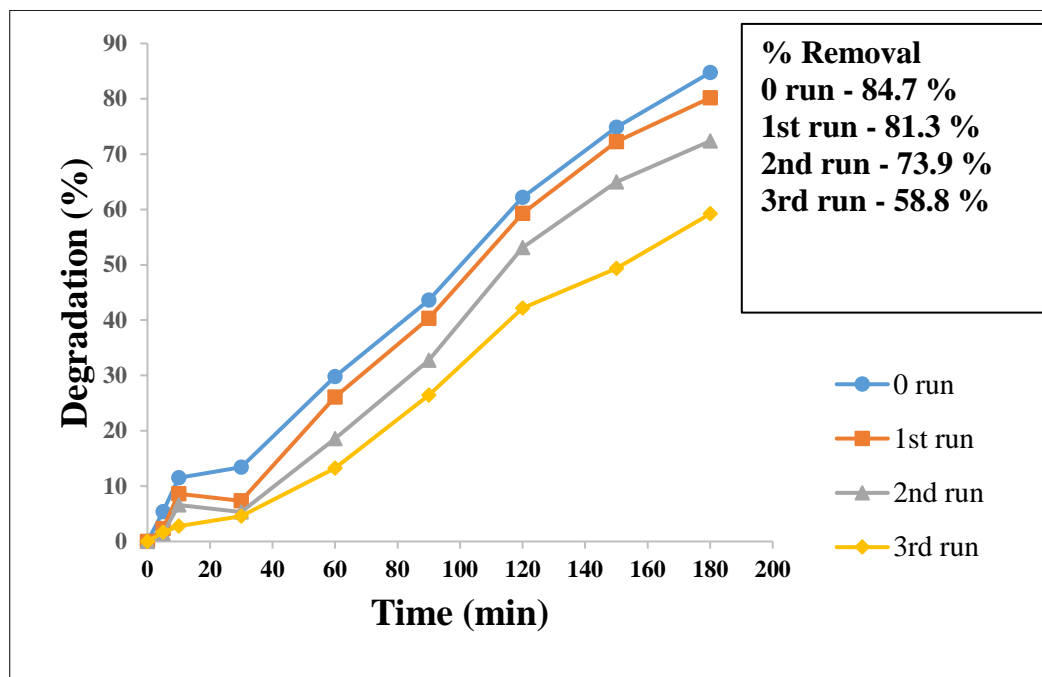


Figure 4.28: (a) effect of reusing the catalyst on degradation of MB of M1 catalyst

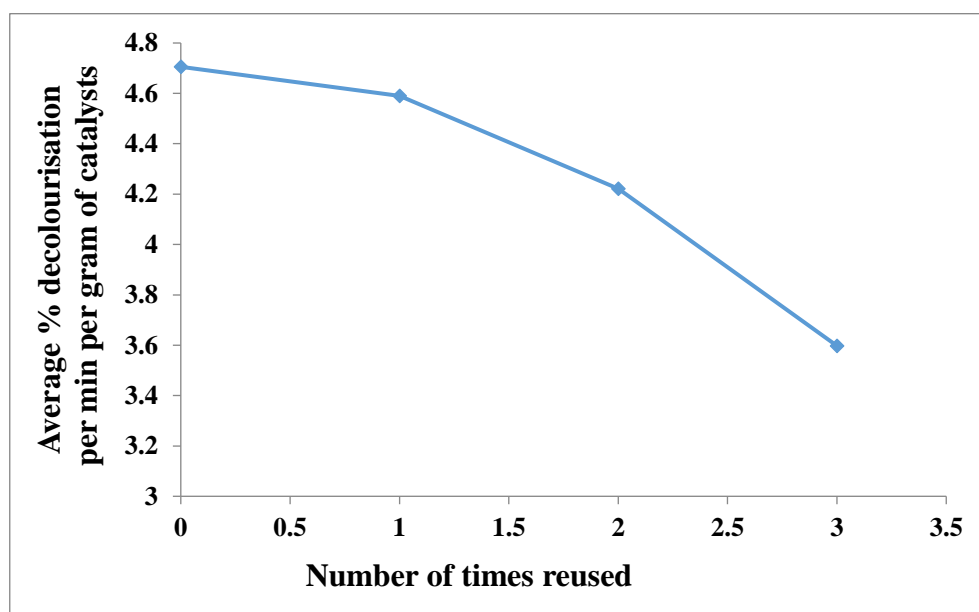


Figure 4.28: (b) Influence of reusing the catalyst on the average rate per gram of catalyst

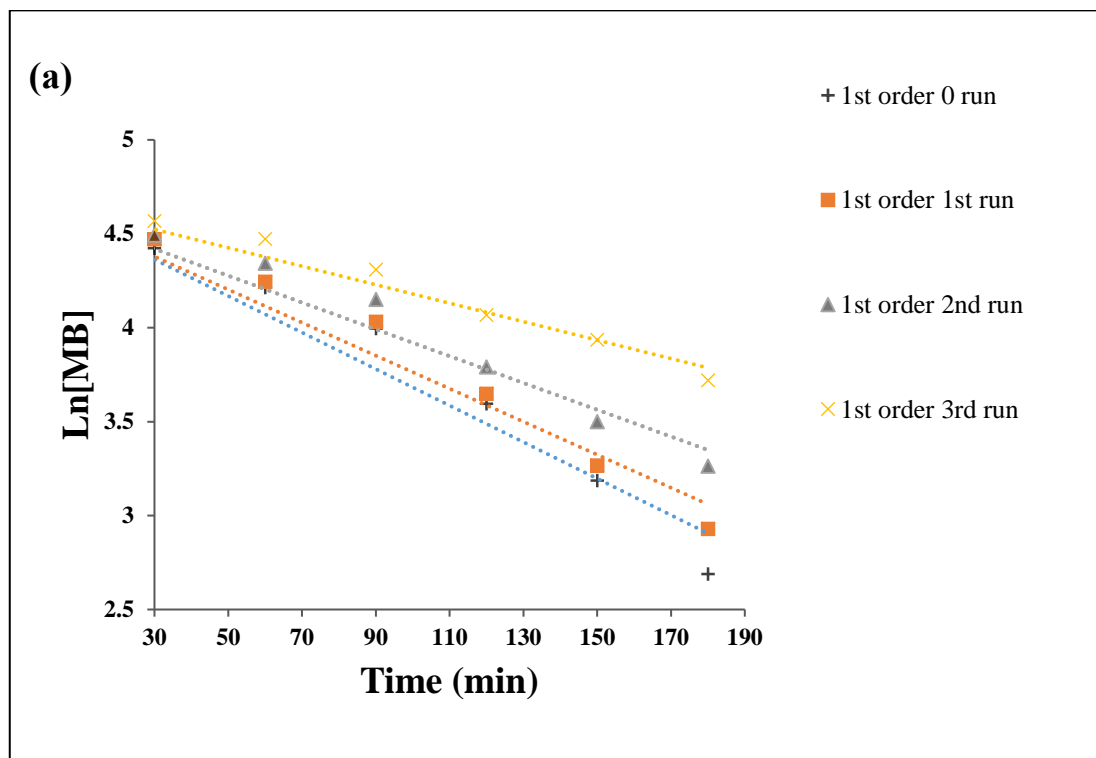


Figure 4.29: (a) pseudo-first order plots of the reusability study for degradation of MB of catalyst M1 in 180 min

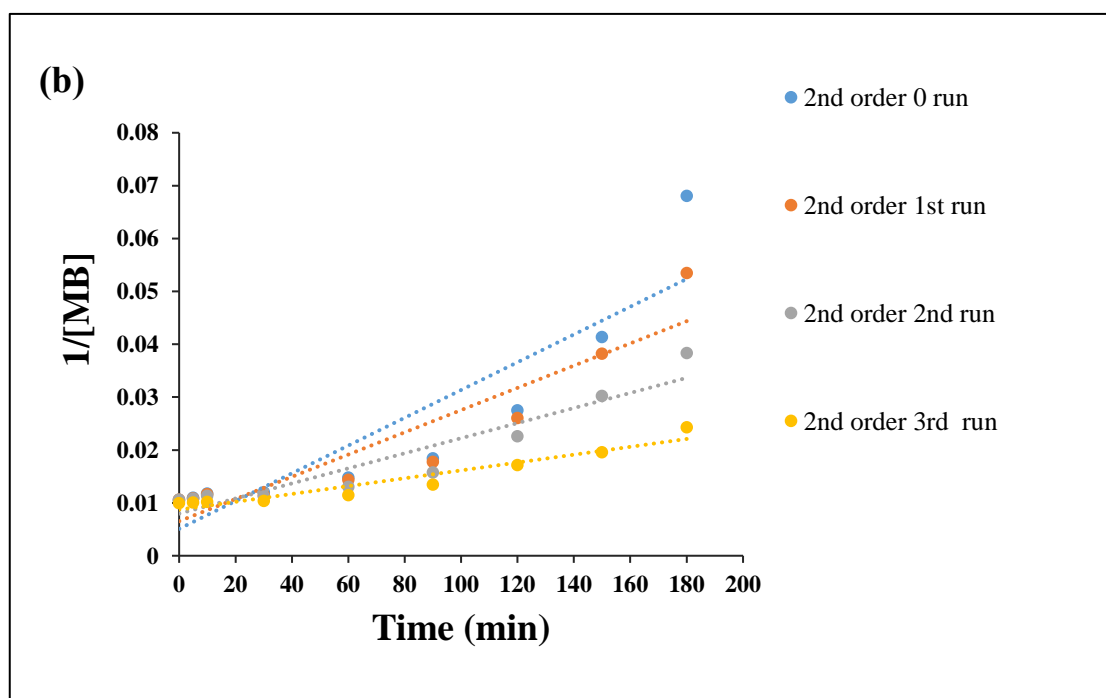


Figure 4.29: (b) pseudo-second order plots of the reusability study for degradation of MB of catalyst M1 in 180 min

Table 10.6: Calculation of regression coefficient R^2

Base type	Pseudo-first order K ($M^{-1}.s^{-1}$)	1 st order R^2	Pseudo second order K ($M^{-1}.s^{-1}$)	2 nd order R^2
0 run	1.16×10^{-2}	0.973	4.00×10^{-4}	0.856
1 st run	8.80×10^{-3}	0.963	2.00×10^{-4}	0.870
2 nd run	7.10×10^{-3}	0.958	1.00×10^{-4}	0.898
3 rd run	4.90×10^{-3}	0.967	7.00×10^{-5}	0.929

4.5.1.3 Effect of reaction temperature of catalyst synthesis on catalytic activity

The catalyst preparation temperature had a very small effect on the MB degradation when the precipitating agent, tetra methyl ammonium hydroxide (MM1, MM3 and MM3) was used with the highest and lowest degradation % differing by only 3.5 % with 37.2 %, 35.5 % and 33.7 %, respectively in 180 min (see **Figure 4.30**). All the catalysts had low activities for the degradation of MB dye. In contrast, the catalyst preparation temperature had a significant effect on the catalyst activity when NaOH was used as precipitation agent (**Figure 4.31**). In this case, the highest and lowest degradation differed by 27.3 % in 180 min. The highest catalytic efficiency was observed with the catalyst synthesised at 25 °C with NaOH as the precipitating agent, which may be due to cleaner surface area (less poisoning) and the smallest particle size obtained at 25 °C during synthesis, as seen in **Figure 4.1 (a-b)** in Chapter 4, where the XRD particle sizes were estimated to be < 5, 9.6 and 8.3 nm for M1, M3 and M5 respectively and 5.7, 7.6 and 8.8 nm for MM1, MM3 and MM5, respectively with M1 particles having the smallest size. The kinetics of the reactions were determined and recorded in **Table 4.8** and **Table 4.9**. Therefore, one may conclude that catalysts prepared with NaOH have less surface poisoning as compared to catalysts prepared with TMAOH, which may have resulted in better catalytic activity.

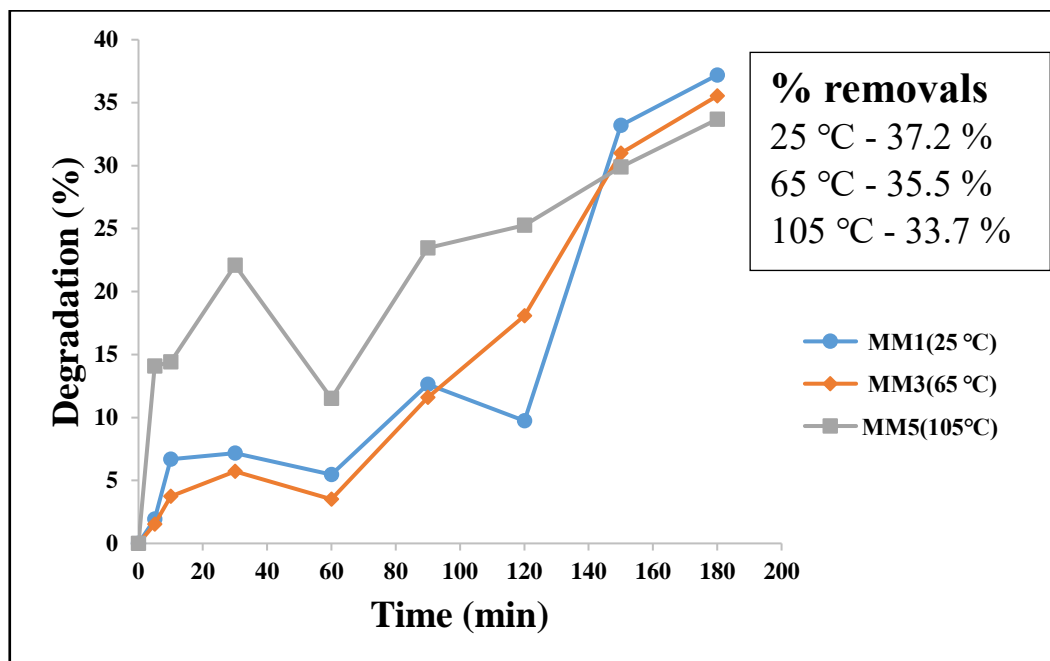


Figure 4.30: effect of catalyst synthesis temperature for MM1, MM3 and MM5 synthesised with iron (II) chloride and tetramethyl ammonium hydroxide base on MB degradation

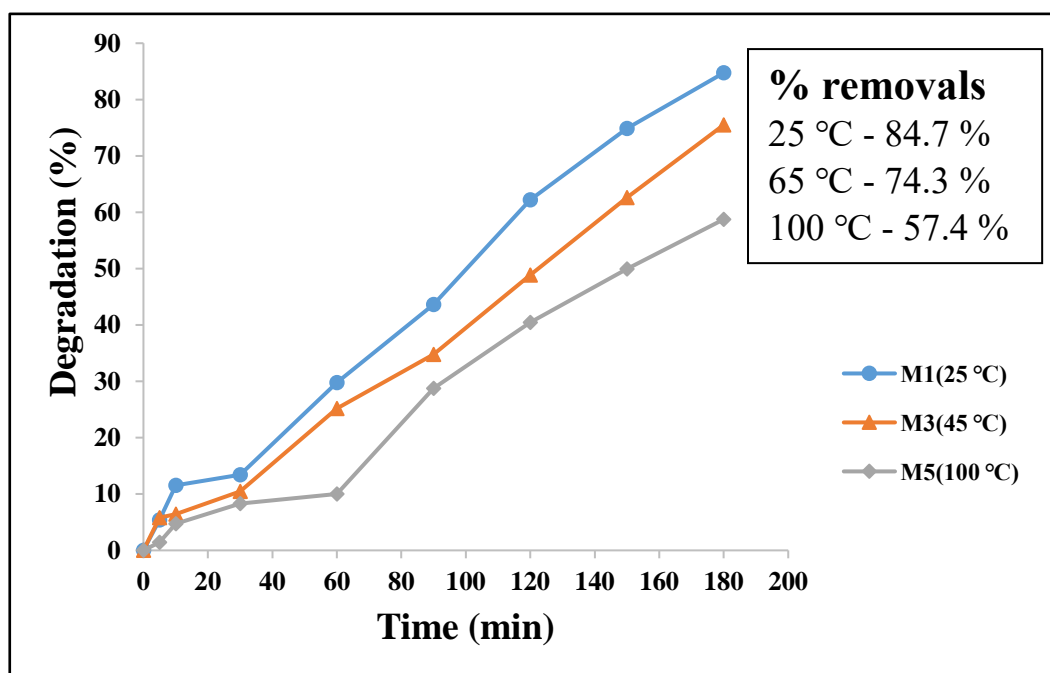


Figure 4.31: Effect of catalyst synthesis temperature for M1, M3 and M3 synthesised with iron (III) nitrate and NaOH base on MB degradation

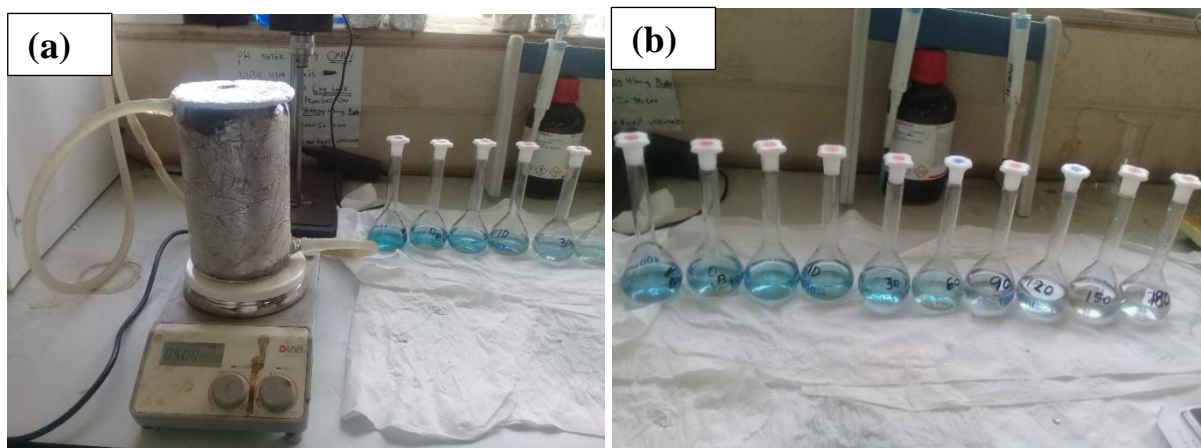


Figure 4.31.1: Picture of the Fenton reactor (a) and colour change (b) during MB removal

4.5.1.4 Effect of calculated TEM sizes on catalytic activity

Figure 4.32 shows that there is an increase in activity with a decrease in the TEM size. Which indicates that nanoparticles as measured by TEM are made up of an agglomeration of small crystallites or that the nanoparticles have strains/dislocations. Both strain and agglomeration will lead to a situation where the size will not correlate with the exposed surface area and catalytic activity.

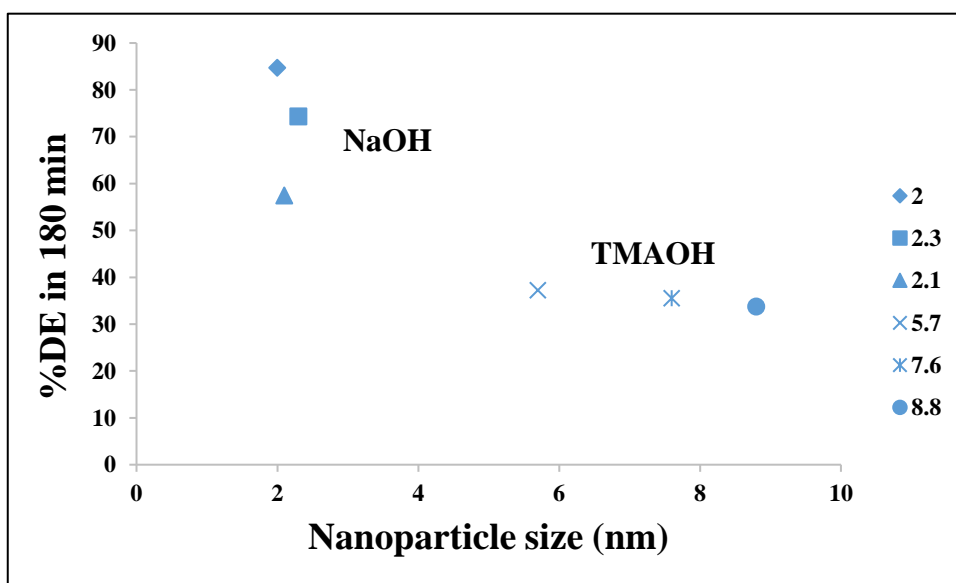


Figure 4.32: % MB removal over catalysts of different particles (M1:1.5, M3:2.3, M5:2.1, MM1:5.7, MM3: 7.6 and MM5:8.8 nm)

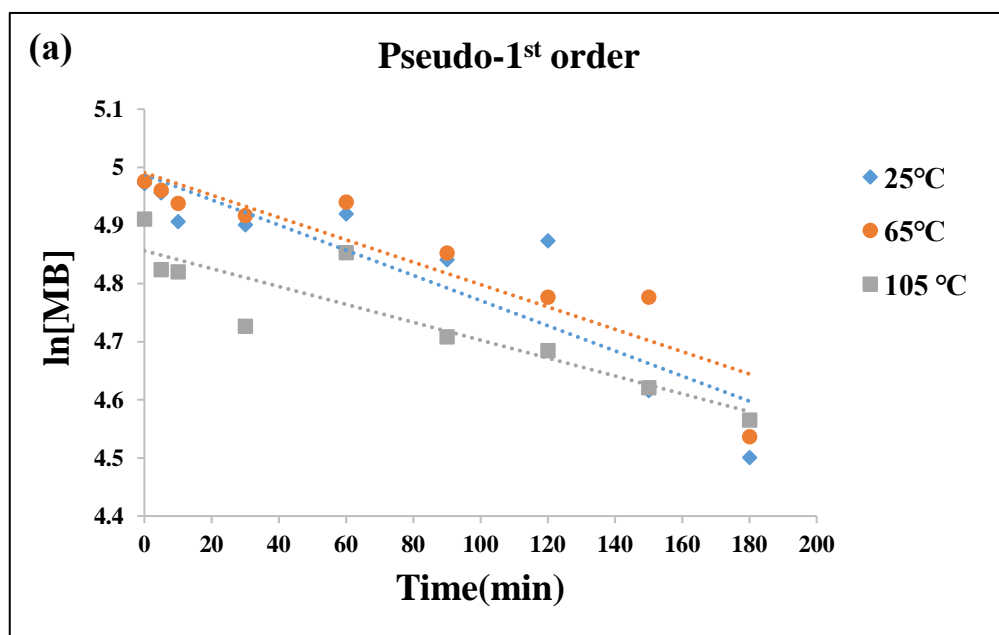
4.5.1.3.1 Kinetic models for effect of temperature on catalytic activity

The data obtained from the degradation of 100 mg/L were fitted into the pseudo-first and pseudo-second order kinetic models. The pseudo-first order and pseudo-second order reactions and its

kinetics were expressed in $\ln(C_0/C) = kt$ (**eq.1**) and $\frac{1}{c} = kt + \frac{1}{C_0}$ (**eq. 2**) where k is the rate constant, C_0 and C are the initial state and final state concentration of MB at time t (min). The correlation coefficients R^2 and rate constants are listed in

Figure 4.33 (a-b) and **Table 4.7** illustrate using pseudo-first and pseudo-second order model of the degradation of MB experiments performed on catalysts synthesised at 25, 65 and 105 °C with TMAOH as base exhibits less the R^2 values than expected for linear relationship experiments for both the pseudo first and second order model using catalyst synthesised at 25 and 65 °C following the pseudo first with R^2 values of 0.80, 0.84 ,respectively and the catalyst synthesised at 105 °C having the higher value of R^2 (0.83) pseudo-second order.

In contrast, catalysts synthesised with NaOH at temperatures of 25, 65 and 105 °C show a better R^2 values close to 1 (**Figure 4.34. (a-b)** and **Table 4.8**) for both pseudo first and second order kinetic model. However, pseudo-first order exhibits the highest values of R^2 for all catalyst with 0.97, 0.96 and 0.98 for 25, 65 and 100 °C respectively, which is an indication that the MB degradation process followed a kinetic adsorption model of pseudo-first order better.



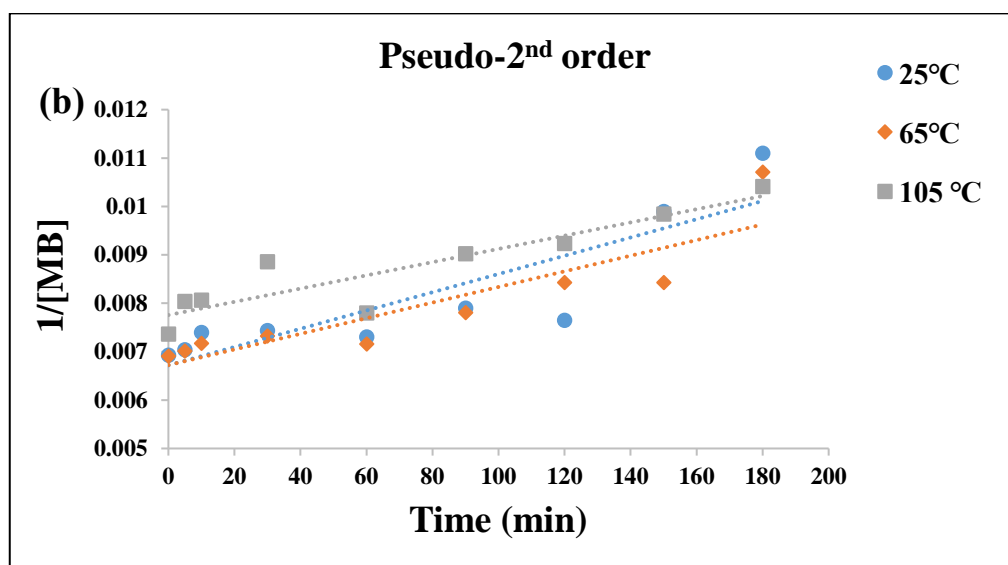


Figure 4.33: (a) pseudo-first order and (b) pseudo-second order plots of the degradation of MB using iron oxide particles prepared with 0.04 mL (CH₃)₄N-OH at 25, 65 and 105 °C

Table 4.7: Calculation of regression coefficient R²

Sample ID	Pseudo-first order k (s ⁻¹)	1 st order R ²	Pseudo-second order k (M ⁻¹ .s ⁻¹)	2 nd order R ²
MM1 (25 °C)	2.20 X10 ⁻³	0.79	2.00 X10 ⁻⁵	0.77
MM3 (65 °C)	1.90 X10 ⁻³	0.84	2.00 X10 ⁻⁴	0.80
MM5 (105 °C)	1.50 X 10 ⁻³	0.81	1.00 X10 ⁻⁴	0.83

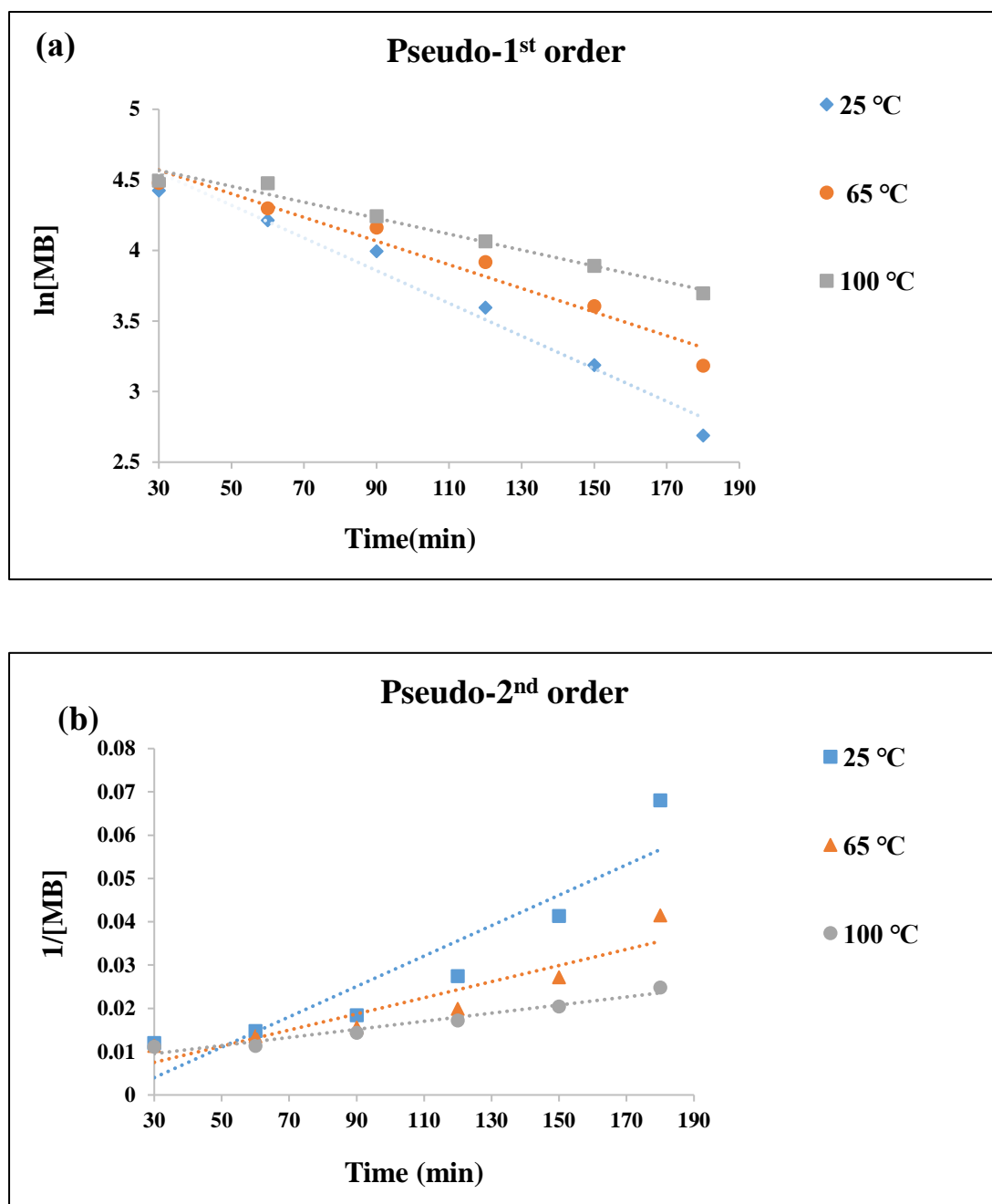


Figure 4.34: (a) pseudo-first order and (b) Pseudo-second order plots of the degradation of MB using iron oxide particles prepared with 0.04 mL NaOH at 25, 65 and 100 °C

Table 4.8: Calculation of regression coefficient R^2

Temperature (°C)	Pseudo-first order k (s ⁻¹)	1 st order R^2	Pseudo second order k (M ⁻¹ .s ⁻¹)	2 nd order R^2
25	1.16 X10 ⁻²	0.97	4.00 X10 ⁻⁴	0.86
65	8.40 X10 ⁻³	0.96	2.00 X10 ⁻⁴	0.86
100	5.70 X10 ⁻³	0.98	9.00 X10 ⁻⁵	0.96

4.5.1.4 Effect of type precipitating agent (base) during synthesis of catalyst on catalytic activity

Effect of the type of precipitating agent on catalytic activity was studied on catalysts synthesised with iron (II) chloride as a precursor with different types of base: MA1 (TMAOH), MA2 (TEAOH), MA3 (NaOH) and MA4 (C₂H₇N). The results are presented below. **Figure 4.35** and Table 18 show the evaluation of catalytic efficiency of the catalysts for the degradation of MB dye. The experiments were carried out with 10 mg/L MB in the presence of 20 mL H₂O₂ and ± 0.1021 g iron oxide catalysts (MA1, MA2, MA3 and MA4) for 3 h.

About 35.2, 19.6, 42.0 and 28.4 % in degradation was observed, respectively, which might be due to the degree of surface areas poisoning of the catalysts as a result of different precipitating agents used during catalyst synthesis. The Catalyst synthesised with NaOH shows high efficiency as compared to catalysts synthesised with other bases. The reason for this could be that NaOH results in cleaner catalyst was observed from the FTIR analysis of the samples in **Chapter 4 Figure 4.15 (a and b)**, where it shows that MA3 samples have less traces of the precipitating agent functional groups on the surface of the material compared to other samples. Therefore, this catalyst is highly effective for degradation of MB dye.

MA3 catalyst synthesised using NaOH shows that more surface area is available for catalysis due to absence of the adsorbed amine groups on the surface. The primary ammine (MA4) adsorbed on the catalyst's surface may block less sites in comparison to the quaternary ammonium compounds (MA2) and therefore has a less detrimental effect on the catalytic activity. Radoń *et al.* (2020) observations show that the Fe₃O₄ nanoparticles surface treated with malonic acid have shown to impact negatively on the catalytic efficiencies in photo-Fenton and Fenton processes, where their activities decreased from 86-35 % and from 93-85.5 % respectively, due to the malonic acid residuals blocking the active sites.

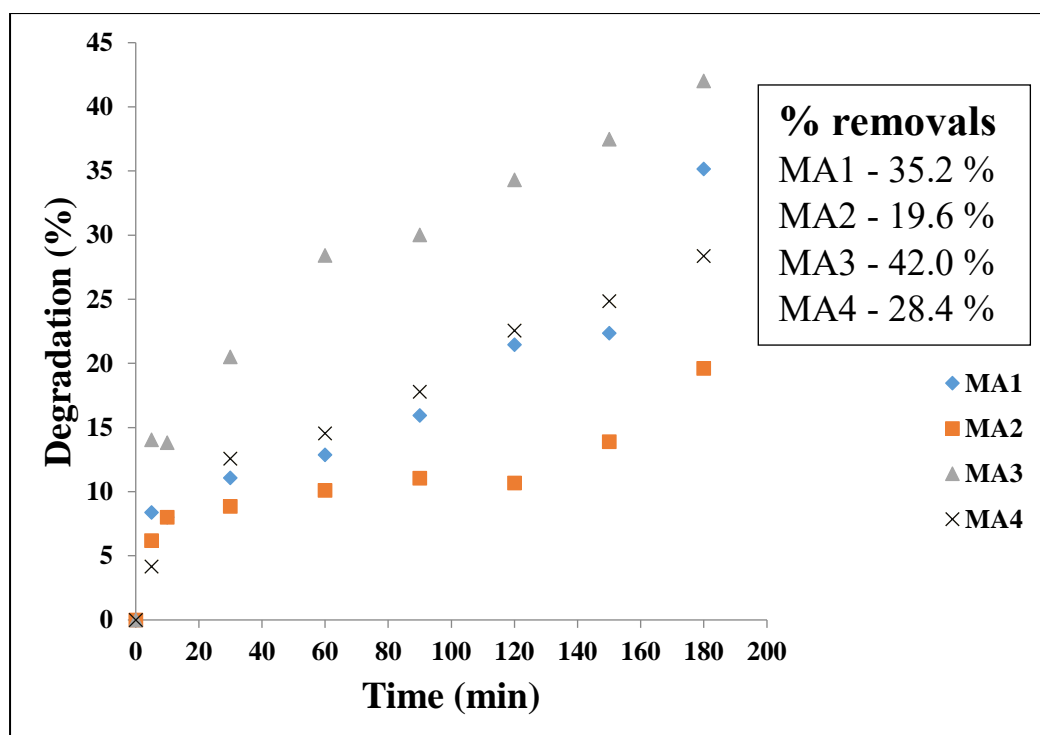


Figure 4.35: Effect of the type of base on MB degradation in 180 min

Table 4.9: Calculated sizes XRD, TEM and % MB removal for MA1, MA2, MA3 and MA4

Sample ID	TEM size(nm)	XRD size(nm)	% Removal at t = 60 min	% Removal at t = 120 min	% Removal at t = 180 min
MA1	6.4	4.5	12.9 %	21.5%	35.2 %
MA2	6.2	4.1	10.1 %	10.7 %	19.6 %
MA3	7.9	4.8	28.4 %	34.3 %	42.0 %
MA4	7.4	4.7	14.6 %	22.6 %	28.4 %

4.5.1.4.1 Kinetic models for effect of base type on catalytic activity

The pseudo-first order kinetics show the highest value of R^2 (0.947) for MA3 and R^2 (0.897) MA1 in **Figure 4.36(a-b)** and **Table 4.10**. These values suggest that one reactant was in excess and these catalysts showed to have the highest catalytic activities as compared to MA2 and MA4 for MB degradation. MA2 and MA3 catalysts fitted better in pseudo second order, which suggests that the adsorption step played a major role for the degradation of methylene blue (MB). In this regard, this suggests that adsorption and desorption processes have more effect than the degradation process thus the reaction depended on either the concentration of a single reactant or two different reactants on the concentration.

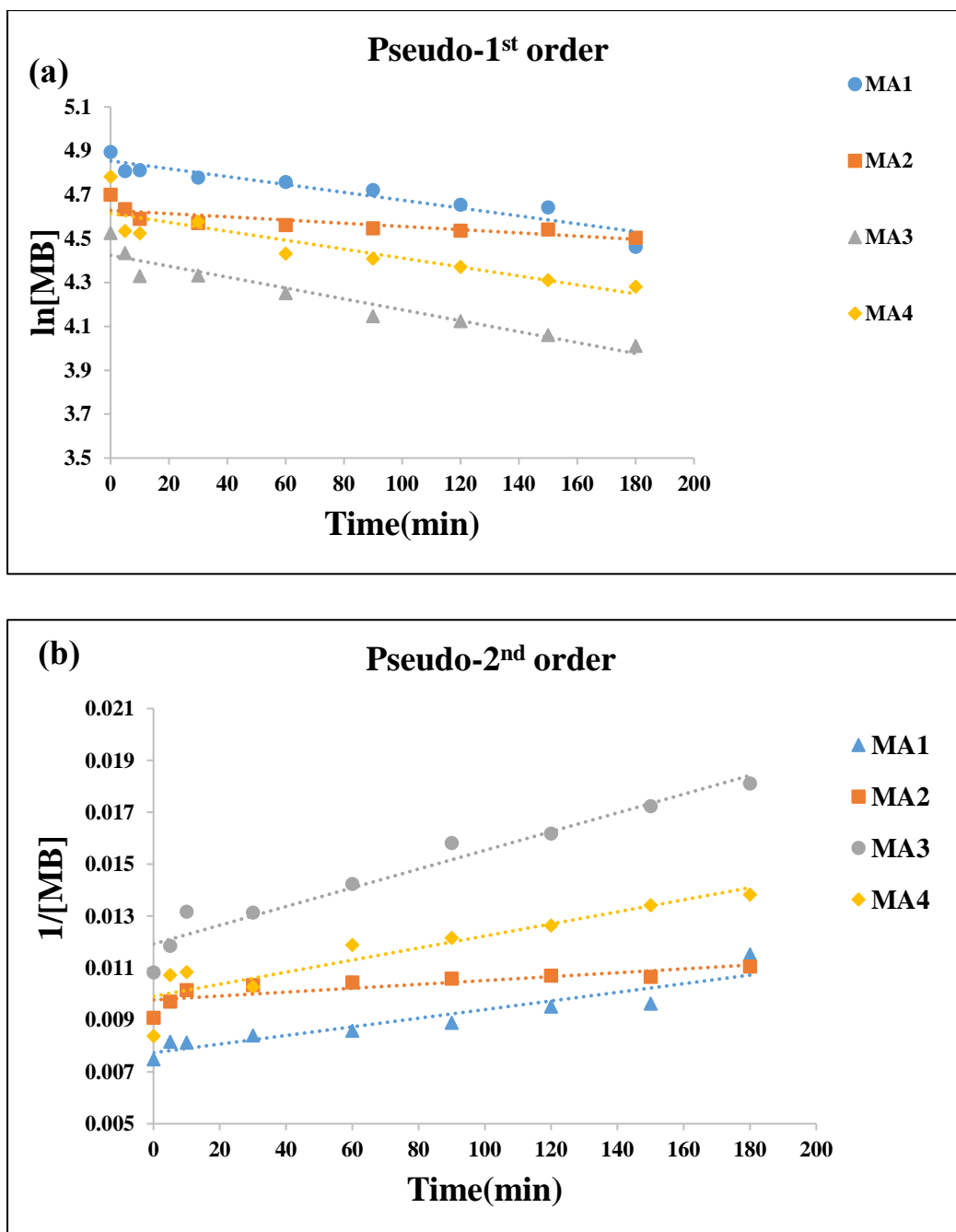


Figure 4.36: (a) pseudo-first order and (b) pseudo-second order plots of the degradation of MB using iron oxide particles prepared with 0.04 mL $(\text{CH}_3)_4\text{N-OH}$, $(\text{CH}_3\text{CH}_2)_4\text{N-OH}$, NaOH and $\text{C}_2\text{H}_7\text{N}$

Table 4.10: Calculation of regression coefficient R^2

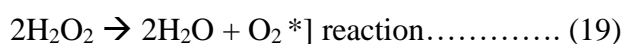
Base type	Pseudo-first order K (s^{-1})	1 st order R^2	Pseudo-second order K ($M^{-1}.s^{-1}$)	2 nd order R^2
MA1(TMAOH)	1.80×10^{-3}	0.90	2.00×10^{-5}	0.87
MA2(TEAOH)	7.00×10^{-4}	0.68	7.00×10^{-6}	0.71
MA3(NaOH)	5.00×10^{-3}	0.95	4.00×10^{-5}	0.92
MA4(C ₂ N ₇ H ₂)	2.00×10^{-3}	0.77	2.00×10^{-5}	0.83

4.5.2 OPTIMAZATION OF FENTON MB DEGRADATION REACTION PARAMETERS

Amongst the catalysts investigated, M1 (25 °C) showed the highest removal efficiency of the MB dye, therefore, this catalyst was used to study the factors influencing the parameters on MB removal.

4.5.2.1 Effect of temperature on the degradation of MB

It is reported that increasing operational temperature could be beneficial for both the oxidation rate and the level of the catalytic decomposition of synthetic dyes (Javaid & Qazi. 2019). In this study, the influence of reaction temperatures (20, 50 and 70 °C) on the degradation of 10 mg/L MB in the presence of 20 mL H₂O₂ and 0.1003 g iron oxide catalyst and the result are shown in **Figure 4.37**. Increasing reaction temperature from 27-50 °C increased with rate of reaction since the percentage degradation increasing from 12.8-84.7 % in 180 minutes. The rate of reaction decreased with a further increase in the temperature. According to Wang, Tian & Ning, (2014); Fida *et al.* (2017), an increase in temperature increased the reaction rate, to faster generation of •OH from H₂O₂, leading to increase with the degradation of MB. However, this was not observed during these reactions (but it was observed from 27 to 50 °C); in contrast, an increase in temperature may have caused more decomposition of the hydrogen peroxide (see Reaction 19); thus, lowering the concentration of hydrogen peroxide decreased the rate of reaction(maybe this is applicable at temperature above 50 °C as observed at 70 °C.



In a heterogeneous reaction it is assumed that the reaction takes place on the surface of the catalyst. One of the important steps is the adsorption of the reagents on the surface. Therefore,

a higher temperature can cause desorption of the reactants or less of the reagents to adsorb (assuming an exothermic physisorption and not an endothermic chemisorption). At a higher temperature, less of the reactions are adsorbed on the surface, decreasing the surface concentration of the reagents and leading to a decrease in the rate of reaction (as shown in eq. 20).

$$\text{rate} = k[\text{MB}^*][\text{H}_2\text{O}_2^*][\text{other surface species form the reagents}^*] \text{ eq. (20)}$$

Where * is the surface, MB* is MB adsorbed on the surface, k is the measured first-order rate constant and $[\text{H}_2\text{O}_2^*]$ is the concentration of the added hydrogen hydroxide. At high temperatures, side reactions can take place, causing fouling of the surface and decreasing the rate of the reaction.

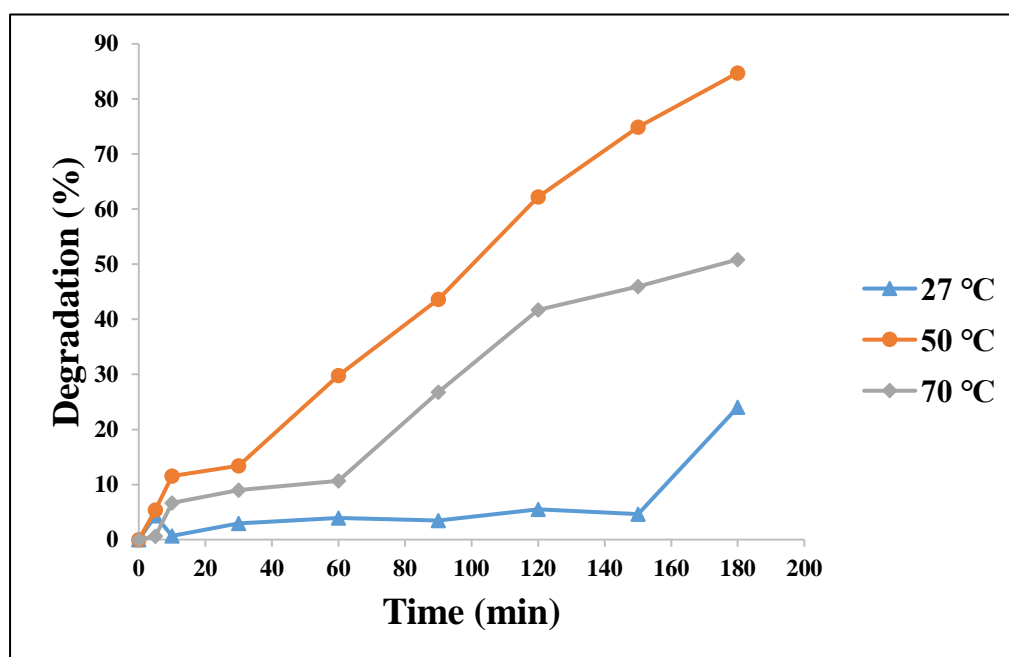


Figure 4.37: Influence of reaction temperature on the discoloration of MB (10 mg/L MB, $\text{H}_2\text{O}_2 = 20 \text{ mL}$, 0.1003 g iron oxide catalyst)

4.5.2.2 Effect of H_2O_2 dosage on the degradation of MB

Hydrogen peroxide (H_2O_2) as the source of $\bullet\text{OH}$, its dosage may affects the efficiency of the Fenton degradation process. Thus, the effect of the amount of H_2O_2 used on the degradation of 10 mg/L MB in the presence of 0.1003 g iron oxide catalyst at temperature of 50 °C, was studied and the results are shown in **Figure 4.38**. The removal efficiency of MB decreased as

the amount of H₂O₂ increased from 20-60 mL, with 84.7 %, 40.0 % and 22.1 % removal efficiencies in 180 min recorded when 20, 40 and 60 mL of H₂O₂ were used, respectively. Comparable results were also reported (Dulman *et al.*, 2012) where a decrease in degradation efficiency for dye decomposition resulted from increasing H₂O₂ amount above the optimum concentration, which may be as a result of the development of competition between the adsorption on the surface and the catalyst. Where the excessive H₂O₂ limits the adsorption of the dye molecules. Besides, too much H₂O₂ could reduce hydroxyl radicals and cause a scavenging effect of H₂O₂ on •OH radicals. The •OH and H₂O₂ forms HO₂ that is less reactive than the •OH radicals (Fida *et al.*, 2017), as described by eq.(2-3)

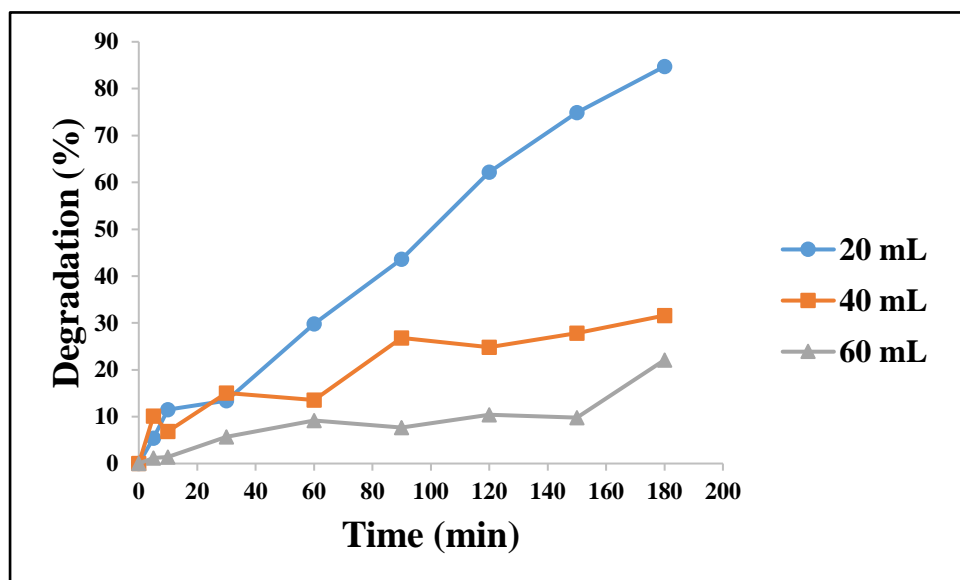
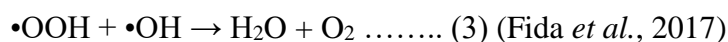
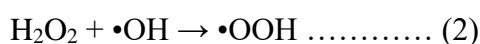


Figure 4.38: Influence of the amount of H₂O₂ on the removal of MB for M1 (50 °C, 10 mg/L MB, 0.1003 g iron oxide catalyst)

CHAPTER 5

CONCLUSIONS AND RECOMMENDATIONS

5.1 CONCLUSIONS

A number of researchers have investigated numerous preparation parameters and the ability of iron oxide nanoparticles to remove pollutants from aqueous solutions in both metallic and oxides forms. The main achievement of this study was the successful synthesis of iron oxide nanoparticles with crystallite sizes ranging from <5 to 15.5 nm and its application on Fenton catalytic reactions for the degradation of the organic pollutant (methylene blue dye). It was evident that the different preparation parameters affected the size, shape, phase and catalytic activity of the iron oxide nanoparticles. The use of different precipitating agents resulted in nanoparticles with different phases of magnetite/maghemite, hematite and a mixture of goethite-hematite phase. The reaction temperature determined the successfully synthesis of monodispersed iron nanoparticle. The shapes of iron oxide NPs were mostly affected by the precipitating agent used. Hydrogen peroxide as an oxidant successfully oxidised the $\text{Fe}(\text{OH})_3$ and $\text{Fe}(\text{OH})_2$ into Fe_2O_3 and FeOOH in different preparation conditions. It is observed that the amine containing precipitating $(\text{CH}_3)_4\text{N-OH}$, $(\text{CH}_3\text{CH}_2)_4\text{N-OH}$ and $\text{C}_2\text{H}_7\text{N}$ acted as capping agents, strongly adsorbing on the surface of the iron oxide nanoparticles leaving trace amounts as confirmed by FTIR analysis.

The use of different iron precursors also affected the shape, size and the phase of the synthesised iron oxide nanoparticles. It is observed that when $\text{FeCl}_2 \cdot 4\text{H}_2\text{O}$ was used, spherical and rods-like extension shaped iron oxide NPs were obtained sizes ranging from 4.5 - 8.8 nm and when $\text{Fe}(\text{NO}_3)_3 \cdot 9\text{H}_2\text{O}$ was used, sizes were in a ranged from <5 - 15.5 nm. The TEM results showed that an increase in the stoichiometric amount of the precipitating agents $(\text{CH}_3)_4\text{N-OH}$ and $(\text{CH}_3\text{CH}_2)_4\text{N-OH}$ resulted in aggregation, size increase and transformation of the iron oxide nanoparticle's shape from spherical to an irregular flower-like shape (hexagonal with rods extensions). The use of different precipitating agents at a stoichiometric amount affected the size of the nanoparticles and its catalytic activity. An increase in the preparation temperature also resulted in an increased nanoparticle size when NaOH was used as a base. The size was not significantly affected by the preparation temperature when $(\text{CH}_3)_4\text{N-OH}$ was used as base. However, this size increment did not affect the phase and shape of the nanoparticles.

The obtained nanoparticles showed to be red-shifted except for B3 sample, which is blue-shifted, from the bulk materials of iron oxide nanoparticles with others showing no optical properties. The highest Fenton catalytic activity achieved for the removal of methylene blue was 84.7 % in 3 h for M1. Catalysts synthesised with NaOH as precipitating agent showed better removal. However, catalysts synthesised with the amine-containing precipitating agents showed to have minimal removal. These catalysts seemed to contain the traces amounts of the base used on the surface. Catalysts synthesised with NaOH as precipitating agent the kinetic models fitted the 1st order reactions. In addition, the catalysts showed no good correlation between the XRD calculated particle size with their catalytic activity. The crystallite sizes also showed to be smaller than that measured by TEM, which may indicate that stacking faults/strain causing peak broadening leading to the discrepancy between the TEM and XRD size. The NaOH catalyst has shown stable repeatability after five tests under the same laboratory and operational conditions. Lastly, the same catalyst (M1) has shown more than 50 % for methylene blue removal after being reused in three cycles with some deactivation, which may be due to fouling and the formation surface organometallic-like compound with lower activity (poisoning). The effect of operational temperature on Fenton reactions showed that temperature of 50 °C had more effect on the degradation efficiency as compared to lower temperature of 27 °C and at higher temperature of 70 °C side reactions may have taken place, causing fouling of the surface and decreasing the rate of the reaction. The increase in the amount of H₂O₂ during the Fenton from 20-60 mL did not improve the degradation efficiency of the catalyst; rather, it caused more competition for adsorption on the surface of the catalyst between H₂O₂ dye molecules, which in turn caused a decrease in degradation efficiency.

5.2 RECOMMENDATIONS

XPS analysis should be done to confirm if the phase of the iron oxide nanoparticles is of magnetite or maghemite and HRTEM should also be employed to aid in getting more accurate size measurements for the nanoparticles. Capping agents such as PVP and other metals such as Si, Mn, Cu and Co could be used as support to form bimetallic with Fe to improve the catalytic activity and agglomeration. Furthermore, the catalysts could be employed for the degradation of other pollutants such as phenolics, pharmaceuticals, herbicides and personal care products.

Mass spectroscopy should also be applied to check whether degradation or discoloration occurred as well as the leaching test to provide the stability of the iron oxide catalyst in Fenton reaction. In addition, other AOPs methods of degradation such as photocatalysis, photo-Fenton and electro-Fenton need to be explored to check if the catalytic activity of the synthesised iron oxide can be improved.

REFERENCES

Adejumoke, A., Adebessin, B.O., Oluyori, A. P., Adelani-Akande, T.A., Dada, A.O & Oreofe, T.A. (2018). Water pollution: effects, prevention and climate impact. *Water Challenges of an Urbanizing World, InTech*, 10:35-36.

Ali, M.E., Rahman, M., Sarkar, S.M & AbdHamid, S.B. (2014). Heterogeneous Metal Catalysts for Oxidation Reactions. *Journal of materials*: 2-3.

Andrei, Y. Khodakov, A.Y., Griboval-Constant, A., Bechara, R & Zholobenko, V.L. (2002). Pore Size Effects in Fischer Tropsch Synthesis over Cobalt-Supported Mesoporous Silica. *Journal of Catalysis*. 206: 230–241.

Ameta, R., Chohadia, A.K., Jain, A & Punjabi, P.B. (2018). Advanced oxidation processes for wastewater treatment: Fenton and photo-Fenton processes. *Journal of Chemosphere*: 49-87.

Andrade, L., Fabris, D., Ardisson, D.V & Manuel, A. (2012). Effect of tetramethylammonium hydroxide on nucleation, surface modification and growth of magnetic nanoparticles. *Journal of Nanomaterials*: 1-11.

Balaprasad. A. (2012). Hydrothermal synthesis of rod shaped iron oxide nanoparticles. *Journal of Materials*: 2335.

Barnes, K.K., Kolpin, D.W., Furlong, E.T., Zaugg, S.D., Meyer, M.T & Barber, L.B. (2008). A national reconnaissance of pharmaceuticals and other organic wastewater contaminants in the United States groundwater. *Science of the Total Environment*, 402:192-200.

Carvalho, M.D., Henriques, F. Ferreira, L.P., Godinho, M & Cruz, M.M. (2013). Iron oxide nanoparticles: the influence of synthesis method and size on composition and magnetic properties. *Journal of Solid State Chemistry*, 201:144-152.

Chorkendorff, I & Niemantsverdriet, J. W. (2003). Concepts of Modern Catalysis and Kinetics. WILEY-VCH Verlag GmbH & Co. KGaA, Weinheim ISBN: 3-527-30574-2.

- Citakovi, N. (2011). Synthesis, morphology, microstructure and magnetic properties of hematite submicron particles. *Journal of Alloys and Compounds*, 509:7639-7644.
- Dahon, N.H., Kassim, M., Jain, N., Nurul, R.A. & Mohd, E.F. (2018). FTIR analysis on phase transformation of rust. *Journal of Global Scientific Research*: 54-62
- Dios, M.A.F., Iglesias, O., Pazos, M & Sanromán, M.A. (2014). Application of electro-Fenton technology to remediation of polluted effluents by self-sustaining process. *The Scientific World Journal*: 8.
- De Luna, L.A.V., Thiago, H.G., Pupo, R.F., Kummrow, F & Umbuzeiro, G.A. (2014). Aquatic toxicity of dyes before and after photo-Fenton treatment. *Journal of Hazard Materials*. 276:332-338.
- Dulman, V., Cucu-man, S.M., Iulian, R., & Buhaceanu, R. (2012). A new heterogeneous catalytic system for decolorization and mineralization of orange G acid dye based on hydrogen peroxide and a macroporous chelating polymer. *Dyes Pigments Journal*, 95: 79-88.
- Eman, H. R., Gehan H. F., Mennat Allah, K.S & Mohie Eldin, K. S. (2017). The impact of some organic and inorganic pollutants on fresh water (Rashid branch, River Nile), Egypt. *Journal of Water Resources*, 2: 432-448.
- Espinosa, J.C., Catalá, C., Navalóna, S., Ferrera, B., Álvaroa, M & Garcíaa, H.H. (2018). Iron oxide nanoparticles supported on diamond nanoparticles as an efficient and stable catalyst for the visible light assisted Fenton reaction. *Applied Catalysis B: Environmental*, 226:242-251.
- Fang Xiao-Liang, Li Yue, Chen Cheng, Kuang Qin, Gao Xiang-Zhi, Xie Zhao-Xiong, Xie Su-Yuan, Huang Rong-Bin, a& Zheng Lan-Sun. (2010). pH-Induced simultaneous synthesis and self-assembly of 3D layered β -FeOOH nanorods. *Langmuir*. 26(4). 2745–2750.
- Feng, Y., Liao, C & Shih, K. (2016). Copper-promoted circumneutral activation of H_2O_2 by $CuFe_2O_4$ spinel nanoparticles: mechanism, stoichiometric efficiency, and pathway of degrading sulfanilamide. *Chemosphere*, 154:573-582.
- Fida, H., Zhang, Y., Gao, S & Naeem, A. (2017). Heterogeneous Fenton degradation of organic dyes in batch and fixed bed using La-Fe montmorillonite as catalyst, *Journal of Colloid And Interface Science*, 490:859-868.

Javaid, R & Qazi, U.Y. (2019). Catalytic Oxidation Process for the Degradation of Synthetic Dyes: An Overview. *International Journal of Environmental Resources Public Health*, 16 (11): 2066.

Frison, R., Cernuto, G., Cervellino, A., Zaharko, O., Colonna, G.M., Guagliardi, A & Masciocchi, N. (2013). Magnetite-maghemite nanoparticles in the 5-15 nm range: correlating the core-shell Composition and the surface structure to the magnetic properties. *A Total Scattering Study Chemistry Material*, 25:4820-4827.

Greluk, M. & Hubicki, Z. (2010). Kinetics, isotherm and thermodynamic studies of reactive black 5 removal by acid acrylic resins. *Chemical Engineering*, 162(3):919-926.

Hassaan, M. A. & El Nemr, A. (2017). Advanced oxidation processes for textile wastewater treatment. *International Journal of Photochemistry and Photobiology*, 2(3):85-93.

Huang, X., Hou, X., Zhao, J & Zhang, L. (2016). Hematite facet confined ferrous ions as high efficient Fenton catalysts to degrade organic contaminants by lowering H₂O₂ decomposition energetic span. *Applied Catalysis B: Environmental*, 181:127-137.

Hossain, M., Islam, K.M.N & Rahman, I.M.M. (2012). An Overview of the persistent organic pollutants in the freshwater system, *Journal of Environmental Resources*.10:5772-48037.

Inyinbor, A.A., Adebisin, B.O., Oluyori, A. P., Adelani-Akande, T.A., Dada, A.O & Oreofe, T. A. (2018). Water pollution: effects, prevention and climate impact. *Water Challenges of an Urbanizing World, InTech*, 10: 61-63.

Jean-Pierre Jolivet, J.P., Chanéac, C & Tronc, E. (2019). Iron oxides chemistry: from molecular clusters to solid. *Journal of Chemistry*:481-487.

Kang, Y.S., Risbud,S., Rabolt, J.F & Stroeve, P. (1998). Synthesis and characterization of nanometer-size Fe₃O₄ and γ -Fe₂O₃ particles. *Chemistry of Materials*, 10(6):1733-1733.

Lassoued, A., Dkhil, B., Gadri, A & Salah Ammar,S. (2017). Control of the shape and size of iron oxide (α -Fe₂O₃) nanoparticles synthesized through the chemical precipitation method. *Results in Physics*, 7:3007-3015.

Kongsat, p., Kudkaew, K., Tangjai,J & O'Rear., E.A. (2021). Synthesis of structure-controlled hematite nanoparticles by a surfacant-assisted hydrothermal method and property

analysis. *Journal of Physics and Chemistry of Solids*, 148:109685.

Lee, H., Kim, C., Yang, S., Han, J.W. & Kim, J. (2011). Shape-controlled nanocrystals for catalytic applications. *Journal of Catalysis*:1-14.

Li, L., Ding, & Xue, J. (2010). A facile green approach for synthesizing monodisperse magnetite nanoparticles. *Journal of Material Resources*, 25(5):810.

Luca, C., Massa, P., Fenoglio, R & Cabello, F.M. (2014). Improved Fe₂O₃/Al₂O₃ as heterogeneous Fenton catalysts for the oxidation of phenol solutions in a continuous reactor. *Journal of Chemistry Technology Biotechnology*: 1-8.

Lu, M., Yao, Y., Gao, L., Mo, D., Lin, F & Lu, S. (2015). Continuous treatment of phenol over a Fe₂O₃/γ-Al₂O₃ catalyst in a fixed-bed reactor. *Journal of Water, Air, Soil and Pollution*, 226(87):1-13.

Mahdavi, M., Ahmad, M.B., Haron, M.J., Namvar, F., Nadi, B & Ab Rahman, M.Z., Amin, J. (2013). Synthesis, surface modification, and characterization of biocompatible magnetic iron oxide nanoparticles for biomedical applications. *Molecules*, 18(7):7533-7548.

Malato, S., Maldonado, M.I., Fernández-Ibáñez, P., Oller, I.; Polo, I. & Sánchez-Moreno, R. (2015). Decontamination and disinfection of water by solar photocatalysis: The pilot plants of the Plataforma solar de Almería. *Material. Science. Semiconductors. Process.* 42:15-23.

Manikandan, A., Vijaya, J., Judith M, J. Arul, K. L & Dinesh, A. J. (2014). Structural, optical and magnetic properties of Fe₃O₄ nanoparticles prepared by a facile microwave combustion method', *Journal of Industrial and Engineering Chemistry*. 20(4):2077-2085.

Mascolo, M.C, Pei, Y & Ring, T.A. (2013). Room temperature co-precipitation synthesis of magnetite nanoparticles in a large pH window with different bases. *Materials*, 6:5559-5560.

Miao, H., Li J., Lin Y.Q., Liu X.D., Zhang Q.M. & Fu J. (2011). Characterization of γ-Fe₂O₃ nanoparticles prepared by transformation of α-FeOOH. *Chinese Science Bulletin*, 56:2383-2388.

Mitar, I., Guć, L., Soldin, Ž., Vrankić, M., Paut, A., Prkić, A & Krehula, S. (2021) Rapid Microwave Method for Synthesis of Iron Oxide Particles under Specific Conditions. *Crystals*. 11:383.

Mohamed, A., Hassaan, M.A & El Nemr, A. (2017). Health and environmental impacts of dyes. *Mini Review: American Journal of Environmental Science and Engineering*, 1(3):64-67.

Mornet, S., Vasseur S., Grasset, F. & Duguet E. (2004). Magnetic nanoparticle design for medical diagnosis and therapy. *Journal of Materials Chemistry*, 14:2161-2175.

Morris D. A & Calvin H. Bartholomew, C.H. (2015). Heterogeneous Catalyst Deactivation and Regeneration. *Journal of Catalysis: Review*. 3:23-40.

Neamtu, M., Nadejde, C., Hodoroaba, V & Rudolf, J.(2018). Functionalized magnetic nanoparticles: Synthesis, characterization, catalytic application and assessment of toxicity. *Scientific Reports*:(3)1-11.

Oh, F. N. H., Tajabadi, M. & Khosroshahi, M. E. (2012). Effect of alkaline media concentration and modification of temperature on magnetite synthesis method using $\text{FeSO}_4/\text{NH}_4\text{OH}$. *International Journal of Chemical Engineering and Applications*, 3(3):3-7.

Ozel, F., Kockar, H. & Karaagac, O. (2015). Growth of iron oxide nanoparticles by hydrothermal process : Effect of reaction parameters on the nanoparticle size. *Journal of Superconductors Novel Magnetite*, 28:823-829.

Özer, A, & Dursun, G. (2007). Removal of methylene blue from aqueous solution by dehydrated wheat bran carbon. *Journal of Hazard Materials*, 146(1):262-269.

Pariente, M. I., Martinez, F & Melero, J. A. (2008). Heterogeneous photo-Fenton oxidation of benzoic acid in water: effect of operating conditions, reaction by-products and coupling with biological treatment. *Applied Catalysis*, 85(1-2):24–32

Parimala, L & Santhanalakshmi, J. (2014). Studies of iron nanoparticles catalysed reduction of substituted aromatic ketones to alcohols. *Journal of Nanoparticles*: 10.

Pastrana-Martínez, L.M., Gomes, H.T., Drazic G., Faria, J.L & Silva A.M.T. (2014). Hydrothermal synthesis of iron oxide photo-Fenton catalysts: the effect of parameters on morphology, particle size and catalytic efficiency. *Global Nest Journal*, 3(16):474-484.

- Pearce, C.I., Lloyd, J.R. & Guthrie, J.T. (2003). The removal of colour from textile wastewater using whole bacterial cells: *A Review, Dyes and Pigments*, 58(3):179-196.
- Pushpalatha, M & Krishna, M.B. (2017). Electro- Fenton process for waste water treatment. *A Review International Journal of Advanced Research, Ideas, and Innovations in Technology*, 3:439-440.
- Qi, B. (2013). Factors controlling synthesis of iron oxide nanoparticles and the effect of surface charge on magnetic hyperthermia. *Materials Science and Engineering Journal*: 1173.
- Radoń, A., Łoński, S. K., Adziołka-Gaweł, M. G., Ebara P., Lis, M., Łukowiec, D & Babilas, R. (2020). Influence of magnetite nanoparticles surface dissolution, stabilization and functionalization by malonic acid on the catalytic activity, magnetic and electrical properties, *Colloids and Surfaces, Physicochemical and Engineering Aspects*: 154-182.
- Rashed, M.N. (2013). Adsorption technique for the removal of organic pollutants from water and wastewater. Intech: organic pollutants-monitoring, risk and treatment. Chapter 7. Prof. M. Nageeb Rashed (Ed.) DOI: 10.5772/54048. [Online]. Available from: <https://www.intechopen.com/books/organic-pollutants-monitoring-risk-andtreatment/adsorption-technique-for-the-removal-of-organic-pollutants-from-water-andwastewater>. (Accessed: 5 October 2019).
- Rusevova, K., Kopinke, F.D & Georgi, A. (2012). Nano-sized magnetic iron oxides as catalysts for heterogeneous Fenton-like reactions-influence of Fe(II)/Fe(III) ratio on catalytic performance. *Journal of Hazard Materials*, 15:241-242.
- Rossi, L.M. & Fiorio, J., L, Garcia, M A. S. & Ferraz, C. P. (2018).The role and fate of capping ligands in colloidally prepared metal nanoparticle catalysts. *Journal of Dalton Transitions*, 47(17):5889-5915.
- Saha, S. & Bhunia, A. K. (2013). Synthesis of Fe₂O₃ nanoparticles and study of its structural, optical properties. *Journal of Physical Sciences*: 191-195.
- Santoyo-Salazar, J.S., Perez, L., Abril, O., Phuoc, L.T., Ihiawakrim, D., Vasquez, M., Grenache, J.M., Begin-Colin, S. & Pourroy.G. (2011). Magnetic iron oxide nanoparticles in 10-40 nm range: composition in terms of magnetite/maghemite ratio and effect on the magnetic properties. *Chemistry Materials*, 23: 1379-1386.

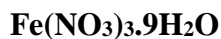
- Schwaminger, S. P., Surya, Rifki, F., Simon, W., Andreas. W., Florian, F. & Paula, B. S. (2017). Formation of iron oxide nanoparticles for the photooxidation of water : Alteration of finite size effects from ferrihydrite to hematite. *Journal of Crystals Engineering Community*: 1-9.
- Sharma, M., Kalita, P., Senapati, K.K. & Garg, A. (2018). Study on magnetic materials for removal of water pollutants. *InTech: Emerging Pollutants-Some Strategies for the Quality Preservation of Our Environment*, 10:62.
- Shima, Q., Pouran, R., Aziz, A.R.A., Mohd, W. & Wan, A. (2014). Review on the advances in photo-Fenton oxidation system for recalcitrant wastewaters. *Journal of Industrial Engineering Chemistry*, 21:53-69.
- Singh, R.L., Singh P.K. & Singh, R.P. (2015). Enzymatic decolorization and degradation of azo dyes—A review. *International Biodeterior Biodegradation*, 104:21-31.
- Sun, S. and Zeng, H. (2002). Size-controlled synthesis of magnetite nanoparticles. *Journal of amorphous chemistry. Society*, 124 (31):8204-8205.
- Sreeja, P.H & Sosamony, K.J. (2016). A Comparative Study of Homogeneous and Heterogeneous Photo-Fenton Process for Textile Wastewater Treatment Technology. *Procedia Technology*, 24:217-223.
- Sun, J., Chen, Y. & Chen, J. (2016). Morphology effect of one-dimensional iron oxide nanocatalysts on Fischer–Tropsch synthesis. *Catalysis Scientific. Technology*, 20(6):7505-7511.
- Tadic, M., Citakovic N., Panjan M., Stojanovic Z., Markovic D. & Spasojevic V. (2011). Synthesis, morphology, microstructure, and magnetic properties of hematite submicron particles. *Journal of Alloys and Compounds*, 509:7639-7644.
- Vidyasagar, C. C., Naik, Y. A., Venkatesha, T. G. & Viswanatha, R. (2012). Solid-state synthesis and effect of temperature on optical properties of CuO nanoparticles. *Nano-Micro Letter*, 4(2):73-77.
- Wan, D., Li, W., Wang, G. & Wei, X. (2016). Size-controllable synthesis of Fe₃O₄ nanoparticles through oxidation-precipitation method as heterogeneous Fenton catalyst. *Chem and Chemical Engineering*, 1(17):2613-2614.

- Wang, P., Bian, X. & Li, Y. (2012). Catalytic oxidation of phenol in wastewater: a new application of the amorphous Fe₇₈Si₉B₁₃ alloy. *Chinese Scientific Bulletin*, 157:33-40
- Wang, J & Tang, J. (2021). Fe-based Fenton-like catalysts for water treatment: Preparation, characterization and modification. *Chemosphere Journal*: 276.
- Wang, Q., Tian, S. & Ning, P. (2014). Degradation mechanism of methylene blue in a heterogeneous Fenton-like reaction catalyzed by ferrocene. *Engineering and Chemical Journal*, 53:643-649.
- Wei, Y., Zhang, C., Chang, Q., Wang, X., Niu, L., Xu, J., Yang, Y & Li, Y. (2017). Synthesis of monodisperse iron oxide nanoparticles: effect of temperature, time, solvent, and surfactant. *J. inorganic and nano-metal chemistry*, 47(10): 1375-1379.
- Wintgens, T., Salehi, F., Hochstrat, R. & Melin, T. (2008). Emerging contaminants and treatment options in water recycling for indirect potable use. *Water Science Technology*, 57:99-107
- Wu, W., He, A. Q. & Jiang, A. C. (2008). Magnetic iron oxide nanoparticles : synthesis and surface functionalization strategies. *Nanoscale Resources Letter*, 3:397-415.
- Xu, L. & Wang, J. (2011). A heterogeneous Fenton-like system with nanoparticulate zero-valent iron for removal of 4-chloro-3-methyl phenol. *Journal of Hazardous Materials*. Elsevier B.V, 186(1):256–264.
- Xu, P., Zeng, G.M., Huang, D.L., Feng, C.L., Hu, S., Zhao, M.H., Lai C., Wei, Z., Huang, C., Xie, G.X. & Liu, Z.F. (2012). Use of iron oxide nanomaterials in wastewater treatment: A review, *Science of The Total Environment*, 424:1-10
- Xie, Z., Wang, C. & Yin, L. (2017). Nickel-assisted iron oxide catalysts for the enhanced degradation of refractory DDT in heterogeneous Fenton-like system. *Journal of Catalyst*, 353:11-18.
- Yu, X., Lin, X., Feng, W & Li, W. (2019). Enhanced catalytic performance of a bio-templated TiO₂ UV-Fenton system on the degradation of tetracycline. *Appl. Surf. Sci*, 465:223-231.
- Zheng, Y.Y., Sun, Q., Duan, Y.H., Zhai, J., Zhang, L.L & Wang, J.X. (2020). Controllable synthesis of monodispersed iron oxide nanoparticles by an oxidation-precipitation combined with solvothermal process. *J. Materials Chemistry and Physics*, 252: 123431.

- Zhang, H., Bayne, M., Fernando, S., Legg, B., Zhu, M., Lee Penn, R & Banfield, J.F. (2011). Size-dependent bandgap of nanogoethite. *The Journal of Physical Chemistry*, 115:17704 -17710.
- Zhao, C., Arroyo-mora, L.E., Decaprio, A.P., Sharma, V.K., Dionysiou, D.D & Shea, K.E.O. (2014). Reductive and oxidative degradation of iopamidol, iodinated X-ray contrast media, by Fe (III)-oxalate under UV and visible light treatment. *Water Resources*, 67:144-153.
- Zhang, T., Qian. C & Dong L. (2019). Preparation of particle reusable heterogeneous catalyst $\text{Fe}_3\text{O}_4/\text{ATP}$ for methylene blue decolorization. *International Journal of Environmental Science and Technology*, 10:343-349.
- Zheng, Y., Cheng, Y., Bao, F & Wang, Y. (2006). Synthesis and magnetic properties of Fe_3O_4 nanoparticles. *Material Resources*, 41(3): 525-529.
- Zheng, Y.Y., Sun, Q., Duan, Y.H., Zhai, J., Zhang, L.L & Wang, J.X. (2020). Controllable synthesis of monodispersed iron oxide nanoparticles by an oxidation-precipitation combined with solvothermal process. *J. Materials Chemistry and Physics*, 252: 123431.
- Zhu, Y., Jiang, F.Y., Chen, K.X., Kang, F.Y & Tang Z.K. (2011). Size-controlled synthesis of monodisperse superparamagnetic iron oxide nanoparticles. *Journal of Alloys and Compounds*, 509:8549-8553.

APPENDIX A

Calculation for mass of the two iron salts required for the formation of iron oxide nanoparticles.



$$\begin{aligned} m \text{Fe}(\text{NO}_3)_3 \cdot 9\text{H}_2\text{O} &= n * Mr \\ &= 0.02 \text{ mol} * 404 \text{ g/mol} \\ &= 8.0817 \text{ g} \end{aligned}$$



$$\begin{aligned} m\text{FeCl}_2 \cdot 4\text{H}_2\text{O} &= n * Mr \\ &= 0.02 \text{ mol} * 198.812 \text{ g/mol} \\ &= 3.9762 \text{ g} \end{aligned}$$

Calculation for 2M HCl required to wash iron oxide nanoparticles during the preparation process.

32% HCl has a density of 1.16kg/l

Molecular weight HCl = 36.46g/mol

$$C_1 = \frac{\rho \times \% \times 1000}{Mr \times 100}$$

$$C_1 = \frac{\rho \times \% \times 10}{Mr}$$

$$C_1 = \frac{1.16 \text{ g/mL} \times 32 \times 10}{36.45 \text{ g/mol}}$$

$$C_1 = 10.18\text{M}$$

$$C_1 V_1 = C_2 V_2$$

$$V_1 = \frac{C_2 V_2}{C_1}$$

$$V_1 = \frac{2\text{M} \times 1000 \text{ mL}}{10.18 \text{ mL}}$$

$$V_1 = 196.5 \text{ mL}$$

Calculation of the crystalline size from XRD (Lassoued *et al.*, 2017)

The Scherrer equation may be written as:

$$\tau = \frac{K\lambda}{\beta \cos \theta}$$

Where:

- T = mean size of the ordered (crystalline) domains, which could be smaller or equal to the grain size.
- K = dimensionless shape factor, with value close to unity, the shape factor has a typical value of about 0.9 but varies with actual shape.
- λ = X-ray wavelength nm
- B = line broadening at half maximum intensity (FWHM), which stands for full width at half maximum) after subtracting the instrumental line broadening in radians. This quantity is also sometimes denoted as $\Delta (2\theta)$.
- θ is the Bragg angle ($2\theta^\circ$).

Example of crystallite size calculation for Fe_3O_4 with a spinel structure for MA1 at peak (311) is as follows

$$\text{Center} = 35.57 (2\theta^\circ)$$

$$\text{FWHM} = 0.9329 (2\theta^\circ)$$

The center and FWHM were determined using a Fityk programme and converted to radians

$k\lambda B \cos \theta$

$$\begin{aligned} \tau &= \frac{K\lambda}{\beta \cos \theta} \\ &= \frac{0.9 \times 0.15418}{\cos\left(\frac{0.62089}{2}\right) * 0.32564} \end{aligned}$$

$$= 4.5 \text{ nm}$$

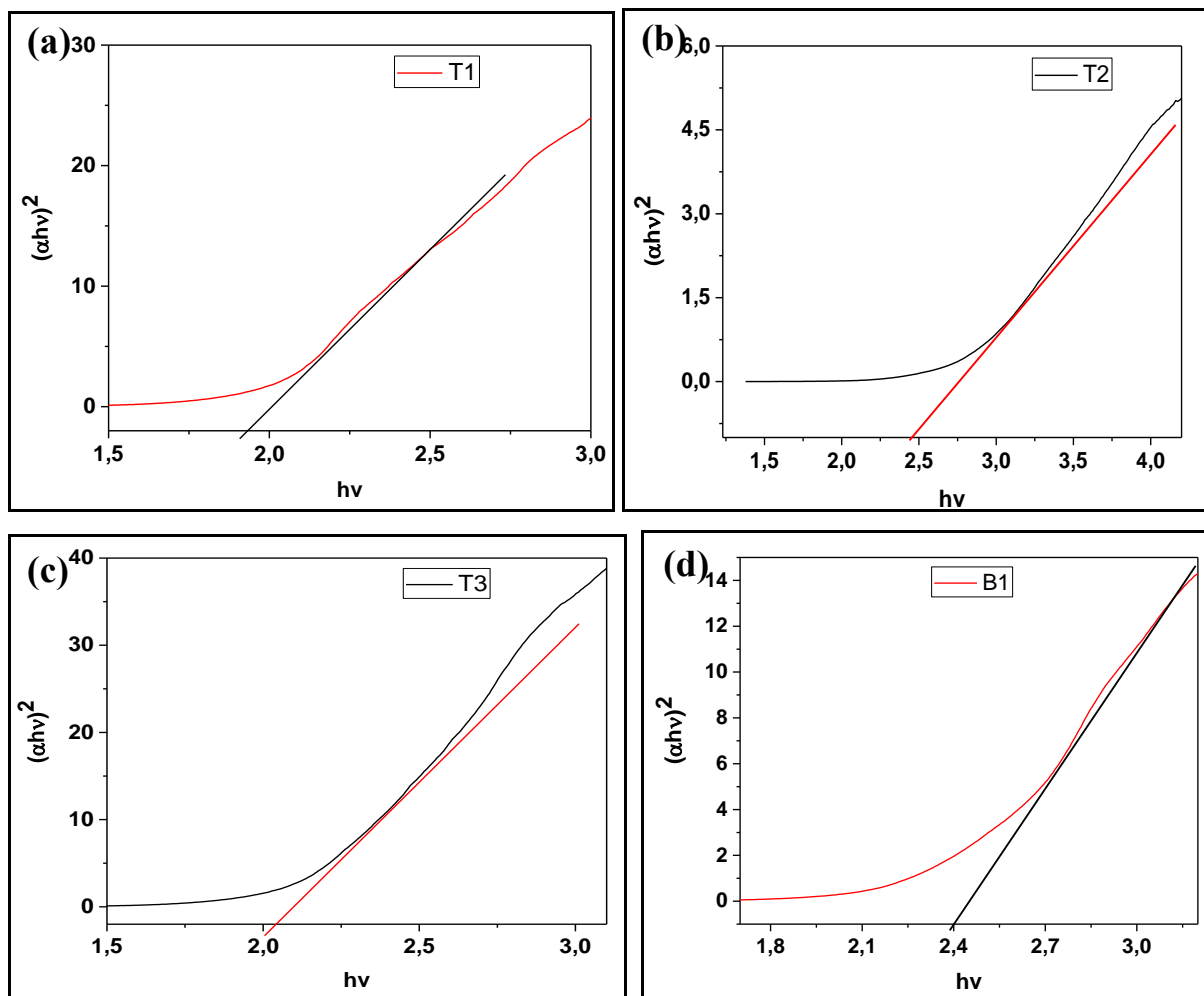
Degradation percentage removal calculation

C_0 = initial degradation concentration

C = final degradation concentration

$$\begin{aligned}\% \text{ Removal} &= \frac{C_0 - C}{C_0} * 100 \% \\ &= \frac{0.963 - 0.147}{0.963} * 100 \% \\ &= 84.7 \%\end{aligned}$$

Effect of type and amount of precipitating agent (TMAOH and TEAOH) direct and indirect Tauc plots.



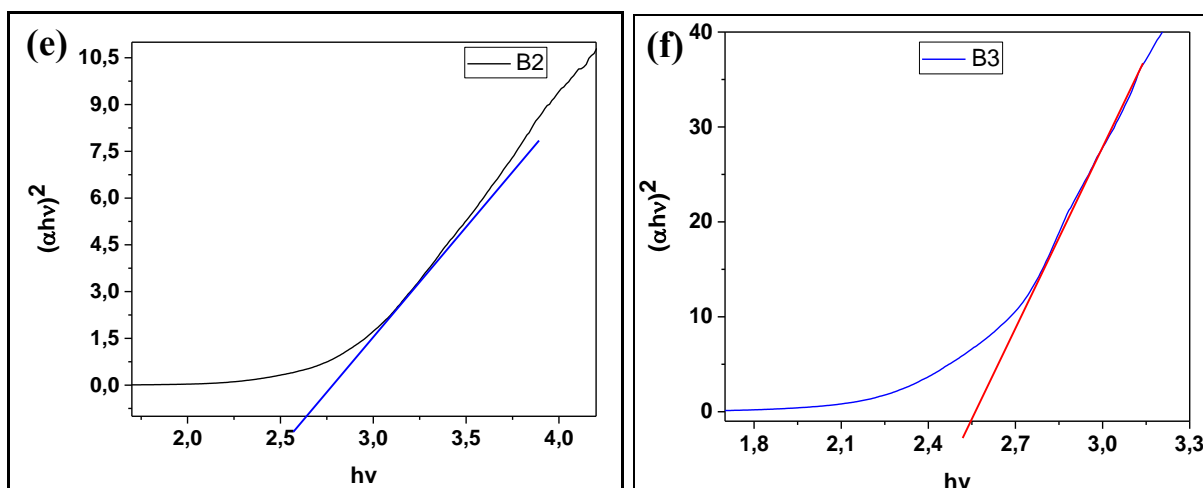
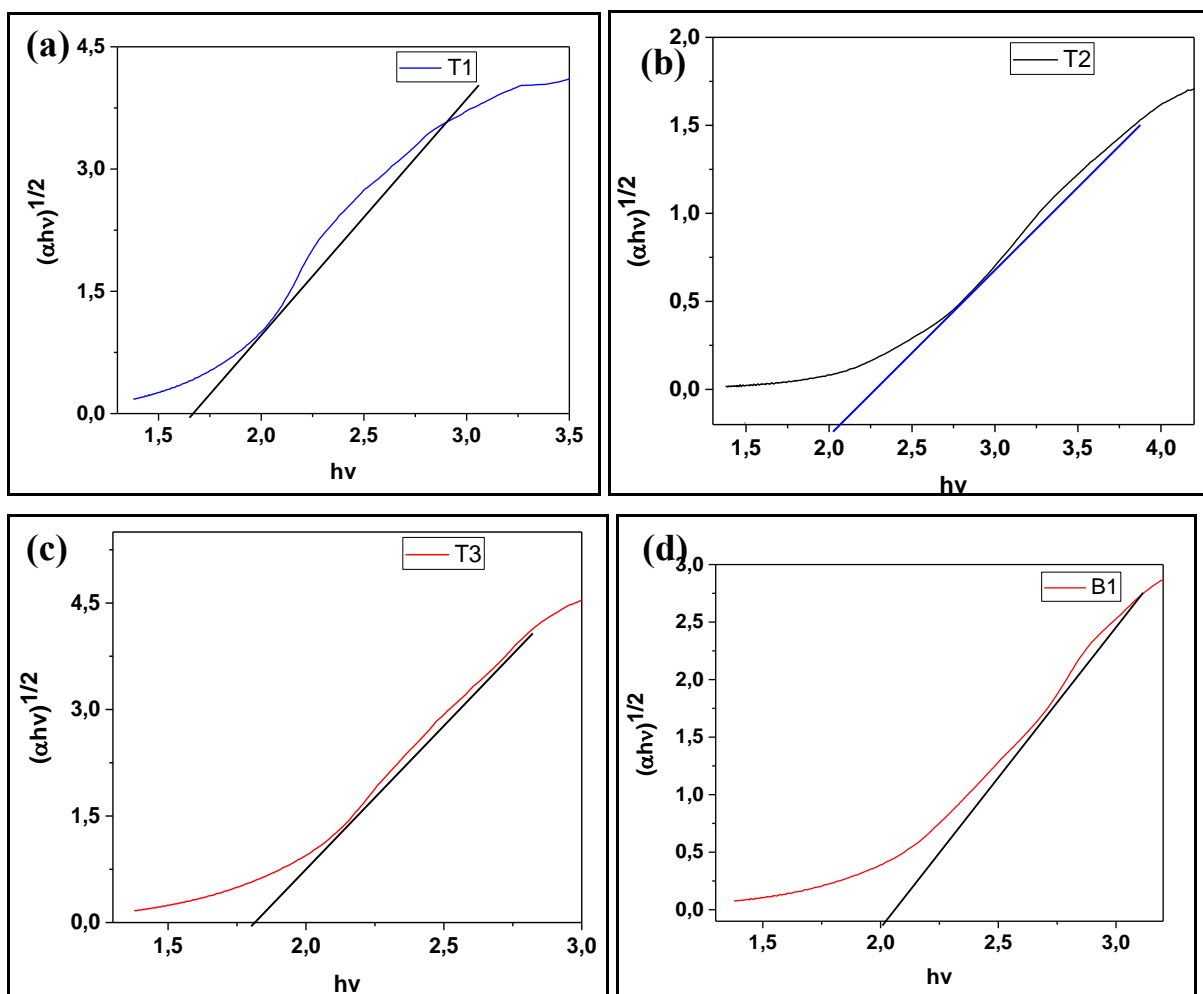


Figure 4.11.1: (a-f) Tauc plot for direct bandgap of iron oxide nanoparticles. The intercept with the horizontal axis shows the value of the bandgap at different temperature with T1: 0.06 mol TMAOH, T2: 0.09 mol TMAOH, T3:0.12 TMAOH, B1: 0.06 mol TEAOH, B2: 0.09 mol TEAOH and B3:0.12 mol TEAOH



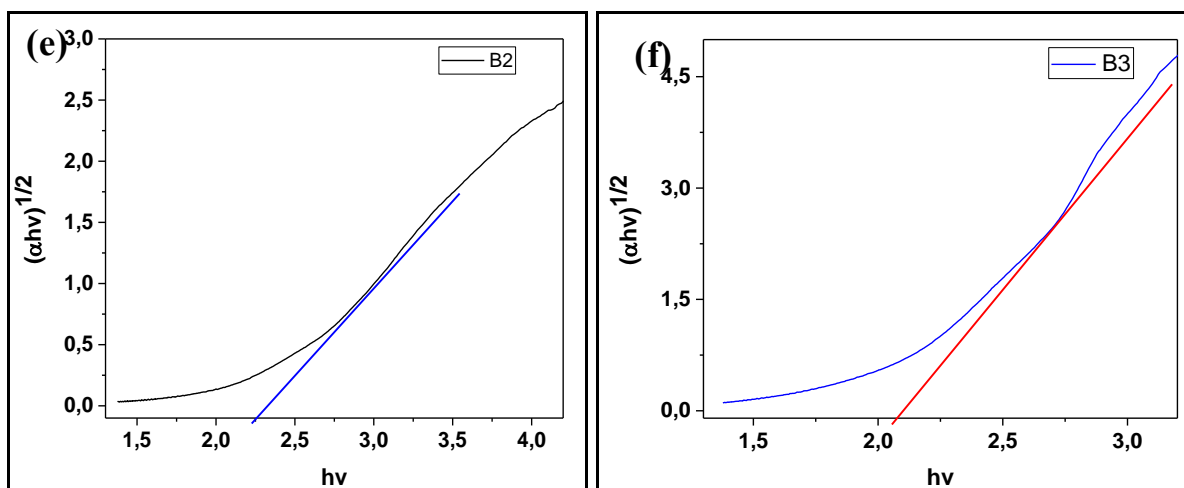


Figure 4.11.2: (a-f) Tauc plot for indirect bandgap of magnetite nanoparticles. The intercept with the horizontal axis defines the value of the bandgap at different temperature with T1: 0.06 mol TMAOH, T2: 0.09 mol TMAOH, T3: 0.12 TMAOH, B1: 0.06 mol TEAOH, B2: 0.09 mol TEAOH and B3: 0.12 mol TEAOH

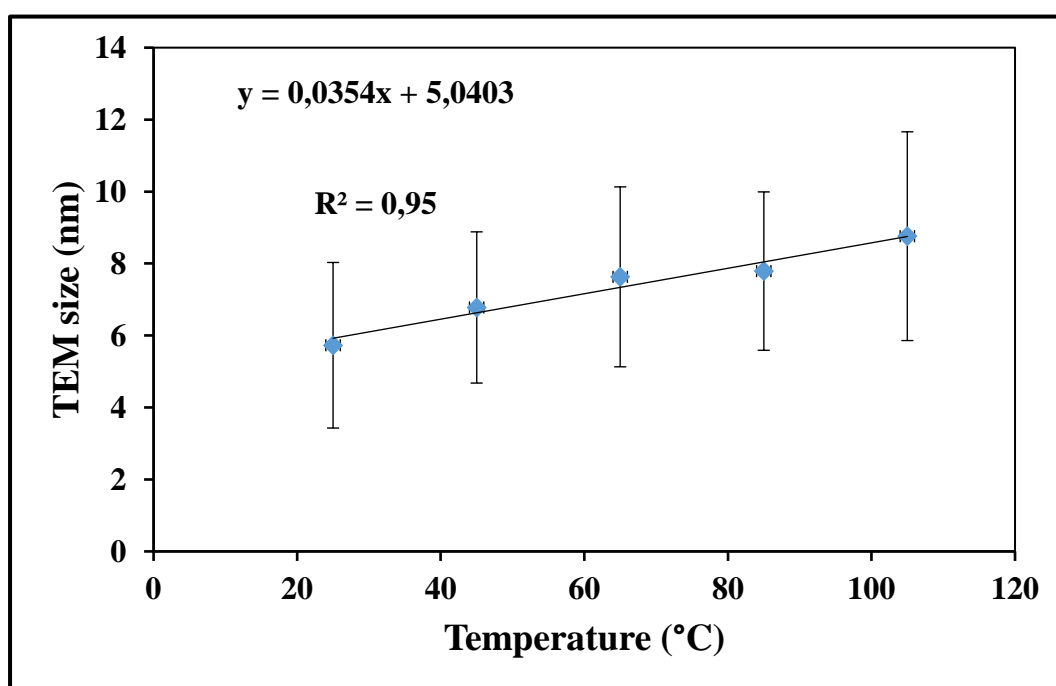


Figure 4.19: The effect of temperature on the TEM size

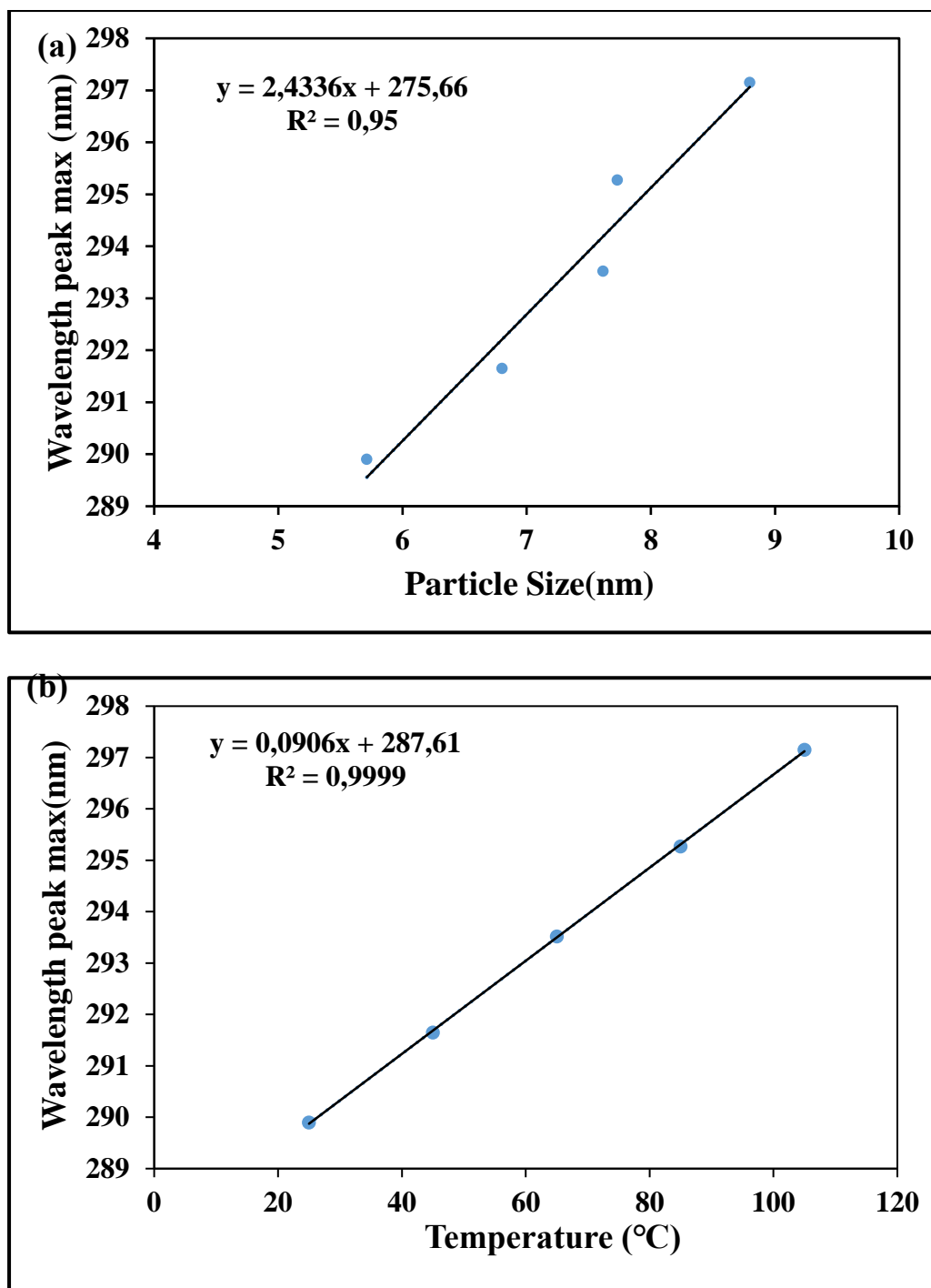


Figure 4.24: (a, b): The effect of temperature on the wavelength peak maximum of iron oxide nanoparticles

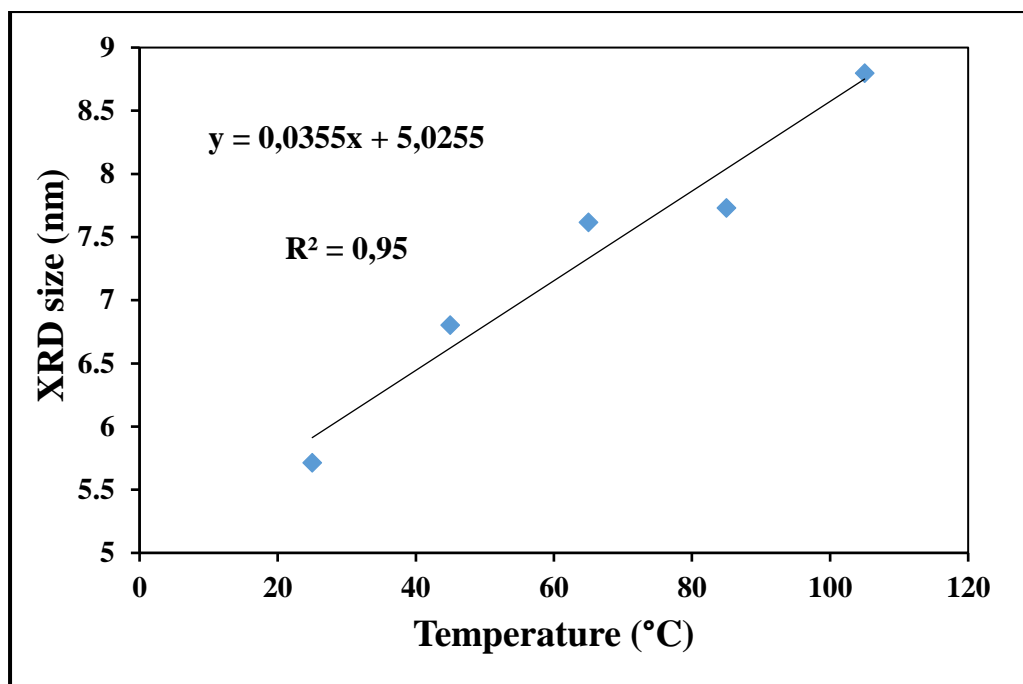


Figure 4.25 The effect of temperature on the XRD size